THE UNIVERSITY OF CHICAGO

ACOUSTICALLY LEVITATED GRANULAR MATTER

A DISSERTATION SUBMITTED TO
THE FACULTY OF THE DIVISION OF THE PHYSICAL SCIENCES
IN CANDIDACY FOR THE DEGREE OF
DOCTOR OF PHILOSOPHY

DEPARTMENT OF PHYSICS

BY
MELODY XUAN LIM

CHICAGO, ILLINOIS
MARCH 2022

To the one in whom all things hold together

TABLE OF CONTENTS

LIST OF FIGURES

LIST OF TABLES

ACKNOWLEDGMENTS

None of the work in this thesis would have been possible without the constant support, optimism, and encouragement provided by my advisor, Heinrich Jaeger. Thank you for teaching me to see beyond the data, and to piece together coherency from the disordered fragments of the day-to-day.

The work in this thesis is the fruit of many discussions with an incredible team of people. Vincenzo Vitelli has the incredible gift of finding each hidden assumption, asked incredibly helpful questions, and led me to think more deeply about my experimental results. Anton Souslov showed me not only how to develop theoretical models and apply them to experimental data, but also how to be a considerate and helpful collaborator. Bryan VanSaders is an excellent sounding-board for ideas (even beyond his great expertise with simulations of all types), and always seeks ways to contribute to and advance the boundaries of what we know. It has been a pleasure to work with and learn from Isaac Harris, Adam Kline, Annie Xia, Tchakamau Ra, Tali Khain, Brady Wu, Tanvi Gandhi, and Nina Brown. Thank you for allowing me to do science with you. I would also like to thank my thesis committee members, Sidney Nagel and Daniel Fabrycky. Thanks for your support, inspiring discussions, and great ideas.

I am greatly thankful for my labmates. Victor Lee helped me get started on acoustic levitation. I am incredibly grateful for his patient support and mentorship. Kieran Murphy and Leah Roth were amazing office-mates – I am indebted to them for all the conversations we shared, across all the different shades of graduate school life. I would also like to thank Endao Han, Nicole James, Jelani Hannah, Michael van der Naald, Ted Esposito, Grayson Jackson, Hojin Kim, Abhi Singh, Baudouin Saintyves, Yifan Wang, Tom Videbaek, Nidhi Pashine, and everyone else in the soft matter labs at Chicago. Thank you for filling my graduate school days with the light of your camaraderie.

I thank Jason Kim for his constant friendship, support, and love.

I am eternally grateful to Bob Behringer, who introduced me to the magic of granular materials. I will forever remember Bob as an example of a great scientist, and an amazing human, mentor, and friend.

This research was supported by the National Science Foundation through Grants No. DMR-1309611, DMR-1810390 and DMR-2104733. This work utilized the shared experimental facilities at the University of Chicago MRSEC, which is funded by the National Science Foundation under award number DMR-2011854. This research utilized computational resources and services supported by the Research Computing Center at the University of Chicago.

ABSTRACT

The properties of small particle clusters can differ dramatically from the bulk phases of the same constituents. For conditions out of equilibrium, new pathways and physical principles for cluster formation and reconfiguration emerge. These principles underlie phenomena from molecular assembly to the formation of planets from granular matter. In this thesis, we introduce acoustic levitation as a platform to experimentally probe the formation of small structures in a controlled environment far from equilibrium. Scattered sound establishes short-range, shape-dependent attractions between millimeter-scale particles. In this substrate-free, underdamped environment, six or seven particles cluster into shapes that resemble flowers and turtles, while hundreds of particles self-assemble into granular droplets with strikingly fluid-like behavior. Particle shape directly controls acoustic forces, with particles preferring to make contact along sharp edges. Detuning the acoustic trap generates active fluctuations that drive cluster rearrangements, droplet spinning and splitting, and soft hinge-like motions, creating a tunable active granular material. Our results open up new possibilities for non-invasively manipulating macroscopic particles, tuning their interactions and directing their assembly.

CHAPTER 1

INTRODUCTION

1.1 Granular matter as a testbed for out-of-equilibrium physics

Many natural systems, from the motion of atoms in a crystal to the dust in a protoplanetary disk, can be modelled as hard spheres with attractive forces. For particles in thermal equilibrium, colloid-polymer mixtures have been successfully used as experimental models of problems in condensed matter physics, where the polymers induce attractions between colloidal hard spheres [1, 2, 3, 4, 5, 6]. In these colloidal systems, key advances have been made by taking advantage of the fact that colloids are large enough to be easily visualised, measured, and tracked, and also small enough to be driven by equilibrium thermal fluctuations.

Naturally, this begs the question of what happens far-from-equilibrium, where thermal flutuations no longer dominate, and where the usual foundations of statistical mechanics can no longer be brought to bear on a system of particles. Furthermore, while colloidal systems have had great success at modelling the physics of overdamped collections of particles, where inertia plays a negligible role in the system dynamics. In particular, adding inertia offers the chance to explore the effects of extreme mechanical driving. Can we extend the success of colloidal matter to far-from-equilibrium, underdamped systems?

Granular materials offer an attractive possibility. These particles (usually hundreds of microns to millimetre sized) can easily be imaged on a single-particle level with precision, permitting detailed explorations of the effect of internal structure, and investigating emergent properties as a function of the number of particles. Mechanically agitated granular matter often serves as a prototype for exploring the rich physics associated with hard sphere systems, with an effective temperature introduced by vibrating or shaking [7, 8, 9, 10, 11, 12].

In these systems, shape additionally provides an important means by which to tune key

properties of dense aggregates, whether their packing fraction [13, 14, 15], contact configuration [16, 17, 18, 19, 20], or mechanical properties [21, 22, 23, 24, 25, 26, 27]. In each of these cases, the shape of a particle determines the global properties of an aggregate by modifying both the geometry of the packing and local inter-particle contacts. These local contacts play a particularly important role in jamming, where the precise type of contact between faceted shapes may dramatically change the mechanical stability of a given packing. In addition, breaking spherical symmetry in a dense granular packing produces a coupling between normal forces and torques on the single-grain level.

In addition to local contact forces and geometry, which produce effects at the level of a single contact on a grain, longer-range particle interactions also play an important role in the properties of a granular material. Previous work has shown that adding weakly attractive dipole-dipole interactions to a granular material provides a means of self-organisation for the force chains that form under compression, thus strengthening the force network that forms as a result [28]. When vibrated, these dipolar interactions drive the formation of chain-like open structures [29]. Alternatively, longer range forces can drive clustering [30, 31] and particle motion [32, 33].

However, while tunable depletion interactions drive clustering and assembly in colloids, no equivalent tunable attractions exist between macroscopic grains (magnetized grains produce dipolar interactions, while electrostatic forces are difficult to tune). Additionally, traditional vibrated granular beds lose much of their inertia to frictional interactions with container walls. These considerations raise the possibility of acoustic levitation, as a means to induce forces between levitated particles and impose external driving in an underdamped environment, all while producing freely-floating structures in midair.

1.2 Acoustic forces on solid particles

The first indication that sound could impart forces on matter was discovered in 1866, reported in English in [34]. Kundt observed that when a horizontal glass tube, closed at both ends, was set into resonance with an external sound wave, powder that was initially scattered at random inside the tube was collected into small piles, whose spacing was determined by the wavelength of sound. This observation set off a flurry of theoretical activity in search of the mechanism – how do sound waves produce forces on objects?

At the same time, the concept of electromagnetic radiation pressure was just entering the scientific consciousness. Lord Rayleigh pointed out in a 1902 paper [35] that "it seemed to me that it would be of interest to inquire whether other kinds of vibration exercise a pressure, and if possible to frame a general theory of the action", and proceeded to calculate the momentum carried by a vibrating gas [36]. This work laid the foundation for the first calculations of what is now referred to as the "acoustic radiation force" [37]: the momentum transferred from an acoustic wave to a particle in that acoustic wave.

We consider a sound wave with frequency ω_0 (and corresponding wavelength λ_0). Such a wave is a resonant mode of the underlying fluid field, and as such consists of the pressure p, velocity $\mathbf{v}$, and density ρ fields. These fields have a spatial part (denoted here as a dependence on vector $\mathbf{x}$), as well as a dependence on time t. Assuming that the sound waves are harmonic in time, we have

$$p(\mathbf{x}, t) = p(\mathbf{x})e^{-i\omega_0 t} \tag{1.1}$$

$$\mathbf{v}(\mathbf{x}, t) = \mathbf{v}(\mathbf{x})e^{-i\omega_0 t} \tag{1.2}$$

$$\rho(\mathbf{x}, t) = \rho(\mathbf{x})e^{-i\omega_0 t}\,. \tag{1.3}$$

Considering these expressions, which are purely harmonic (and thus oscillate about zero), we

arrive at the first difficulty: the time-average of a purely harmonic expression is identically zero, and so to lowest order there is no net momentum transferred to a particle. Thus the acoustic radiation forces must arise from additional nonlinear scattered fields due to the presence of the particles in the acoustic wave.

For convenience, these acoustic radiation forces are divided into primary radiation forces and secondary radiation forces. The primary acoustic force is due to the scattered sound field of a single particle in the acoustic field, and it drives rigid particles to migrate to the pressure nodes of standing acoustic waves. Secondary acoustic forces, on the other hand, are due to secondary scattering between levitated particles, and they drive inter-particle forces.

In general, the computation of the form of either the primary or secondary acoustic force due to particle scattering (let alone the form of these scattered fields) is not straightforward. Such an acoustic force depends, for instance, on the details of the particle geometry, whether or not the particles are compressible, and the arrangement of particles in the acoustic field. However, some progress can be made in certain limits. The most common approximation is that particles are perfectly rigid and have a radius a much smaller than the wavelength of sound, which propagates in an inviscid fluid, a regime referred to as the Rayleigh limit. In this limit (where particles can be accurately treated as spheres), the acoustic radiation force on a point scatterer is conservative [38, 39, 40, 41, 42], and can be expressed as the gradient of the acoustic potential U_{rad}:

$$F_{\text{rad}} = -\nabla U_{\text{rad}} \tag{1.4}$$

$$U_{\text{rad}} = \frac{4\pi}{3} a^3 \rho_0 \left[f_1 \frac{1}{2} c_0^2 \langle p^2 \rangle - f_2 \frac{3}{4} \langle v^2 \rangle \right], \tag{1.5}$$

where sound propagates in the particle with speed c_p, the particle material density is ρ_p, and the fluid has speed of sound c_0 and density ρ_0. Angled brackets denote time averages

of the pressure p and velocity v. The scattering coefficients f_1 and f_2 are given by

$$f_1 = 1 - \frac{c_p^2 \rho_p}{c_0^2 \rho_0}$$
$$f_2 = \frac{2(\rho_p/\rho_0 - 1)}{2\rho_p/\rho_0 + 1}.$$

We emphasize that Eq. 1.5 is quantitatively accurate only for spherical (point-like) scatterers, in the Rayleigh limit ($a \ll \lambda_0$).

Other regimes, however, are highly relevant and in need of exploration. In particular, there is the question of what happens when a particle can no longer be treated as a point particle. This can happen in two senses. First, a particle or cluster of particles may no longer be small compared to λ_0. The many-particle case in particular has so far only been treated in the limit of dilute particle suspensions, where the inter-particle separation is large compared to a. In this case, the total secondary acoustic force can be calculated by a mean-field approach [42], namely by summing individual contributions to Eq. 1.5. When particles are instead closely packed into a cluster, how does Eq. 1.5 need to be modified?

Alternatively, a particle may have a shape that is significantly different from the smooth, symmetric shape of a sphere. Calculations and simulations have so far focused on the force between other types of levitated particles with a high degree of symmetry, such as cylinders [43, 44, 45], or between smooth deformable objects such as liquid drops [46] and bubbles [47] (the acoustic radiation forces on gas bubbles are usually referred to as Bjerknes forces). What about shapes without a high degree of symmetry, such as cubes and flat discs? How are their secondary acoustic fields different to the point scatterer case? These issues point to the need for a systematic experimental and numerical effort to understand the secondary acoustic forces in new size and shape regimes, which is one major focus of this work.

1.3 The scope of this thesis

This thesis takes the first steps into the intersection of two fields, acoustic levitation and granular materials, with the aim of showing not only that each can be used to shed light on the other, but also that their union produces surprising new physics. As such, this thesis has two main goals: first, to use acoustic levitation to probe the out-of-equilibrium clustering of granular materials, and second, to use granular materials to deepen our understanding of secondary acoustic forces. The main body of this thesis is composed of six parts. In Chapter 2, we introduce some experimental methods that are useful for acoustically levitating granular materials. Chapter 3 introduces numerical methods for the calculation of acoustic forces. Chapter 4 shows how we used these methods to probe the assembly statistics and pathways of six- and seven-particle clusters. Chapter 5 extends this study of clustering to clusters consisting of twenty to two-hundred particles, which we find assemble into rafts with strikingly liquid-like behaviour. These rafts also display an anomalous dependence of their surface tension and bulk modulus on their size, pointing to a gap in our understanding in secondary acoustic forces. Chapter 6 further demonstrates that levitated grains cluster by joining sharp corners, establishing the connection between shape and secondary acoustic forces. Chapter 7 combines these ideas by showing that shape (via the secondary acoustic force) can be used to direct the out-of-equilibrium self-assembly of lock-and-key structures. Chapter 8 contains conclusions, and an outlook for avenues of further research.

CHAPTER 2

EXPERIMENTAL METHODS FOR ACOUSTIC LEVITATION

2.1 Introduction

Acoustically levitated granular matter in principle requires only two components: an acoustic standing wave, and granular material. In practice, care must be taken with the methods used to generate the standing wave.

Here, we describe the setup used in Chapters 4-7, as illustrated in Fig. 2.1 We generate a standing wave of the acoustic pressure field between an ultrasound transducer and a transparent reflector. The reflector height and tilt are controlled by a pair of translation stages, while the transducer is attached to a second translation stage, with micrometer attached, controlling the precise distance between reflector and transducer. The setup (including transducer) is enclosed in an acrylic box ($l \times w \times h = 0.6 \times 0.3 \times 0.6\text{m}^3$) to mitigate the effect of external air currents. The walls of the box are far from the levitation area, such that the acoustic trap has open boundary conditions. In addition, all experiments were performed in a humidity- and temperature-controlled environment (40-50% relative humidity, 22-24° C).

2.2 Transducer design

We used a commercial transducer (Hesentec HS-4AH-3540, base diameter 55mm, frequency 40±1 kHz) to generate ultrasound. An aluminium horn was bolted onto the transducer to maximise the strength of the nodes in the pressure field, using the finite-element optimization reported in Ref. [48] as a basis. The reported design was then scaled down to increase the resonant frequency closer to that of the commercial transducer, and modified to flare out with a wider base. The resulting design is shown in schematic form in Fig. 6.1(b). The base of the horn (diameter 38.1mm) was painted black to better image the particles from below.

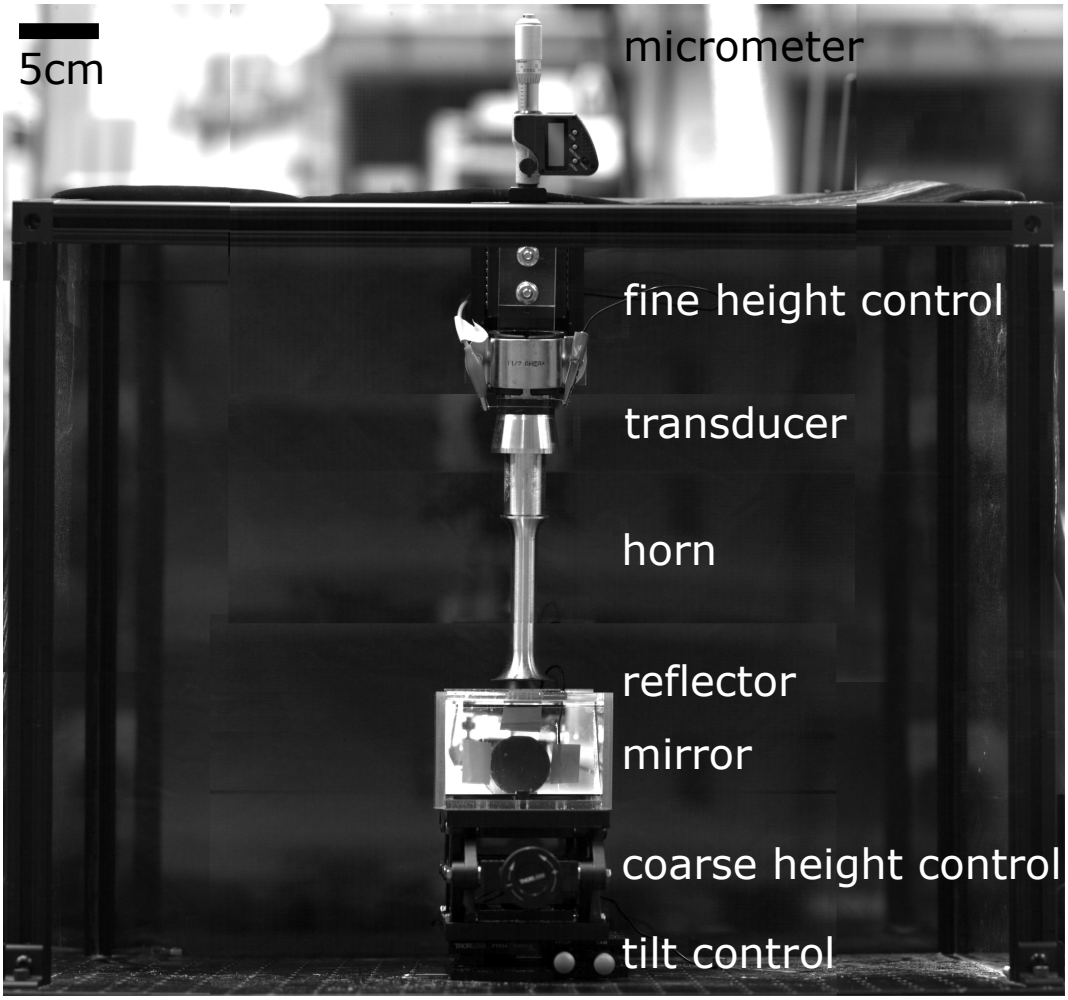

Figure 2.1: Composite photograph of the experimental setup, as used in Chapters 4-7. Labels are placed next to the different parts of the setup, which is enclosed in a black metal frame. Side walls are enclosed using acrylic sheets. For visual clarity, the back of the enclosure has been covered with a black background.

The transducer was driven by applying an AC voltage, produced by a function generator (BK Precision 4052) connected to a high-voltage amplifier (A-301 HV amplifier, AA Lab Systems, gain 20), with care to make sure that the aluminium horn is grounded. Particles can generally be levitated for peak-to-peak voltages between 200V and 400V; particles that have a lower mass (either smaller or lower density) can be levitated at lower voltages.

In order to find the resonant frequency of the transducer and horn, we invert the setup (so the bottom surface of the horn is facing upwards) and scatter 100μm polyethylene grains on the surface. We then adjust the driving frequency slowly until we find the peak displacement of the grains on the transducer surface. More refined measurements to find the peak pressure output of the transducer can then be taken with an acoustic sensor sensitive to ultrasonic frequencies (here the Xarion Eta100 Ultra Optical Microphone). Using these methods, the resonant frequency of the transducer (coupled to the horn) was found to be $f_0 = 45.65$kHz. In order to mitigate the self-heating of the transducer, the transducer was turned on at least two hours before an experiment, allowing the transducer time to come to thermal equilibrium with its environment.

2.3 Reflector design

The strongest constraint with respect to the design of the reflector is the requirement to visualize the granular dynamics. Since much of the dynamics takes place in the two-dimensional nodal plane, this necessitates a bottom or top view - i.e. through either the transducer or the reflector. Practically speaking, it is easiest to create a transparent reflector. Any choice of rigid transparent material can usually be used - in this thesis, acrylic was most frequently used as the reflector base due to the ease of constructing parts out of laser-cut acrylic. Acrylic can also be purchased with anti-static coatings (AC-300), reducing some of the issues related to static charge buildup on grains in the acoustic trap. In order to further reduce issues with static charge buildup, a grounded indium tin oxide (ITO)

coated glass slide (thickness 1.1mm) was additionally secured to the top of an acrylic sheet ($(l \times w \times h = 152 \times 152 \times 6\text{mm}^3)$). Before each experiment, the acrylic/glass reflector was cleaned with compressed air, ethanol, and de-ionised water. We neutralised any charges that remained on the reflector with an anti-static device (Zerostat 3, Milty).

This transparent reflector is glued to a box, which is mounted to a lab jack and adjusted so that the distance between transducer and reflector is $\lambda_0/2$, corresponding to the transducer resonant frequency f_0, or wavelength $\lambda_0 \approx 7.2$mm in air.

The acrylic reflector was glued to a box mounted on a lab jack and adjusted to a transducer-reflector distance $n\lambda_0/2$, corresponding to $f_0 = 45.65$kHz, with n either 1 or 2 depending on the experiments performed. We confirmed that this transducer-reflector distance corresponded to the stable resonant frequency of the cavity by adding a large particle (Cospheric, material density $\rho = 1,000\,\text{kg}\,\text{m}^{-3}$, diameter $d = 710 - 850\,\mu$m) to the acoustic trap and observing its lack of translational and rotational motion. The acoustic trap was then detuned by adjusting the frequency f of the function generator. Polyethylene particles (diameter 710-850μm) levitate within a horizontal plane one-quarter of the gap height from the reflector.

2.4 Visualizing particle dynamics

Video was recorded using a high speed camera (Phantom v12 or Phantom v2515) at 1,000-3,000 frames per second. We image these acoustically trapped particles from the side (Fig. 6.1c), or from below (Fig. 6.1d), through a mirror oriented at 45° to the levitation plane. Since the reflector and transducer are both flat, the levitated granular material can explore an area with characteristic length up to ten times the diameter of the cluster. At the same time, tracking microstructural changes in the interior of the cluster requires a large number of pixels per particle in any given image. In addition, the experiment necessitates that the particles be some distance from the camera. Combined, these factors necessitate

the use of a macro lens with a large focal distance (here, either a Nikon 200mm f/4 AF-D Macro or IRIX 150mm f/2.8 Macro 1:1 lens). In order to maximise the image depth of field, images were taken at the largest practical f-stop (32). Particles were illuminated using a focused LED lighting system (Dedolight).

2.5 Tracking particles and extracting statistics

In this thesis, we focus mostly on statistics and the general shape of clusters. Such statistics can be extracted without tracking the detailed position of particles in a cluster. The first step for particle tracking is to isolate the cluster from its background, which is easily achieved by thresholding the image to produce a black-and-white binary image. The largest connected cluster of pixels in such a black and white image can then be identified, and all other clusters removed. Functions such as `regionprops` in Matlab can then be used to extract key properties of the identified particles, and distinguish types of particle shape.

CHAPTER 3

NUMERICAL METHODS TO COMPUTE ACOUSTIC FORCES

3.1 Introduction

It is frequently useful to compute the acoustic forces on an object in an acoustic trap. In this section, we describe two strategies for computing the acoustic forces on an object, both based on finite-element simulations. Such simulations have been recently shown to be an accurate, general tool for the calculation of acoustic radiation forces for particles of arbitrary shape [49, 50], and a variety of boundary conditions [51].

In the acoustic limit (where the effects of viscosity are negligible), the forces on a particle can be considered as a result of only radiative momentum transfer, as outlined in Sec. 1.2. As such, the first step towards computing acoustic forces is to accurately compute the acoustic fields $p(\mathbf{x}, t), \mathbf{v}(\mathbf{x}, t)$, and $\rho(\mathbf{x}, t)$. Here, we used the acoustics module of Comsol Multiphysics to compute the acoustic fields in the frequency domain, at the driving frequency of the transducer f_0, such that the result is the spatial part of the acoustic fields.

Accurately computing the spatial part of the acoustic fields thus reduces to the problem of accurate modelling of the experimental boundary conditions. For fully three-dimensional models (Fig. 3.1(a)), we use a cylindrical volume with diameter $38.1mm$ (corresponding to the width of the base of the horn in the experiment) and height $n\lambda_0/2$, where n is an integer (usually 1). The top and bottom of the cylinder are set to be perfectly reflecting boundaries. Such a cavity can form a resonator when driven at the transducer frequency f_0.

In some cases, the full three-dimensional nature of the acoustic field is not as important, and it is sufficient to compute the acoustic fields within a two-dimensional axisymmetric model (Fig. 3.1(b)). All other model parameters remain the same.

The next step is to establish a standing wave in the acoustic cavity. Here, we used one of two methods, depending on what physics the simulation was intended to highlight.

If a simulation was intended to closely reproduce the experimental conditions, a standing wave was established by applying a normal acceleration to the top of the cylindrical cavity (transducer side). In the frequency domain, this normal acceleration corresponds to a harmonic acceleration of the transducer surface. Since there are no corresponding experimental measurements of the transducer acceleration, all simulation results are accurate only up to an overall scaling factor, which we usually normalize with a suitable choice of energy scale. Acoustic energy was dissipated by plane-wave radiation conditions on the cavity sides. The plane-wave radiation conditions ensure a gradient of acoustic energy from the cavity center to the exterior, providing a weak restoring force that confines particles to the cavity center.

The simulation scheme as outlined above closely mimics the experimental boundary conditions. When comparing the numerical solution to theoretical calculations (usually done assuming a plane standing wave [42]), or when finding the secondary acoustic force far from the center of the trap, the plane wave radiation conditions can obscure some of the underlying physics. In this case, the standing wave was established simply by enforcing a background pressure condition with given amplitude P_0, such that the initial background pressure is $P(z) = P_0 \sin(2\pi z/\lambda)$.

3.2 Rayleigh limit: computing the Gor'kov acoustic potential

In order to compute the Gor'kov acoustic potential (Eq. 1.5) on a particle, the pressure and velocity fields resulting from the boundary conditions above can be straightforwardly substituted into Eq. 1.5.

Since the Gor'kov acoustic potential U_{rad} is valid in the point scatterer limit ($a \ll \lambda_0$), the particle on which U_{rad} acts (the probe particle) does not need to be modelled in the finite element model. This means that a model of the empty acoustic cavity is used to compute the primary acoustic force in the Gor'kov approximation. In order to compute the secondary acoustic force, a perfectly scattering particle can be fixed in the center of the acoustic cavity,

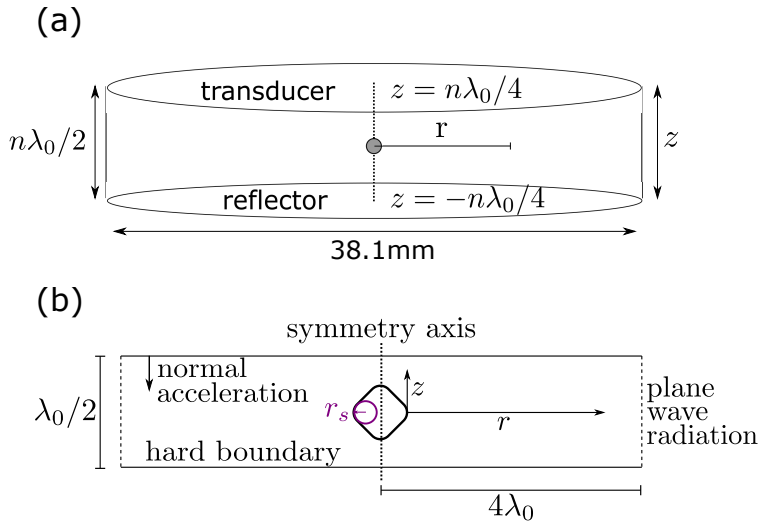

Figure 3.1: (a) A general schematic of the cavity geometry in three dimensions, introducing the parameters used in modelling the sound field. The cavity has n nodes, and is constructed to resonate with the acoustic driving, which has wavelength λ_0. (b) A specific example of a 2D axisymmetric setup for calculating the acoustic potential, where $n = 1$, and boundary conditions are schematically indicated.

such that the resulting U_{rad} corresponds to the potential on a point particle in response to the fixed scattering particle.

The flexibility of the finite-element method means that a particle of any shape and size can be fixed in the trap center, and U_{rad} calculated. We use this approach to find the force on a point scatterer due to the presence of a faceted particle in Chapter 6, and a planar crescent-shaped particle in Chapter 7.

3.3 Beyond the Rayleigh limit: fluid structure interactions

When a particle becomes larger than the Rayleigh limit (practically, when $a/\lambda_0 > 0.1$), the Gork'kov acoustic potential becomes less and less valid as an approximation. In this case, it becomes necessary to model higher order effects of the probe particle on the acoustic field, instead of simply treating the probe as a point scatterer. We follow the approach of Ref. [49] in calculating the fluid-structure interaction between a pair of particles. An example model

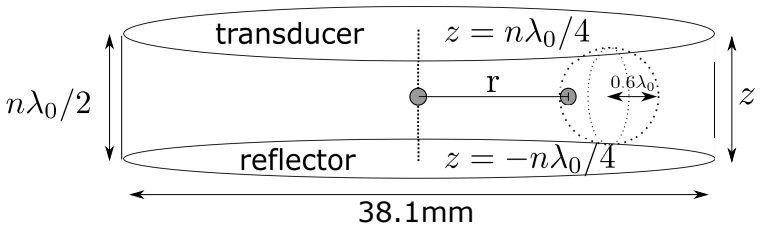

Figure 3.2: A general finite element model for computing the acoustic force between a pair of particles due to the fluid-structure interaction. The source particle is placed at the trap center, while the probe particle is placed at some distance r away. In order to calculate the acoustic force, the probe particle is surrounded by an integration surface (sphere, marked by dotted lines).

geometry is shown in Fig. 3.2 (with all other boundary conditions as above). A perfectly scattering source particle is fixed in the center of the acoustic trap. The probe particle, which is allowed to deform elastically, is placed some distance away. The force on this probe particle is them computed by integrating the momentum flux over an integration surface S, with surface normal $\hat{\mathbf{n}}$. Quantitatively, the vector acoustic force $\mathbf{F}$ (which in general is no longer conservative) is given by [49]

$$\mathbf{F} = \int_S \left[-\frac{1}{2\rho c^2}\langle p^2 \rangle + \frac{1}{2}\rho \langle v^2 \rangle \right] \hat{\mathbf{n}} d\mathbf{A} - \int_S d\mathbf{A} \rho \langle (\mathbf{v} \odot \hat{\mathbf{n}}) \cdot \hat{\mathbf{n}} \rangle, \tag{3.1}$$

where ρ is the levitation medium density, in which sound propagates with speed c. Angled brackets denote a time average, and $\mathbf{v} \odot \hat{\mathbf{n}}$ is the element-wise product of $\mathbf{v}$ and $\hat{\mathbf{n}}$ (i.e. $v_i n_i$).

Any integration surface that completely encloses the particle, and does not intersect any of the domain boundaries, can be used. In general, a large integration surface gives more accurate results, since the number of mesh points on which to evaluate the integral is larger. In Chapter 4, we work with a spherical integration surface whose diameter is six times the probe particle diameter (shown in Fig. 3.2 as a dotted line).

CHAPTER 4

ASSEMBLY STATISTICS AND PATHWAYS OF SMALL ACOUSTIC CLUSTERS

4.1 Introduction

In this Chapter, we focus on understanding the effect of out-of-equilibrium fluctuations on the statistics of cluster formation.[1] In the acoustic trap, scattered sound establishes short-range attractions between small particles [41, 38, 52, 53], while detuning the acoustic trap generates active fluctuations [54]. To illuminate the interplay between attractions and fluctuations, we investigate transitions among ground states of two-dimensional clusters composed of a few particles. Experiments and modelling reveal that, in contrast to thermal colloids, in non-equilibrium granular ensembles the magnitude of active fluctuations controls not only the assembly rates but also their assembly pathways and ground-state statistics. These results open up new possibilities for non-invasively manipulating macroscopic particles, tuning their interactions, and directing their assembly.

In two dimensions, particle clusters with five or fewer constituents have only one compact configuration, i.e., one isostatic ground state [55] (Fig. 1a). However, beginning with six particles, there are an increasing number of energetically degenerate, but geometrically distinct, ground-state configurations. This complex energy landscape has been studied with colloids in thermal equilibrium [4, 55]. Here, we explore the ground-state statistics in ensembles of macroscopic particles driven by active fluctuations that emerge from the dynamics of a driven system rather than from coupling to a heat bath. Furthermore, we demonstrate how energetic degeneracies, assembly rates, and pathways are altered during out-of-equilibrium assembly.

1. This Chapter is based on Lim, Melody X., Anton Souslov, Vincenzo Vitelli, and Heinrich M. Jaeger, "Cluster formation by acoustic forces and active fluctuations in levitated granular matter." Nature Physics 15, no. 5 (2019): 460-464.

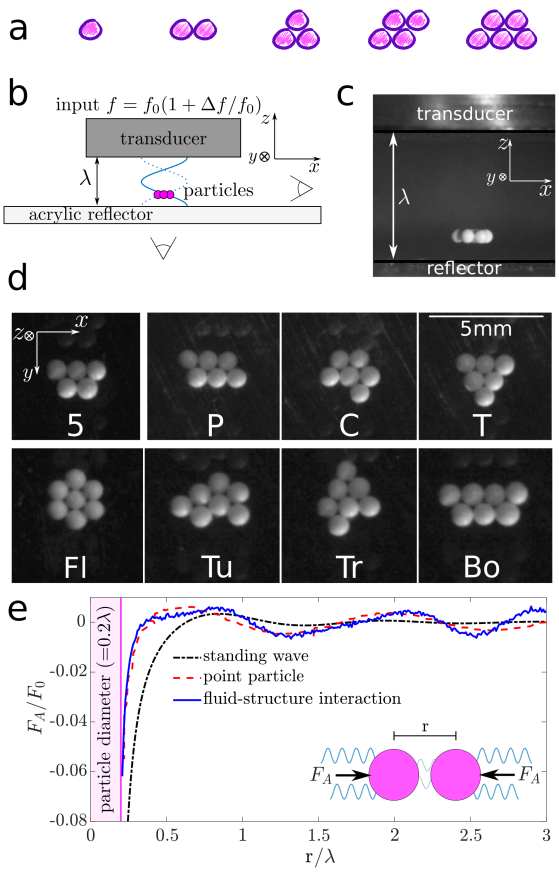

Figure 4.1: **Acoustic levitation as a platform to assemble and manipulate clusters composed of macroscopic particles.** (a) Sketches of compact cluster configurations (isostatic ground states) for one to five particles. (b) Schematic of experimental setup. An ultrasound transducer generates sound waves in air, with speed of sound $c_s = 343\text{m/s}$. The distance between transducer and transparent acrylic reflector is chosen to create a pressure standing wave (blue line) with two nodes, at frequency $f_0 = 45.651\text{kHz}$ and wavelength c_s/f_0. Polyethylene particles are acoustically levitated in the lower of the two nodes. Clusters are imaged from the side (b), as well as from below via a mirror (c). (c) Different cluster configurations, imaged from below. (Top) In two dimensions, there is only one 5-particle cluster configuration, but six particles can form one of three distinct ground states: parallelogram P, chevron C, and triangle T. (Bottom) Seven-particle clusters have four compact configurations: flower Fl, turtle Tu, tree Tr, and boat Bo. (d) The acoustic field generates short-range attractions within the levitation plane, which stabilises particle clusters. Force between two particles as a function of distance r between their centres, normalised by the particle weight $F_0 \equiv m_0 g$. Finite-element simulations (red dashed, blue solid lines) are compared to an analytical solution for particles in a standing wave [42] (black dashed-dotted line). (Inset) Schematic illustrating the sonic depletion force between two particles in an acoustic field.

To eliminate frictional interactions with container walls we levitate particles in a sound pressure field. The same field also induces short-range, tunable attractions that we here call sonic depletion forces. Much like depletion forces in colloids [56] or other Casimir-like forces, these acoustically-mediated attractions can generate robust particle clusters. This differs from the formation of clusters in granular media due to external confinement [57, 7] or, transiently, due to inelastic collisions [58, 57, 7, 59]. Furthermore, the sonic depletion forces scale with the sound pressure amplitude, which enables precise control over cluster energetics. Such control provides advantages over cohesive forces due to capillary bridges, van der Waals interactions, or charging [30, 31]. Finally, in contrast to induced electric or magnetic dipole forces [32], the acoustic interactions are not aligned with an applied vector field.

4.2 Experimental Setup and Methods

Our setup is illustrated in Fig. 6.1b, with details as given in Chapter 2. Polyethylene particles (diameter 710–850 μm) levitate within a horizontal plane one-quarter of the gap height from the reflector. We image these acoustically trapped particles from the side (Fig. 6.1c) or from below (Fig. 6.1d) using a high-speed camera

When multiple particles are placed in the trap, they form compact clusters. Images of the resulting configurations for six- and seven-particle clusters are shown in Fig. 6.1d. In order to extract cluster shape information from the raw videos, we thresholded the images, then computed properties of the largest connected region in the resulting image using black-and-white image operations (`regionprops`). These functions are available in Matlab. Since each cluster is associated with a specific set of shape parameters, we computed the number of times a cluster shape was formed, divided by the total number of times that any cluster shape was formed, to obtain cluster statistics. Six-particle systems have three distinct ground-state configurations: parallelogram (P), chevron (C), and triangle (T). For 7-particle clusters,

there are four distinct topologies: Flower (Fl), Tree (Tr), Turtle (Tu), and Boat (Bo) [60].

Whereas colloidal clusters can be stabilised by depletion forces, acoustically levitated clusters are stabilised by sonic depletion forces, which are short-range attractions generated by acoustic scattering. At close approach, these Casimir-like forces F between spherical particles scale as

$$F \sim \frac{E_0 a^6 \lambda^{-3}}{r^4} \tag{4.1}$$

where $E_0 \equiv \rho_0 v_0^2/2$ is the energy density of the sound field having amplitude v_0 and wavelength λ in air (density ρ_0) [42]. The particles have radius a and are distance r ($\ll \lambda$) apart.

For arbitrary separation, these forces can be computed analytically in the absence of trap geometry [42]. Alternatively, we used finite element modeling software (COMSOL) to model the force between a pair of particles levitated in the acoustic field, using two different methods. In both cases, we established a background standing pressure wave with given amplitude, with a particle with radius $r = 0.1\lambda$ fixed in the center of the trap. The levitation chamber was constructed to have height $3\lambda_0/2$ and width $4\lambda_0$, with materials parameters chosen to match the experiment. In one case, labelled "point particle", we computed the force on a point particle in the resulting pressure field by solving the equations for the acoustic field by using the expression derived in Ref. [38]. In the second case, labelled "fluid-structure interaction", we computed the force on a second particle of radius $r = 0.1\lambda$ by computing the full fluid-structure interaction, following the method of [49].

These calculations, shown in Fig. 6.1e, indicate that cluster energetics are dominated by the strong short-range attractions between nearest neighbours, as captured in Eq. (4.1).

The acoustic trap can also induce non-conservative forces. Specifically, we use the fact that the particle dynamics in the acoustic field are underdamped (in contrast to colloids in a liquid) to drive instabilities that generate active fluctuations. As Ref. [54] shows, a sound wave with frequency f tuned just slightly larger than the standing wave resonance condition

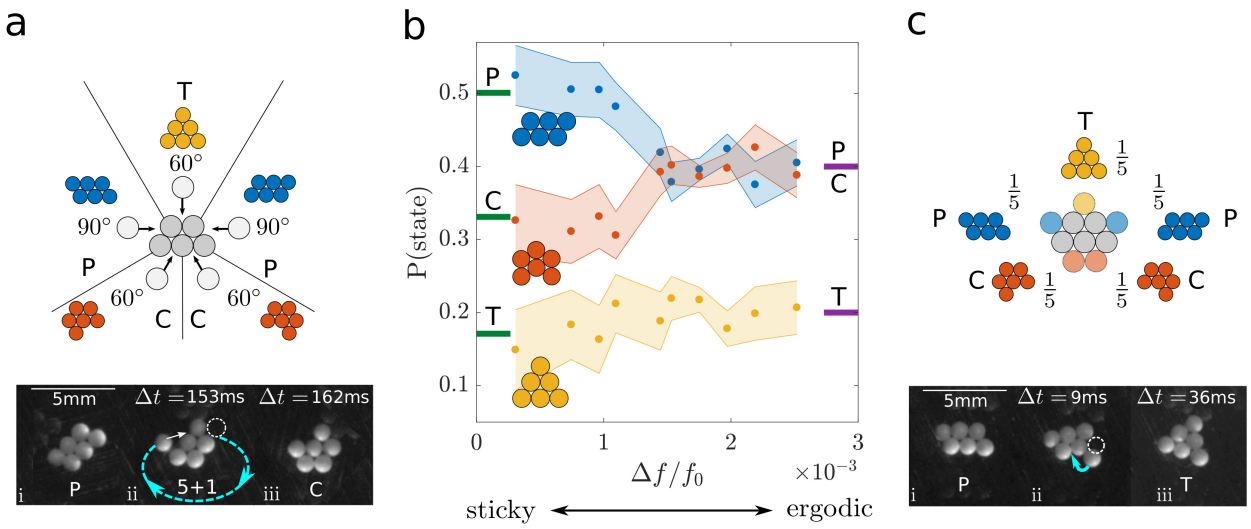

Figure 4.2: **Tuning 6-particle assembly between sticky and ergodic limits.** Near resonance, cluster statistics follow sticky assembly (a). As the acoustic trap is detuned by increasing the sound frequency (b), cluster statistics change to ergodic assembly (c). (a) Sticky assembly: In the regime of small detuning parameter, $\Delta f/f_0 > 0$, the likelihood of a cluster configuration is determined by the geometric angle of approach of a sixth particle to the 5-particle cluster (top). (Bottom) Sequence of images from below showing a sticky rearrangement pathway. (b) Steady-state probabilities for 6-particle-cluster ground-state configurations as a function of detuning parameter. Standard error is indicated by shaded region. Horizontal bars indicate model predictions for the sticky and ergodic limits (see text). (c) Ergodic assembly: For larger detuning, the sixth particle has equal probability of occupying each of the five binding sites on the five-particle cluster (top). (Bottom) Sequence of images from below showing a transition between ground states in the ergodic regime through a hinge motion.

acts on a levitated object with a destabilising force proportional to the object's speed. As a result, the clusters fluctuate up and down in the trap, occasionally hitting the reflector. This impact transfers kinetic energy from center-of-mass motion to modes that bend the cluster out of its planar, two-dimensional configuration. For sufficiently high amplitudes, these active fluctuations can lead to rearrangements between the different ground states.

4.3 Assembly of six-particle clusters

For these 6-particle clusters, the different possible ground states are each associated with a unique eccentricity. A time series can thus be first divided into the segments where there are six (or seven) connected particles by thresholding for a minumum area of connected pixels, and then isolating the parts of the time series into cluster shapes by the eccentricity of the cluster. We thus define the probability of forming a given state by the time spent in a given ground state divided by the total amount of time the cluster spends in a stable 6-particle ground state (P, C, or T),

Close to resonance, 6-particle clusters rearrange by ejecting a single particle, which then travels many particle diameters in a curved trajectory before it re-joins the 5-particle cluster from a random angle of approach. Once the particle re-joins, it becomes stuck due to the short-range attraction. This sticky, far-from-equilibrium assembly pathway is shown in Fig. 4.2a. The corresponding cluster statistics retain memory of the formation process [52]: the ground-state configuration is determined by the spatial angle of approach that the sixth particle takes towards the 5-particle cluster. Assuming that docking onto the 5-cluster is equally likely for any angle of approach (see Fig. 4.2a), the probabilities of forming P, C, or T 6-clusters are 1/2, 1/3, and 1/6, respectively, in close agreement with the data for the sticky limit (Fig. 4.2b).

By contrast, deep into the off-resonant regime, clusters rearrange by moving particles randomly along their periphery (Fig. 4.2c). This occurs either by single particle ejection with much shorter trajectories (i.e., no more than one particle diameter) or by 'floppy' hinge motions: When all but one of the bonds to nearest neighbours is broken by active cluster fluctuations, the remaining bond acts as a flexible hinge. This enables the particle to swing around to a new position without leaving the cluster. In this off-resonant regime, we find that P and C clusters occur with equal probability and twice as often as T clusters (Fig. 4.2b). Such cluster statistics correspond to an unbiased sampling of configuration space, where we

simply count the number of ways a 6-cluster can be formed by adding one more particle to a 5-cluster. This ergodic limit is indistinguishable from the thermal case, which [55] observed using 6-particle clusters composed of micrometre-sized Brownian colloids.

By changing the ultrasound frequency, we can control the amplitude of active fluctuations and thus control the cluster rearrangement processes. Figure 4.2b shows statistics for relative ground-state probabilities as a function of detuning parameter $\Delta f/f_0$, where f_0 (= 45.651kHz) is the trap resonant frequency, f is the driving frequency, and $\Delta f \equiv f - f_0 > 0$. As the trap is detuned, cluster statistics transition smoothly from sticky to ergodic. At the same time, clusters increasingly rearrange via hinge motions.

4.4 Out-of-plane fluctuations as an effective temperature

The emergence of hinge motions is closely linked to out-of-plane bending, which like particle ejection is triggered by impacts against the reflector, as shown in Fig. 4.3a. As a measure of out-of-plane bending, we calculated the second moment J of the vertical coordinate z by integrating the distance to the z geometric center of the cluster over the area of the cluster. That is,

$$J = \iint_A (z - z_0)^2 \, dA \,,$$

where z_0 is the z geometric center of the cluster. Note that we define J for the specific 2D projection of the cluster sideview. For a fully planar configuration, J is at a minimum; if the cluster is bent out of plane, J increases. Representative time series of J for small and large detuning parameters are shown in Fig. 4.3a. From longer versions of such time series, the probability distributions $P(J)$ for finding a particular magnitude J can be extracted. As Fig. 4.3b shows, clusters remain effectively rigid and planar for small $\Delta f/f_0$, while further

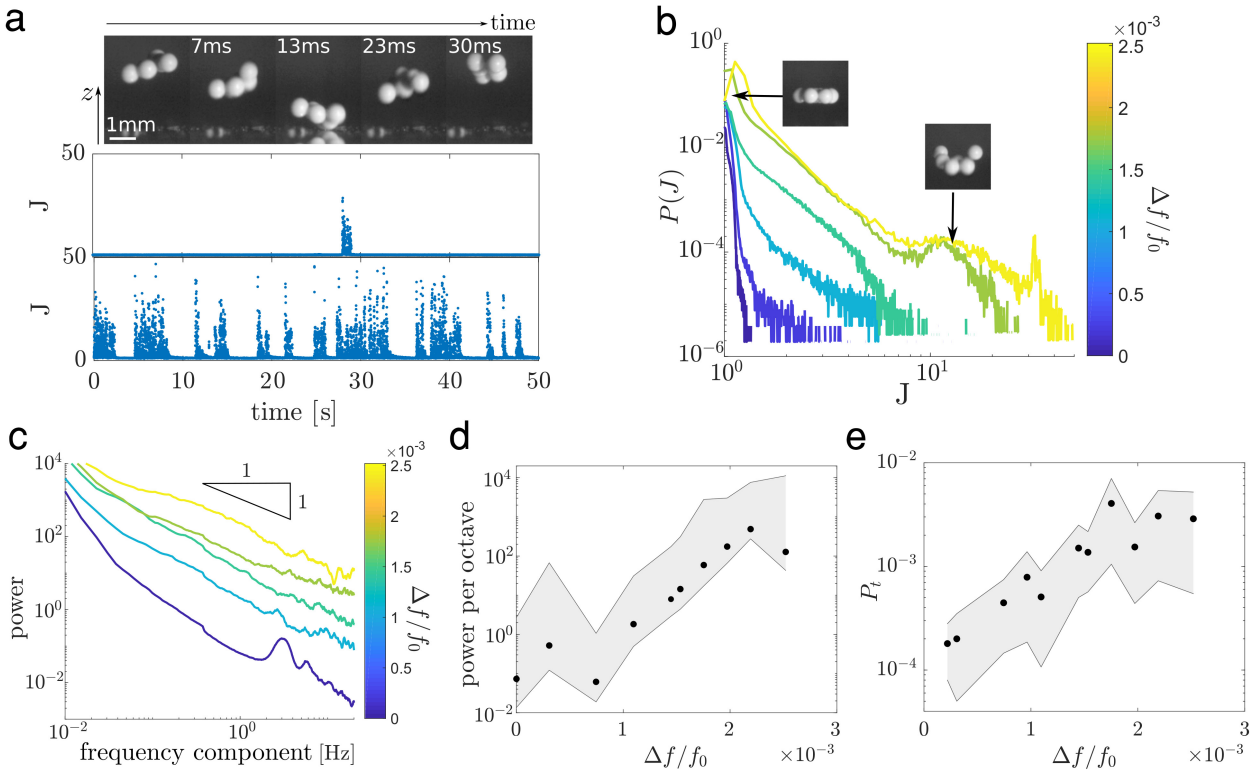

Figure 4.3: **Out-of-plane fluctuations as a measure of effective temperature.** (a) (Top) Sequence of side images showing a cluster colliding with the reflector. Time series for second moment J of vertical coordinate z (see Methods), for small detuning (middle) and large detuning (bottom). (b) Probability distribution of J as function of detuning parameter, obtained from time series as in part (a). Illustrative side images of clusters are shown at their value of J. (c) Power spectrum of the J time series. (d) Average power per octave as function of detuning parameter. (e) P_t, the probability of transition between any cluster ground state, as a function of detuning parameter. Shaded areas in (d) and (e) indicate the standard error. Note the similar trends in (d) and (e): the fluctuations increase exponentially as a result of the effective temperature induced by detuning away from resonance.

detuning generates a rapidly increasing probability of exciting large-J values associated with shape-changing, out-of-plane bending fluctuations. These fluctuations also become more frequent (Fig. 4.3a, bottom), resulting in broad power spectra whose magnitude quickly rises with $\Delta f/f_0$, while their overall character changes little (Fig. 4.3c).

When we plot the average power per octave associated with shape-changing fluctuations we find it to increase exponentially with detuning parameter $\Delta f/f_0$ (Fig. 4.3d). At the same time, we find that also the probability P_t of observing a transition between any two 6-particle ground states increases exponentially (Fig. 4.3e). Together, this shows that $\Delta f/f_0$ plays the role of an effective temperature in an activated process: detuning the trap generates instabilities that temporarily break particle-particle bonds and allow for cluster rearrangement.

Here, a surprising aspect is that detuning not only controls the rate, but also the type of rearrangement process. From Fig. 4.2b, we see that these processes have important consequences for the likelihood of observing specific ground state configurations. In particular, the degeneracy between parallelogram (P) and chevron (C) in the ergodic limit can be broken by moving to the regime dominated by sticky assembly.

4.5 A general model for athermal cluster reconfigurations

Driven by active fluctuations, these clusters explore an athermal ensemble. The cluster reconfigurations are instances of a general transition process through intermediate states. We model this process with a discrete-time Markov chain, in which state transition matrices represent the creation of specific ground state configurations through adding or removing one particle. To represent the various ground-state probabilities P_i for a general N-particle cluster, we list them as i components of a vector $\mathbf{P}_N$. Specifically for $N = 6$, $\mathbf{P}_6 = (P_P, P_C, P_T)$, where the subscripts refer to the three possible configurations. The (i, j)-th element of the transition matrix T_N represents the probability of creating the i-th N-particle ground state by adding a single particle to the j-th $(N-1)$-particle ground state. Similarly, the (i, j)-th

element of the matrix Q_N captures how the i-th N-particle state is obtained by destroying the j-th ground state of the $(N+1)$-particle cluster. Under steady-state conditions, $\mathbf{P}_N$ is related to the probabilities $\mathbf{P}_{N-1}$ and $\mathbf{P}_{N+1}$ through

$$\mathbf{P}_N = \mathrm{T}_N \mathbf{P}_{N-1} + \mathrm{Q}_N \mathbf{P}_{N+1} \,. \tag{4.2}$$

Once T_N and Q_N are known, Eq. (4.2) can be solved recursively for $\mathbf{P}_N$ (see Methods). For the case discussed so far, with six particles in the trap, Eq. (4.2) leads to $\mathbf{P}_6 = \mathrm{T}_6 \mathbf{P}_5$ and $\mathbf{P}_5 = \mathrm{Q}_5 \mathbf{P}_6$, which gives $\mathbf{P}_6 = \mathrm{T}_6 \mathrm{Q}_5 \mathbf{P}_6$. Since removing any particle from a 6-cluster results in the same 5-cluster (so that $\mathbf{P}_5 = 1$), we have $\mathrm{Q}_5 = \begin{pmatrix} 1 & 1 & 1 \end{pmatrix}$. However, the 3×1 matrix T_6 depends on whether the creation process is sticky or ergodic, i.e., its components are the docking probabilities indicated in the top panels of Fig. 4.2a, c. Solving for $\mathbf{P}_6$ then gives the values indicated by the horizontal bars along either side of Fig. 4.2b, in close agreement with the data.

4.6 Assembly of seven-particle clusters

Having obtained T_6 and Q_5, we can now make predictions for the case that there are seven particles in the trap and $\mathbf{P}_7$ represents the four ground states shown in Fig. 6.1d. Figure 4.4a shows the reconfiguration pathways for 7-particle clusters and, as examples, transitions from boat to tree via hinge-motion and from flower to turtle via particle ejection and recapture. In the model, we assume that T_7 contains only processes that generate 7- from 6-particle states in an ergodic fashion. As a result, T_7 is a 4×3 matrix with elements corresponding to docking one particle at any available 6-cluster site with equal probability (Fig. 4.4a).

Recursively solving Eq. (4.2) for $\mathbf{P}_7$, we find steady-state probabilities near 0.075, 0.47, 0.30 and 0.15 for the flower (Fl), tree (Tr), turtle (Tu) and boat (Bo) configurations (see Methods for details). Importantly, the model indicates that all four 7-particle ground states

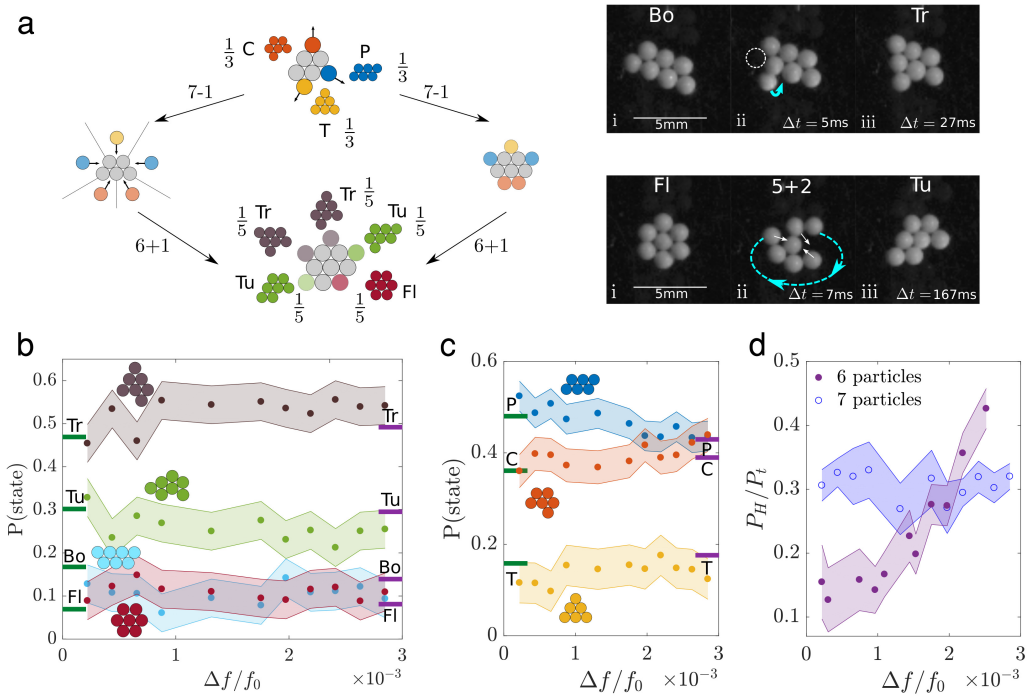

Figure 4.4: **Seven-particle cluster assembly, ground-state statistics, and transition states.** (a) Left: Schematic of model for statistics of six- and seven-particle clusters in the acoustic trap. Acoustic frequency tunes the formation of six-particle clusters from sticky (centre left) to ergodic (centre right) regimes. Six-particle clusters can be formed when a particle is removed from the edge of a seven-particle cluster (top). In the reverse process, seven-particle clusters are formed ergodically from six-particle clusters (bottom). Right: Sequence of images from below showing a transition between seven-particle states via a hinge motion (top) or a particle ejection (bottom). (b) Distribution of seven-particle cluster configurations as a function of detuning parameter, with standard error indicated by shaded area. The green (purple) bars indicate statistics derived from taking into account the sticky (ergodic) six-particle clusters. (c) Statistics of intermediate six-particle clusters within a seven-particle system, plotted as a function of detuning parameter (standard error indicated by shaded area). The green (purple) bars indicate statistics derived from considering sticky (ergodic) cluster assembly. (d) Probability of observing a hinge motion P_H as a fraction of the total number of transitions P_t for different values of the detuning parameter. Filled, purple (hollow, blue) disks correspond to clusters of 6 (7) particles.

should be largely insensitive to whether the 6-particle intermediate states are formed from 5-particle precursors via a sticky or ergodic process. These numerical values are in excellent agreement with the data (Fig. 4.4b).

A further model prediction concerns the probabilities for the intermediate 6-particle states in the 7-particle system, shown in Fig. 4.4c. As before, these states are strongly affected by whether the sticky or ergodic assembly process is followed. However, the probabilities differ from those for the ground states in the 6-particle system (Fig. 4.2b), since now T_7 and Q_6 enter the Markov-chain model. Again we find that these probabilities are consistent with the data.

This match between model and experiments justifies, *a posteriori*, the above assumption about the applicability of the ergodic form of T_7 across the whole range of $\Delta f/f_0$. However, we can also check this assumption directly. This is done in Fig. 4.4d, where we plot the experimentally observed probability of reconfiguration via hinge motion P_H relative to P_T as a function of the detuning parameter $\Delta f/f_0$. While for 6-clusters this fraction increases steadily with detuning, for 7-clusters it is effectively independent of $\Delta f/f_0$, just as the 7-cluster statistics. This difference in hinge-mode proliferation reflects that larger clusters support more bending modes and generate larger out-of-plane bending amplitudes along their periphery. We conclude that hinge motions serve as a key indicator for processes that generate ergodic reconfigurations among the ground states.

4.7 Conclusions

In this paper we introduced acoustic levitation as a tool to assemble small clusters of particles and investigate their dynamic reconfigurations. While thermal fluctuations set the magnitude of depletion forces in more microscopic particle systems such as colloids, the sonic depletion forces discussed here depend on the sound pressure amplitude and thus can be controlled independently from the effective temperature of the system. The effective temperature, in

turn, was shown to be an emergent quantity that arises from the dynamic response of the levitated objects in the off-resonant regime $\Delta f/f_0 > 0$.

We can envision acoustic levitation as a more general platform for non-invasive manipulation of granular matter with tunable attractive interactions. Our results open up new opportunities for investigating in the underdamped regime the dynamics of extended, 2D rafts of close-packed particles [61]. Since the levitated particles are macroscopic, anisotropy in sonic depletion forces could be achieved via particle shape and/or by combining materials with different sound scattering properties. This may provide a means to assemble complex structures similar to what has been done with patchy colloids [62, 5] or shape-dependent entropic forces [63]. Longer-range interactions analogous to those between particles at curved fluid interfaces [33] could be implemented using the back-action of levitated grains on the sound field itself.

4.8 Additional information

In this section, we provide additional relevant details for the results presented in Chapter 4 (originally published as Supplementary Information to Lim, Melody X., Anton Souslov, Vincenzo Vitelli, and Heinrich M. Jaeger, "Cluster formation by acoustic forces and active fluctuations in levitated granular matter." Nature Physics 15, no. 5 (2019): 460-464.). Contents include a full derivation of the Markov-chain model results of Chapter 4.5 and 4.6, a comparison to thermal seven-particle cluster statistics, and the number of observations for the cluster statistics. In addition there are three additional figures, which show the acoustic force as a function of detuning parameter, the thermal seven particle statistics, and a comparison between the primary and secondary forces in the levitation plane.

4.8.1 Details of the Markov-Chain Model

We consider a discrete-time Markov chain that relates the cluster statistics for five-, six-, and seven-particle clusters by examining the physical processes that produce different clusters. We consider the following mechanisms: (1) Seven particle clusters are formed by ergodically adding a particle to a six-particle cluster (meaning that the particle occupies any binding site with equal probability). (2) Six-particle clusters are formed from five-particle clusters, in a way that depends on the detuning parameter. (3) Six-particle clusters are also formed from the removal of a particle from the edge of a seven-particle cluster. (4) Five-particle clusters are formed from the removal of a particle from the edge of a six-particle cluster. Denoting the probability of state S as $P(S)$, we write

$$\mathbf{P_7} = \begin{pmatrix} P(Fl) \\ P(Tu) \\ P(Tr) \\ P(Bo) \end{pmatrix}, \mathbf{P_6} = \begin{pmatrix} P(P) \\ P(C) \\ P(T) \end{pmatrix}, \mathbf{P_5} = \begin{pmatrix} P(5) \end{pmatrix} .$$

We recall that there are four possible states for seven-particle clusters, three for six-particle clusters, and one for five-particle clusters. Let $\mathrm{T}_N^{e,s}$ denote the creation matrix that describes building a N-cluster from an $(N-1)$-cluster for either ergodic or sticky processes, and Q_N the destruction matrix for breaking an $N+1$-cluster to make a N-cluster. Then

$$\mathbf{P_7} = \mathrm{T}_7^e \mathbf{P_6}, \tag{4.3}$$

$$\mathbf{P_6} = \frac{1}{2}\mathrm{Q}_6 \mathbf{P_7} + \frac{1}{2}\mathrm{T}_6^{e,s} \mathbf{P_5}, \tag{4.4}$$

$$\mathbf{P_5} = \mathrm{Q}_5 \mathbf{P_6}. \tag{4.5}$$

Note that we assign equal weight to the processes which form a six-particle cluster from a five-cluster, and those which form a six- cluster from a seven-cluster. In addition, T_6 describes either ergodic or sticky six-particle formation processes depending on the detuning parameter.

Six particle statistics

If we exclude the seven-particle processes from the model, we are left with

$$\mathbf{P_6} = \mathrm{T}_6^{e,s}\mathbf{P_5}, \tag{4.6}$$

$$\mathbf{P_5} = \mathrm{Q}_5\mathbf{P_6}. \tag{4.7}$$

We construct an effective transition matrix R_{66}, describing the six- to six-cluster transitions through intermediate five-cluster states. Substituting Eq. (4.7) into Eq. (4.6),

$$\mathrm{R}_{66} = \mathrm{T}_6^{e,s}\mathrm{Q}_5. \tag{4.8}$$

To find Q_5, we consider the possible clusters that result from removing a particle from the edge of a cluster. Trivially, removing any particle from a six-cluster results in the unique five-cluster:

$$\mathrm{Q}_5 = \begin{pmatrix} 1 & 1 & 1 \end{pmatrix}. \tag{4.9}$$

In addition, $\mathrm{T}_6^{e,s}$ are constructed from the ergodic and sticky models:

$$\mathrm{T}_6^e = \begin{pmatrix} 2/5 \\ 2/5 \\ 1/5 \end{pmatrix}, \mathrm{T}_6^s = \begin{pmatrix} 1/2 \\ 1/3 \\ 1/6 \end{pmatrix}. \tag{4.10}$$

Since the steady state probability vector $\mathbf{P_6}$ satisfies $\mathbf{P_6} = R_{66}\mathbf{P_6}$, we find $\mathbf{P_6}$ by finding the eigenvector of R_{66} with unit eigenvalue. Substituting

$$\mathbf{P_6^e} = \begin{pmatrix} 2/5 \\ 2/5 \\ 1/5 \end{pmatrix}, \mathbf{P_6^s} = \begin{pmatrix} 1/2 \\ 1/3 \\ 1/6 \end{pmatrix}.$$

These probabilities are shown in Fig. 2b of the main text.

Seven particle statistics

Similarly to the six-cluster derivation, we derive expressions for the effective transition matrices M_{77} and M_{66} from Eqs. (4.3)-(4.5), such that $\mathbf{P_7} = \mathrm{M}_{77}\mathbf{P_7}$ and $\mathbf{P_6} = \mathrm{M}_{66}\mathbf{P_6}$. The steady-state probabilities are then the eigenvectors of M_{66} and M_{77} with unit eigenvalue. Note that M_{77} and M_{66} include transitions through five- and six-cluster intermediates. Substituting Eqs. (4.3) and (4.5) into (4.4), we obtain

$$M_{66} = \frac{1}{2}\mathrm{Q}_6\mathrm{T}_7^e + \frac{1}{2}\mathrm{T}_6^{e,s}\mathrm{Q}_5\,. \tag{4.11}$$

We derive M_{77} by substituting Eq. (4.5) into (4.4), which is then substituted for $\mathbf{P_6}$ in Eq. (4.3):

$$\begin{aligned}\mathbf{P_7} &= \mathrm{T}_7^e \left(\frac{1}{2} \mathrm{Q}_6 \mathbf{P_7} + \frac{1}{2} \mathrm{T}_6^{e,s} \mathrm{Q}_5 \mathbf{P_6} \right) \\ &= \frac{1}{2} \mathrm{T}_7^e \mathrm{Q}_6 \mathbf{P_7} + \frac{1}{2} \mathrm{T}_7^e \mathrm{T}_6^{e,s} \mathrm{Q}_5 \mathbf{P_6}\end{aligned}$$

In order to get a closed-form expression for $\mathbf{P_7}$, we continue substituting for P_6:

$$\begin{aligned}\mathbf{P_7} &= \frac{1}{2} \mathrm{T}_7^e \mathrm{Q}_6 \mathbf{P_7} + \frac{1}{2} \mathrm{T}_7^e \mathrm{T}_6^{e,s} \mathrm{Q}_5 \left(\frac{1}{2} \mathrm{Q}_6 \mathbf{P_7} + \frac{1}{2} \mathrm{T}_6^{e,s} \mathrm{Q}_5 \mathbf{P_6} \right) \\ &= \frac{1}{2} \mathrm{T}_7^e \mathrm{Q}_6 \mathbf{P_7} + \frac{1}{4} \mathrm{T}_7^e \mathrm{T}_6^{e,s} \mathrm{Q}_5 \mathrm{Q}_6 \mathbf{P_7} \\ &+ \frac{1}{4} \mathrm{T}_7^e \mathrm{T}_6^{e,s} \mathrm{Q}_5 \mathrm{T}_6^{e,s} \mathrm{Q}_5 \mathbf{P_6}\end{aligned}$$

This leads to a geometric series in increasing numbers of transitions between five- and six-cluster states:

$$\mathbf{P_7} = \frac{1}{2} \mathrm{T}_7^e \mathrm{Q}_6 \mathbf{P_7} + \left(\sum_{n=1}^{\infty} \frac{1}{2^{n+1}} \mathrm{T}_7^e (\mathrm{T}_6^{e,s} \mathrm{Q}_5)^n \mathrm{Q}_6 \right) \mathbf{P_7}$$

We note that $\mathrm{T}_6^{e,s}\mathrm{Q}_5$ is idempotent, so that $(\mathrm{T}_6^{e,s}\mathrm{Q}_5)^n = \mathrm{T}_6^{e,s}\mathrm{Q}_5$ for any n. Then we complete the geometric series and write

$$M_{77} = \frac{1}{2} \mathrm{T}_7^e \mathrm{Q}_6 + \frac{1}{2} \mathrm{T}_7^e \mathrm{T}_6^{e,s} \mathrm{Q}_5 \mathrm{Q}_6 \tag{4.12}$$

To find the destruction matrix Q_6, we assume that any particle on the edge of a cluster has equal probability to be removed. Then Fl can only make C, Tu makes P and C with equal probability, Tr makes P, C, and T equally, and Bo makes only P:

$$Q_6 = \begin{pmatrix} 0 & 1/3 & 1/2 & 1 \\ 1 & 1/3 & 1/2 & 0 \\ 0 & 1/3 & 0 & 0 \end{pmatrix}$$

Similarly, we construct T_7^e assuming that a seventh particle has equal probability to attach to any binding site on a six-particle cluster:

$$T_7^e = \begin{pmatrix} 0 & 1/5 & 0 \\ 1/3 & 2/5 & 1 \\ 1/3 & 2/5 & 0 \\ 1/3 & 0 & 0 \end{pmatrix}$$

Substituting into Eqs. 4.11 and 4.12 and solving the eigenvalue problem, as for the six-particle clusters, gives

$$\mathbf{P_7^s} = \begin{pmatrix} 0.071 \\ 0.464 \\ 0.303 \\ 0.161 \end{pmatrix}, \mathbf{P_7^e} = \begin{pmatrix} 0.079 \\ 0.480 \\ 0.299 \\ 0.141 \end{pmatrix}$$

and

$$\mathbf{P_6^s} = \begin{pmatrix} 0.484 \\ 0.355 \\ 0.161 \end{pmatrix}, \mathbf{P_6^e} = \begin{pmatrix} 0.426 \\ 0.349 \\ 0.180 \end{pmatrix}$$

4.8.2 Thermal seven-particle clusters

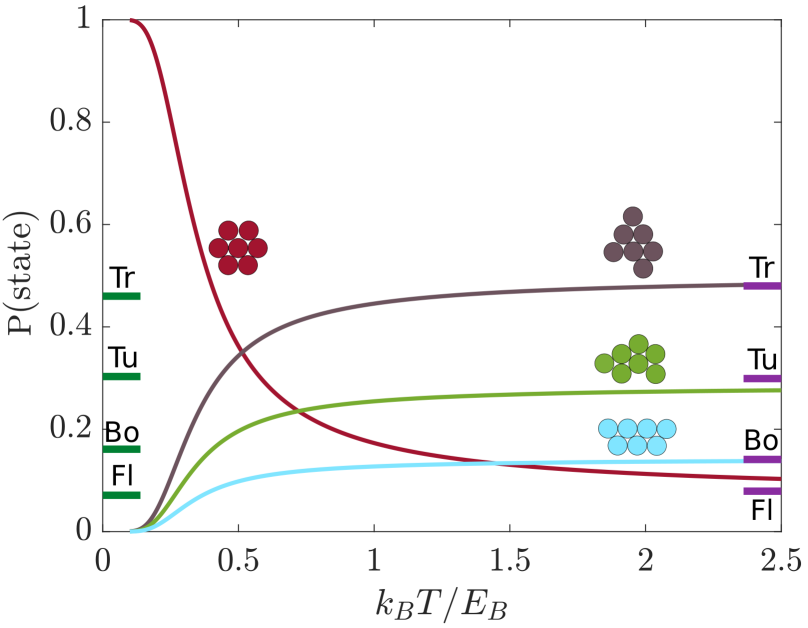

Figure 4.5: **Predicted statistics for thermal seven-particle clusters.** Cluster statistics for thermal seven-particle clusters as a function of k_BT/E_B (solid curves). See section S1 for derivation. The probabilities from the Markov-chain model in the ergodic (sticky) used in the main text are also shown as purple (green) bars. Within error of our experiment, the Markov-chain predictions in the ergodic regime are indistinguishable from the high-temperature limit of the thermal seven-particle clusters ($k_BT > 2E_B$).

For thermal clusters, the flower is the only ground state of the seven-particle system, since it has one more bond than the tree, turtle, or boat. For this reason, in a thermal system, the relative occupation probabilities of the four possible configurations are a function of the temperature. These statistics can be calculated as follows.

Let the energy of each bond be E_B. Then we define the flower as having zero energy (the only ground state), and the tree, turtle, and boat as being at energy E_B each. Then the partition function of the system is

$$\begin{aligned} Z &= \sum_i \mathrm{e}^{-E_i/k_BT} \\ &= n_{Fl} + (n_{Tr} + n_{Tu} + n_{Bo})\mathrm{e}^{-E_B/k_BT} \end{aligned}$$

where n_i is the degeneracy of each possible cluster configuration, T is the temperature, and k_B is the Boltzmann factor. To determine the degeneracy of each cluster configuration, we count the number of ways to make a given configuration from a six-particle cluster, multiplied by the degeneracy of that six-particle cluster. The flower can be made only one way (add a particle to the chevron), but the chevron can be made two ways from the five-particle cluster, so $n_{Fl} = 2$. Similarly, the boat can be made two ways from the parallelogram, and the parallelogram two ways from the five-particle cluster, so $n_{Bo} = 4$. The turtle can be made two ways from the parallelogram, and two from the chevron, so $n_{Tu} = 8$. Finally, the tree can be made in two ways from the parallelogram, two ways from the chevron, and six from the triangle (which can only be made one way from the five-particle cluster), so that $n_{Tr} = 14$. The probability of each state as a function of temperature is thus:

$$\begin{aligned} \mathrm{P(Fl)} &= \frac{2}{2 + 14\mathrm{e}^{-E_B/k_BT}} \\ \mathrm{P(Bo)} &= \frac{4}{2\mathrm{e}^{E_B/k_BT} + 14} \\ \mathrm{P(Tu)} &= \frac{8}{2\mathrm{e}^{E_B/k_BT} + 14} \\ \mathrm{P(Tr)} &= \frac{14}{2\mathrm{e}^{E_B/k_BT} + 14} \end{aligned}$$

These probabilities are plotted as a function of k_BT/E_B in Fig. 4.5. For reference, the probabilities from the Markov-chain model used in the main text are also shown. Within error of our experiment, the Markov-chain predictions in the ergodic regime are indistinguishable from the high-temperature limit of the thermal seven-particle clusters ($k_BT > 2E_B$). Thus the failure of the system to find the global ground state even in the ergodic limit suggests that our large detuning limit is most analogous to a high temperature thermal system.

4.8.3 Supplementary Figures

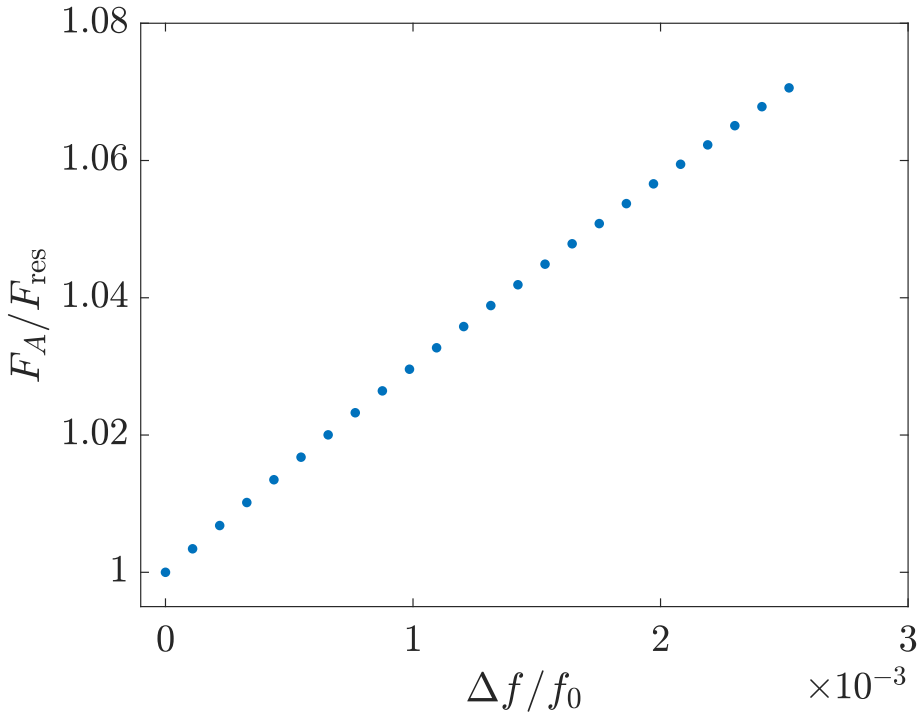

Figure 4.6: **Acoustic force as a function of detuning parameter.** We used finite element modeling software, as in Fig. 3.1 and Fig. 3.2, to determine the variation of acoustic force F_A between a pair of particles as a function of detuning parameter $\Delta f/f_0$. For this calculation, $r = 0.25\lambda$, and all geometrical parameters are fixed in terms of λ_0 while the wavelength of the standing wave is detuned. We plot F_A normalised by the force at resonance, F_{res}. The magnitude of acoustic force increases less than 10% for the experimental range of detuning.

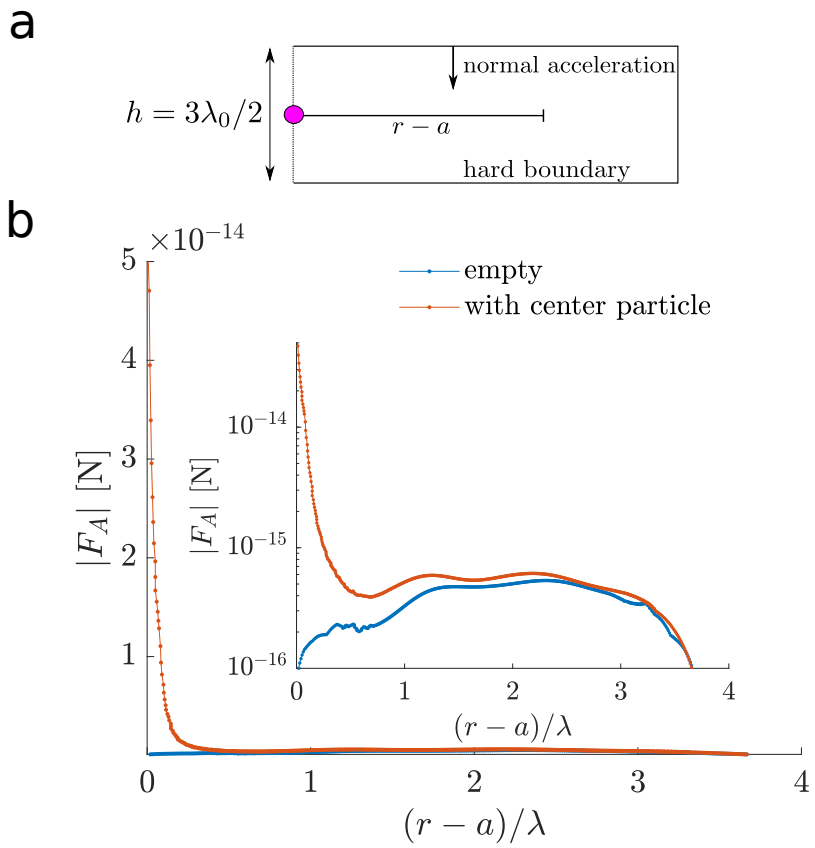

Figure 4.7: **Acoustic forces dominate dynamics in the levitation plane.** (a) Simulation geometry. The axisymmetric acoustic cavity is modeled using a finite-element simulation. The top of the cavity is driven at a fixed normal acceleration (0.1m/s^2 for the results shown here), while the bottom enforces a sound hard boundary (perfectly reflecting) condition. We apply a plane-wave radiation condition to the left boundary to mimic the experimental conditions. The acoustic force F_A as a function of r, distance from the center, on a point scatterer in the levitation node is calculated from the resulting pressure and velocity field according to the expression derived in Ref. [38]. F_A is calculated for two different configurations: (1) the point scatterer subject only to a standing wave ("empty"), or (2) a perfectly scattering particle fixed in the center of the trap ("with center particle", compare to the curve labeled "point particle" in Fig 1e of the main text). (b) Comparison of the force on a point scatterer due purely to the trap (blue, primary radiation force), to the force on a point scatterer due to the presence of another particle (red, secondary radiation force or acoustic force). (Inset) same as main figure, with a log-scale y-axis. When the particles are close, the acoustic force is larger than the confining potential by 2 orders of magnitude.

4.8.4 Supplementary Tables

$\Delta f/f_0 \times 10^{-3}$	number of observations
0.31	347
0.74	360
0.96	639
1.10	665
1.45	472
1.53	1305
1.75	1992
1.97	1393
2.19	2114
2.52	584

Table 4.1: Number of observations for 6-clusters

$\Delta f/f_0 \times 10^{-3}$	number of observations
0.22	843
0.44	1151
0.66	350
0.88	1103
1.32	671
1.75	1136
1.97	1329
2.19	1869
2.41	1454
2.63	1372
2.85	1537

Table 4.2: Number of observations for 7-clusters

CHAPTER 5

MECHANICAL PROPERTIES OF ACOUSTICALLY LEVITATED GRANULAR RAFTS

5.1 Introduction

In this Chapter, we ask what happens when we self-assemble acoustically levitated rafts of twenty to two hundred particles, and use the rotational dynamics of the acoustic trap to probe their mechanical properties[1]. The dynamics of rapid rotation underpin a wide range of physical systems, from rotating black holes [64, 65, 66], to the shapes of spinning self-gravitating asteroids [67, 68, 69], the cooling of optically trapped microparticles [70], and the spin and stability of atomic nuclei [71, 72, 73, 74]. To probe the stability and modes of deformation of such systems, rotating liquid droplets are often used as models, where surface tension mimics attractive forces that bind the material and compete with the outward pressure exerted by the rotation [71, 64, 75, 76, 77, 72, 73]. The small size of molecules implies that liquid droplets can only represent the elastic limit where the number of constituent components is very large, and internal structure is treated as a continuum. Deviations from elastic behavior emerge in the mesoscopic regime as the surface to volume ratio becomes large. For example, measurements of thin films and metallic nanopillars have found elastic moduli [78, 79], dielectric constants [80], and melting temperatures [81] that depend on the system size.

Observing the effects of internal structure and investigating emergent properties as a function of the number of constituent particles in the mesoscopic regime is possible by using colloids [82, 2, 83] or the micron-sized particles in dusty plasmas [84, 85, 86] as 'model atoms', but generating rapid rotations is difficult. For exploring the mesoscale dynamics in

1. This Chapter is adapted from Lim, Melody X., Bryan VanSaders, Anton Souslov, and Heinrich M. Jaeger,"Acoustically levitated granular rafts." arXiv preprint arXiv:2106.09765 (2021).

a rapidly rotating, inertial, many-particle system we here introduce acoustically levitated granular rafts: close-packed monolayers of sub-millimeter particles freely floating in air.

In these rafts, tunable attractive forces generate short-ranged cohesion, providing in-plane elastic properties as well as out-of-plane bending stiffness. As the rotation rate increases beyond the point where inertia outweighs this cohesion, sufficiently large rafts undergo a shape transition strikingly similar to liquid drops. We can image such granular rafts on the particle scale at high temporal resolution, allowing us to measure microstructural properties and dynamics during inertial driving. To explore the emergent physics of this granular system, we here focus on mesoscale rafts comprised of 10 to 200 particles.

Our setup consists of a cylindrical ultrasound transducer (Langevin horn) and a reflector, between which we generate a standing sound wave with a single pressure node along the vertical direction (Fig. 5.1(a)) [87, 88]. While strong sound pressure enables the levitation of solid particles (primary acoustic force), sound scattering between the particles generates attractive interactions among them (secondary acoustic force) [42, 89]. Particles are levitated in air, generating an underdamped environment in which levitated particles collide and self-assemble into a raft, weakly confined to the horizontal plane of the sound pressure node (Fig. 5.1(a), Supplementary Movie 1). Such rafts form roughly circular monolayers comprised of varying numbers of constituent particles (Fig. 5.1(b)).

Driving the cavity slightly above resonance produces stochastic, non-conservative forces, including a torque (along the vertical direction) that imparts angular momentum to the levitated rafts and spins them up. Unlike other strategies for activating underdamped matter [90, 91, 92], the resulting motion of the granular rafts is entirely substrate free. At low angular velocities, the rafts retain their close-packed internal structure (visible in Fig. 5.1(b)). As their rotation speeds up, the rafts undergo deformation via internal rearrangements until they eventually break apart into smaller fragments. Weak radial confinement within the nodal plane brings these pieces back together and they merge by forming a bridge that grows

with time, eventually coalescing back into a single circular raft (Fig. 5.1(c), Supplementary Movie 2). This process is similar to the surface-tension driven coalescence of a pair of liquid drops [93, 94]. Once merged, the (again) circular drop can then be spun up by the acoustic torque, repeating the cycle of spin-up-to-failure.

The spin-up during such cycles provides conditions in which the gyrostatic pressure slowly increases, driving micro-structural changes as well as overall shape deformations. These shape deformations reveal the consequences of the binding potential, here induced by acoustic scattering, on measurable mechanical properties of the granular rafts.

Specifically, we use the rotation-induced shape changes to track how the emergent mechanical properties depend on raft size. We find that the effective surface tension and the effective elastic modulus grow roughly linearly with the number of particles, i.e. both are extensive quantities. We show that this is a direct consequence of acoustically-induced binding energies. This extensivity demonstrates the presence of non-pairwise acoustic forces between particles. We conclude that the properties of levitated granular rafts challenge existing frameworks for the calculation of acoustic forces between multiple particles, which assume superposition of pairwise interactions and, over the same range in raft sizes we explore, would predict saturation at some elastic value. We further show that these rafts also display size-dependent microstructural deformations.

5.2 Experimental Setup and Methods

Experiments

Our acoustic trap consists of an acoustic resonant cavity, driven on one side by a commercial ultrasound transducer (Hesentec HS-4SH-3840). An aluminum horn was bolted onto the transducer to maximize the strength of the pressure field, as detailed in Ref. [87, 88] (Fig. 5.1(a), first panel). The base of the horn (diameter 38.1mm) was painted black to bet-

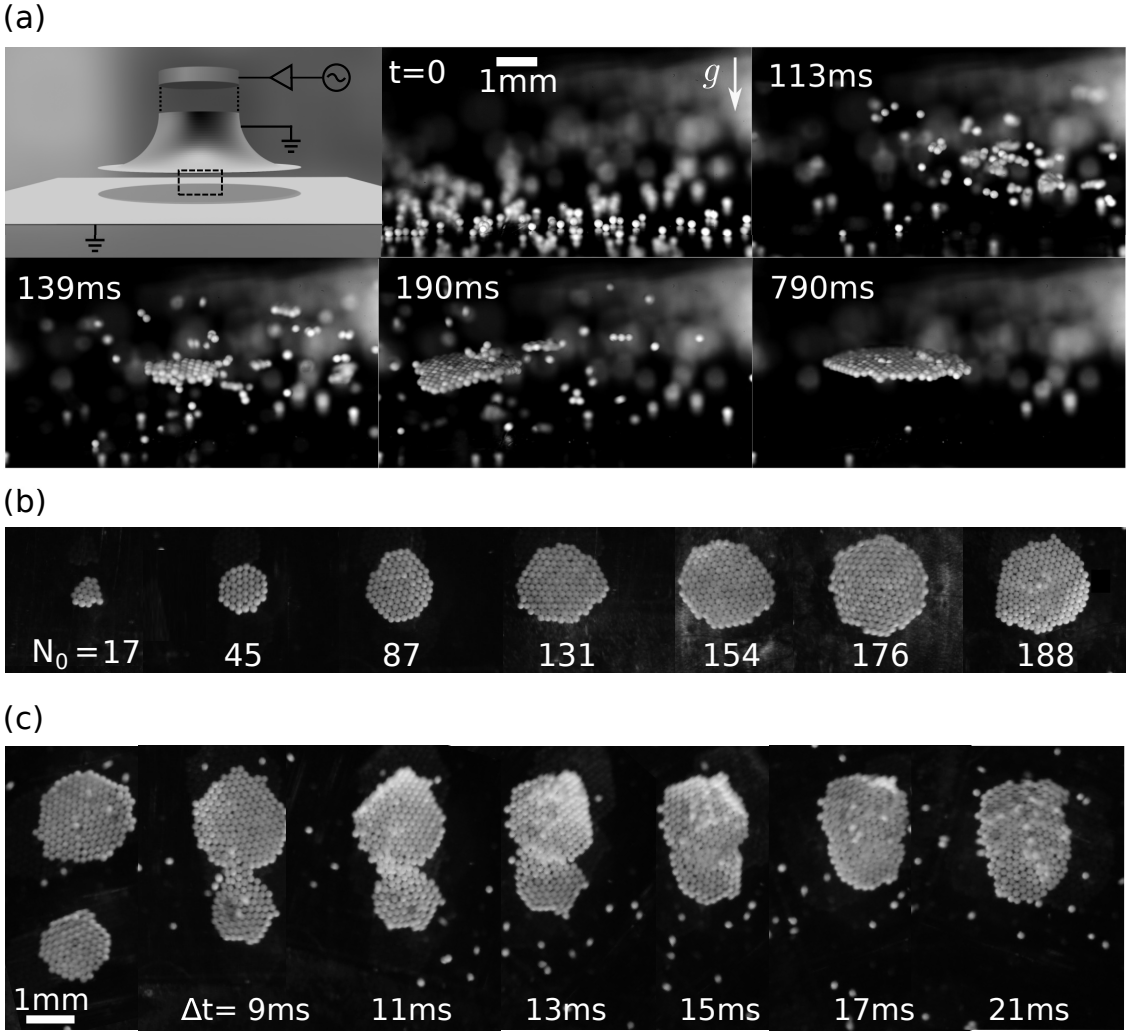

Figure 5.1: Self-assembly of granular rafts by acoustic levitation. (a) 3D drawing of setup and sequence of images (side view) showing the self-assembly of a granular raft from its constituent particles. Piezoelectric elements (cylinder) are attached to an aluminium horn to generate ultrasound (only base is shown). The grounded aluminium horn is spaced over a (grounded) indium tin oxide glass slide. The dashed black rectangle indicates the field of view in the subsequent still images. At $t = 0$, a standing wave is established between the transducer (above the top of the image) and reflector surface, which is covered with loose particles. These particles are picked up from the reflector surface by the primary acoustic force, and initially form small clusters, which travel in the underdamped acoustic environment until they coalesce to form a monolayer. (b) Self-assembled rafts composed of varying numbers of particles N_0, viewed from below. (c) Sequence of images from below, showing two rafts approaching each other and merging into a larger raft. Variations in brightness correspond to local curling of the raft out of plane.

ter image the particles from below. The transducer was driven by applying a sinusoidal signal of peak-to-peak voltage V_{pp} (100 - 400V) and frequency f close to the resonance frequency of the horn $f_0 = 45.65$kHz, produced by a function generator (BK Precision 4052) connected to a high-voltage amplifier (A-301 HV amplifier, AA Lab Systems). The transducer-reflector distance was adjusted via a translation stage to $\lambda_0/2 = 3.8$mm, establishing a single pressure node within the acoustic trap. Stable levitation is possible across a range of a few tens of Hz to either side of the resonant frequency. In order to reduce the effects of air currents, the entire setup was enclosed in a transparent acrylic box, with side-walls far from the experimental area of interest ($l \times w \times h = 24 \times 12 \times 18$ in^3).

We used polyethylene spherical particles (Cospheric, material density $\rho = 1,000\,\mathrm{kg\,m^{-3}}$, diameter $d = 180 - 200$ μm). The particles were stored and all experiments were performed in a humidity- and temperature-controlled environment (40-50% relative humidity, 22-24°C). The reflector was comprised of a grounded indium tin oxide (ITO) coated glass slide (thickness 1.1mm) secured to the top of an acrylic sheet (thickness 6.35mm). To mitigate tribocharging, both the reflector and the horn were grounded. The setup was cleaned with compressed air, ethanol and de-ionized water before each experiment. We neutralized any charges that remained on the reflector with an anti-static device (Zerostat 3, Milty). For each experimental run, particles were scattered onto the reflector from a spatula or, in some cases, inserted with a tweezer. Video was recorded with a high-speed camera (Vision Research Phantom v12) at 3,000 frames per second.

Lattice Boltzmann Simulations

We employed the Lattice Boltzmann method (LBM) to perform *ab initio* simulations of the sound field inside the acoustic cavity and its coupling with the levitated particles, hence taking into account the full extent of the fluid-structure interactions [95, 96]. This approach naturally includes the effects of viscous dissipation, momentum transfer due to multiple

scattering events, and anisotropy in the shape of the levitated objects.

LBM simulations of the acoustic cavity were carried out within the `waLBerla` framework [96]. A single relaxation time scheme with a viscosity matching that of air was used [95]. To compute inter-particle forces, a simplified simulation geometry with plane wave acoustic input and periodic domain boundaries was used. The ultrasonic horn was represented as a bounce-back boundary condition with time-dependent velocity, and the reflector as a stationary no-slip boundary.

We used the `PE` functionality of the `waLBerla` framework to simulate the interaction of particles with the acoustic field [97]. Hydrodynamic forces between the particles and fluid were handled with the partially-saturated cells method [98], which was found to be more stable than other momentum-exchange methods under acoustic conditions. We found that a local cell size of $D/15$, where D is the particle diameter, was sufficient for accurate force calculations.

In Fig. 6.1(b) we compare the results produced by the analytical approximation [42] and our LBM simulations for the secondary acoustic force due to scattering between two particles of radius $a \ll \lambda_0$ (Rayleigh limit) and volume V_p, in an imposed standing wave with acoustic energy density E_0. The data show close agreement, except very close to the particle surface, where the far-field scattering approximations break down and viscous effects become increasingly important [99]. Spherically symmetric particles in the same horizontal plane experience an azimuthally symmetric acoustic potential well (Fig. 6.1(a)). As a result, the secondary acoustic force along the horizontal direction x is attractive, driving the particles into direct contact (Fig. 6.1(b)). For particles approaching at some angle ϕ with respect to the horizontal, the interaction is more complex due to the quadrupole-like secondary acoustic potential (Fig. 6.1(a)). The result is a restoring force that brings particles back into the plane (Fig. 6.1(b)). In both cases the secondary acoustic force is short-ranged, acting on lengthscales of the particle radius. This gives rise to an effective cohesion and bending

rigidity of the raft, while at the same time stabilizing monolayer formation by penalizing particles for stacking into multiple layers. In contrast, the primary acoustic force, which sets up an acoustic potential well centered around the nodal plane of the standing wave in the cavity, has a characteristic length scale on the order of the wavelength of sound. Together, this means that the levitated granular rafts behave as effectively two-dimensional membranes that are weakly confined in three dimensions.

Raft Rotation

In addition to conservative acoustic forces, which assemble and stabilize the rafts, non-conservative forces can be generated if the transducer is driven with a frequency slightly larger than the resonance condition for levitation. These non-conservative forces can manifest as of out-of-plane, velocity-dependent forces, which originate from a phase lag between the motion of levitated objects in the cavity and the response of the cavity mode [100], and lead to vertical height fluctuations. In prior work we showed that such fluctuations can drive cluster rearrangements [87], or actuate modes of deformation within a cluster held together by secondary acoustic forces [88].

Our focus here is on fluctuating torques caused by off-resonance driving, where angular momentum is transferred to levitated objects, such that they spin around an axis perpendicular to the nodal plane. These spontaneous, fluctuating torques are frequently observed in levitated objects in air. Candidates to explain their origin include streaming flows in the acoustic cavity [101], velocity-dependent instabilities [100], and radial potential gradients in the levitation plane [102]. Although a full explanation of the origin of this acoustic torque is outside of the scope of the present study, here we show that the statistics of this oscillational instability can be controlled by the transducer frequency detuning $\Delta f/f_0$, such that they can be used to provide rotational driving to a levitated granular clusters.

To demonstrate and characterize this momentum transfer as a function of frequency

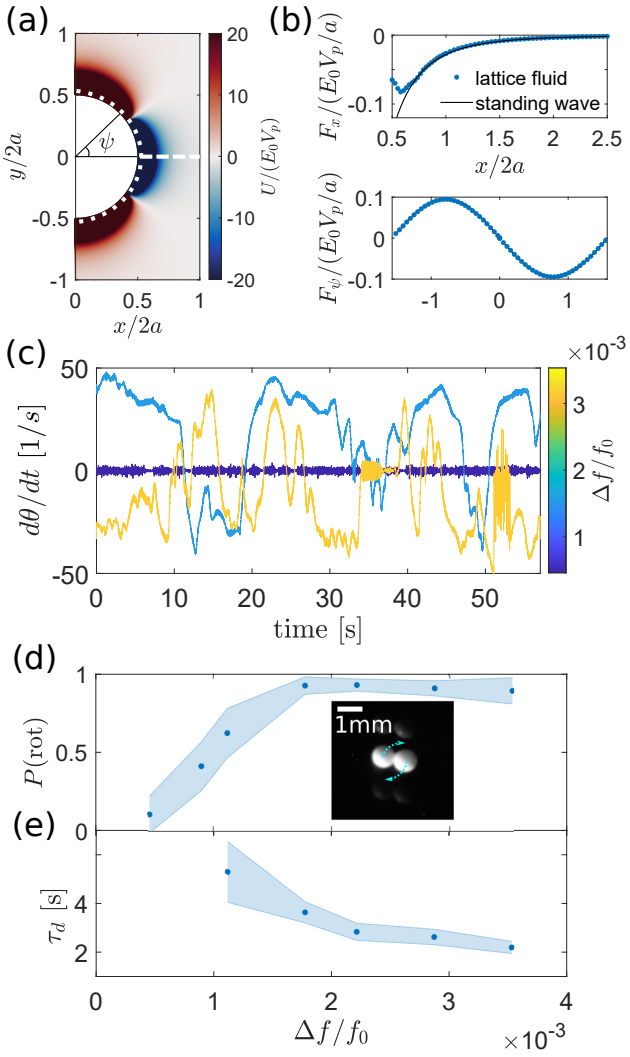

Figure 5.2: Secondary acoustic forces drive self-assembly and rotation of levitated granular rafts. (a) Secondary acoustic potential due to a particle with radius a, computed using a scattering expansion, normalized by the energy density of the cavity E_0, and the particle volume V_p. (b) Secondary acoustic force between a pair of particles, computed using a scattering expansion (black solid line), and using a lattice simulation (blue markers). (top) Horizontal force F_x between two particles as a function of distance x between their surfaces (dashed white horizontal line in panel (a)). (bottom) Angular force F_ψ on a particle displaced out of the nodal plane with angle ψ ($x/2a = 0.1$, dotted circular contour in (a)). (c) Example traces of rotation rate $d\theta/dt$ as a function of time, for a 2-particle dimer consisting of a pair of 700-810μm polyethylene particles, at different detuning parameters $\Delta f/f_0$. (d) Probability of dimer rotation P(rot) as a function of $\Delta f/f_0$. Shaded areas indicate the standard error. (e) Plot of the decorrelation time τ_d for the rotation rate of a pair of particles, as a function of $\Delta f/f_0$. Shaded areas indicate the standard error. Data not plotted for the smallest detuning parameters, for which there is no significant change in the rotation over time.

detuning $\Delta f/f_0$, we measure the in-plane angular rotation rate for a cluster consisting of two (700-810μm polyethylene) particles held together by the secondary acoustic force (data in Fig. 6.1(c), see inset to Fig. 6.1(d) for an image). We chose to use a pair of larger spheres as a minimal model for these rotational measurements, such that the longest dimension of the pair together was approximately equal to the diameter of the largest rafts. Results are qualitatively similar for pairs of smaller spheres, rigid rods, and the rafts, with differences in the maximum possible rotation rate and acceleration due to size-dependent viscous drag.

For the smallest $\Delta f/f_0$, the cluster does not complete full rotations, but simply rocks back and forth, occasionally stopping. As $\Delta f/f_0$ is increased, the cluster spins up to high angular speed, where both rotation rate and rotation direction vary stochastically when tracked over tens of seconds. However, this also includes stretches where the rotation rate increases roughly linearly with time, such that the imparted torque is nearly constant. Such stretches are used for our measurements on the rafts, reported below, which involve time intervals of typically less than one second. With increasing detuning, the probability of being in some continuously rotating state quickly approaches unity (Fig. 6.1(d)), while the typical lifetime of the state, measured by the time for the auto-correlation of the angular speed to decay to half its value, never drops below two seconds (Fig. 6.1(e)).

5.3 Results and Discussion

As the initially roughly circular rafts spin up, their rotational kinetic energy eventually becomes comparable to the particle binding energy and their shape begins to deform into ellipses (Fig. 5.3, Supplementary Movie 3). This plastic deformation process (see Appendix D for Voronoi diagrams of the raft interior) continues until eventual break-up. For sufficiently large rafts, plastic deformation is localized mainly to a small "neck" region that continues to extend as the raft rotates, eventually pinching off into two or more raft pieces (Fig. 5.3(a)). In contrast, for smaller rafts we observe a different mode of shape change (Fig. 5.3(b)): after

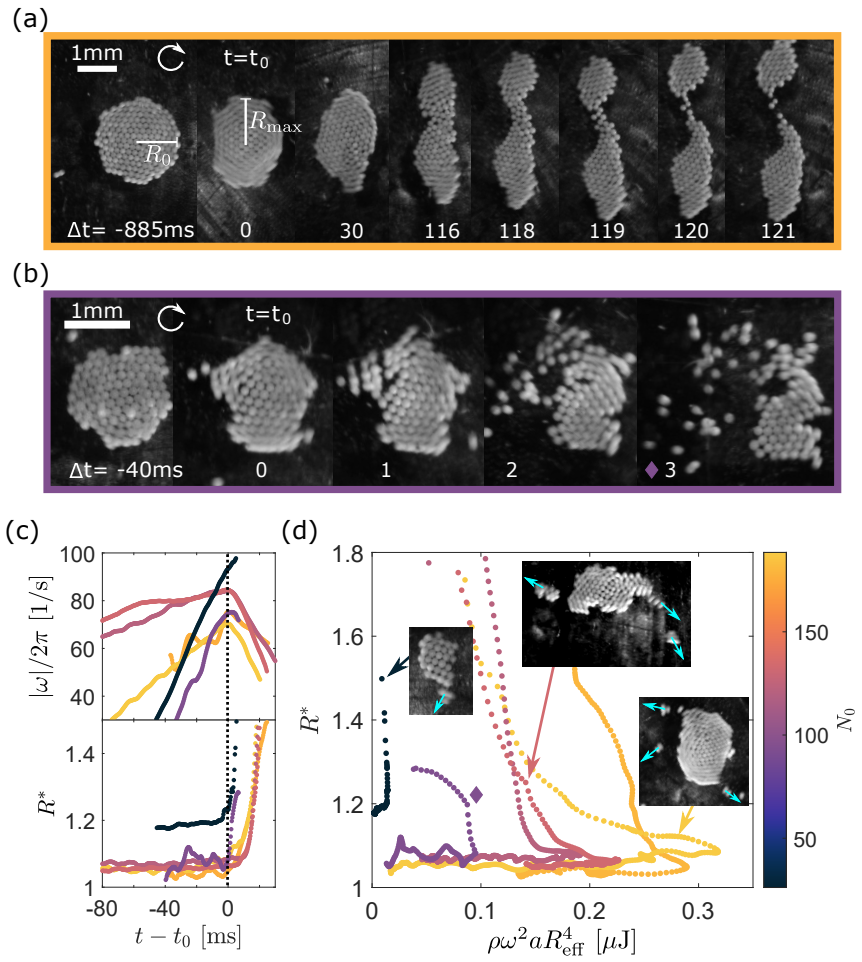

Figure 5.3: Levitated granular rafts exhibit emergent liquid-like behavior. (a) Sequence of images from below, showing the deformation of an initially circular raft that rotates in the clockwise direction. As the raft gains angular momentum, it elongates into an ellipse (at $t = t_0$, where the kinetic energy $\rho\omega^2 a R_{\text{eff}}^4$ is at its maximal value), then splits into two smaller rafts. The corresponding traces are shown in orange in (c) and (d) (second largest raft) (b) Sequence of images from below, showing the deformation of a smaller raft, at first also by elongating (at $t = t_0$), but then by shedding particles. The corresponding traces are shown in purple in (c) and (d) (second smallest raft), with the diamond marking the image at time $t = 3$ms in (b). (c) Example time-series of the absolute value of the number of rotations per second $|\omega|/2\pi$ (top), and the dimensionless shape parameter R^* of the levitated raft (bottom), as a function of the number of particles in the raft N_0, see part (d) for color key. Before t_0, the rafts spin faster without deforming; after t_0, the rafts change shape, shed weakly bound particles, and eventually split into multiple pieces. Raw data was filtered using a moving-average filter, with a width of 20 data points (7ms) to obtain the data in (c) and (d). (d) Evolution of the dimensionless shape parameter R^*, as a function of the kinetic rotational energy of the drop $\rho\omega^2 a R_{\text{eff}}^4$, for rafts with several different N_0. Inset images show the rafts at various points in the spinning process. After deformation into an ellipse, rafts can shed angular momentum by losing small clusters of weakly bound particles.

the rafts initially elongate into ellipses, they tend to continue to deform by shedding particles from their perimeter rather than via plastic deformation.

We now focus on the behavior well before break-up, where the rafts first begin to deviate from their circular shape and to elongate into ellipses. For a raft of total area A, which may change as the raft gains rotational kinetic energy, we measure deviations from circularity by the dimensionless parameter $R^* = R_{\max}/R_{\text{eff}}$. Here $R_{\max}$ is the semi-major axis of the raft at any given time, and $R_{\text{eff}} = \sqrt{A/\pi}$ is the effective radius of the raft's (time-varying) area A.

Comparing time-traces of the rafts' rotation rate ω and shape parameter R^* (Fig. 5.3(c)) reveals that the shape evolution is divided into two regimes. At first, ω increases nearly linearly with time, while R^* remains close to its initial value, indicating constant torque and angular acceleration without shape change – rotational kinetic energy is diverted into uniform stretching of the acoustic "bonds" between the constituent particles of the raft. In this regime, the raft perimeter is elastically stretched by increasing the interparticle spacing, without moving particles from the interior to the raft perimeter.

Once a maximum spinning speed has been reached, a point in time we label as t_0 in Fig. 5.3(c), the spinning speed ω decreases, and the shape parameter R^* increases sharply – the rafts become elliptical, and increase the total length of their perimeter by introducing particles from the interior to the raft surface. We use these differences in the microstructural evolution of the rafts to distinguish the two raft regimes as being dominated by elasticity before t_0, and being dominated by surface tension at and after t_0 (where "surface" here refers to the outer perimeter of the raft), in accordance with the nomenclature used in studies of the surface stresses and energies of thin films [103, 104].

In Fig. 5.3(d) we plot the evolution of R^* as a function of the rotational kinetic energy of the rafts E_{rot}. For our circular monolayer rafts $E_{\text{rot}} \sim \rho\omega^2 a R_{\text{eff}}^4$, where we have treated the rafts as discs with the thickness of one particle (diameter $2a$ and material density ρ),

and where we have omitted numerical prefactors of order unity. After reaching a maximum E_{rot}, the rafts lose rotational kinetic energy, visible as a change in curvature in the traces. After this point, R^* grows as the rotational kinetic energy decreases: further increases to the angular momentum of the raft serve to increase its moment of inertia, increasing its surface area as it elongates. While the raft continues to lengthen, ejection of weakly bound particles, which carry away some of the angular momentum, is reflected in sharp curvature changes of the traces in Fig. 5.3(d). The insets give examples.

The general shape of the traces in Fig. 5.3(d) exhibits striking similarity with what is found for rotating droplets of molecular liquids [76, 77, 105, 106]. For liquid drops, as with our granular rafts, shape is governed by the competition between rotational kinetic energy, E_{rot}, which acts to elongate the drop, and interfacial energy, E_{int}, which penalizes increases to the drop-air interfacial area (for rafts this is the perimeter area, i.e. the product of the perimeter and $2a$). Air drag can be neglected provided that the raft undergoes rigid body rotation [77, 107] (see Appendix E for measurements of the non-affine motion of particles in the raft, and Appendix F for an estimate of the magnitude of drag on the edge of the raft, which we show to be much smaller than the secondary acoustic forces binding particles to the raft edge). Although these aerodynamic forces are small compared to the in-plane forces holding raft particles together, these small forces can excite resonant out-of-plane bending similar to what is observed for thin, flexible disks that are spinning rapidly (see Appendix G for measurements and a qualitative discussion).

In liquids, as the spinning speed increases under constant torque, the droplets stay axisymmetric, and the energy ratio $\Sigma = E_{\mathrm{rot}}/E_{\mathrm{int}}$ is simply a function of the spinning speed ω until a value Σ_{max} is reached. Beyond this value there is a bifurcation away from the axisymmetric shape of the drop, such that the drop elongates along one axis, decreasing its rotation rate [76, 77]. Chandrasekhar [76] calculated the maximum ratio value $\Sigma_{\mathrm{max}} \approx 4$ for 3D droplets, a value that is found to increase to 12 for droplets in two dimensions [108].

As Fig. 3(d) implies, the ratio Σ for our rafts similarly increases up to some maximum value $\Sigma_{\max}$, beyond which there is a significant change away from the initially circular shape and the rotational kinetic energy decreases. Not directly apparent from the data in Fig. 3(d) (but discussed further below) is a slight isotropic expansion of the raft that occurs without significant change in R^* up to the point that $\Sigma_{\max}$ is reached. Here we note that this dilation serves to drive the particles toward a state where they can begin to plastically flow. For such flow, the important quantity is the energy associated with the creation of new interfaces.

Thus, by identifying the maximum E_{rot} before shape change occurs in data such as Fig. 5.3(d), we can extract the interfacial energy $E_{\text{int}} = E_{\text{rot,max}}/\Sigma_{\max}$ of the rafts, in analogy to liquid droplets. Using $E_{\text{int}} = \gamma a R_{\text{eff}}$, we define an effective surface tension γ:

$$\gamma = \frac{E_{\text{rot,max}}}{2a\Sigma_{\max}R_{\text{eff}}}\,. \tag{5.1}$$

Our data, plotted in Fig. 5.4(a), reveals that the effective surface tension of the granular rafts is extensive, and scales as a power law with the number of constituent particles, N_0. This scaling of the effective surface tension does not depend on the numerical value for $\Sigma_{\max}$, which we here take to be 12, in accordance with Ref. [108]. Within the scatter of the data, there is no consistent trend with the detuning parameter $\Delta f/f_0$, showing that the trap fluctuations do not affect the magnitude of attractive forces. The data are compatible with a power-law exponent between 1 and 3/2. Increasing the acoustic energy in the trap via the driving voltage of the transducer also proportionally increases the ratio γ/N_0, confirming that the observed effective surface tension is a direct product of acoustic scattering forces (Fig. 5.4(a) inset).

Unlike molecular liquids, our granular rafts can respond to tensile stresses by dilating slightly, and can thus respond elastically to an increase in rotational kinetic energy as long as $\Sigma < \Sigma_{\max}$. In this regime, the change in raft perimeter is less than 0.1 times the raft

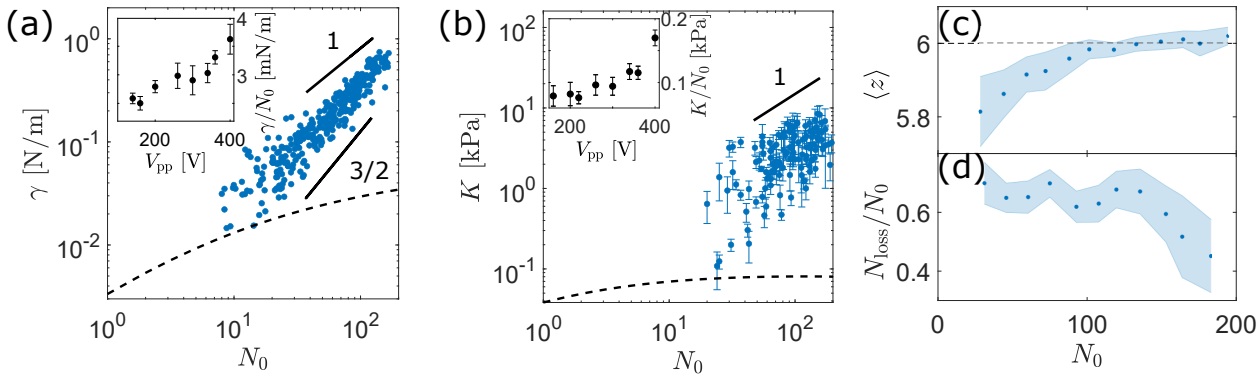

Figure 5.4: Contactless measurement of effective surface tension, effective elastic modulus, and microstructural properties. (a) Effective surface tension γ as a function of the initial number of particles in a raft N_0. Dashed line displays the prediction for γ obtained from integrating the acoustic force (Fig. 6.1(a)) over the raft body (within a multiplicative prefactor, see Appendix A). Data shown for transducer peak-to-peak driving voltage V_{pp} =300V. (inset) The slope of γ with respect to N_0, measured for different V_{pp}. Error bars indicate standard error. (b) Effective elastic modulus K, defined in analogy to the bulk modulus of a three-dimensional material, as a function of the initial number of particles in a raft N_0. Dashed line displays the prediction for K obtained from integrating the acoustic force (Fig. 6.1(a)) over the raft body, with a multiplicative prefactor (see Appendix A). Data shown on a log-log plot for transducer peak-to-peak driving voltage $V_{\mathrm{pp}} = 300$V. Error bars indicate error due to fitting the data. (inset) The slope of K with respect to N_0, measured for different V_{pp}. Error bars indicate standard error. (c) Average coordination number of particles in the raft interior $\langle z \rangle$, as a function of N_0. Dotted line indicates the coordination number for close-packed configurations in two dimensions. (d) Lost number of particles up to maximal plastic deformation, N_{loss}, normalised by N_0, as a function of N_0. Shaded regions indicate the standard error.

radius R_{eff}, such that the surface tension contribution to this elastic expansion is negligible. In Fig. 5.3(d) this slight isotropic expansion takes place before the upturn in R^* and can be used to extract the effective elastic modulus. For our rotating rafts, which we treat as discs with thickness $2a$ and circular face area A, the fractional increase in volume $V = 2aA$ from rest volume $V_0 = 2aA_0$ in response to an applied rotational pressure is

$$\frac{V}{V_0} = 1 + \frac{1}{2K}\rho\omega^2 R_{\text{eff}}^2 \,, \tag{5.2}$$

where we have assumed that the granular material is linearly extensible with effective elastic modulus K, which we define in analogy to the bulk modulus of a three-dimensional material, and particle material density ρ (see Appendix A for details, and Appendix C for examples of the data used to extract K). Our measurements of K, plotted in Fig. 5.4(b), show that the effective elastic modulus of the levitated granular rafts also scales with the number of constituent particles N_0 (but not with the detuning parameter, within the scatter of the data). Increasing the acoustic energy density of the trap also increases the ratio K/N_0 (Fig. 5.4(b) inset), confirming that the effective raft elasticity is directly controlled by the acoustic scattering forces between particles. For any driving amplitude, neither the effective elastic modulus nor the effective surface tension appear to saturate, even up to rafts with 200 particles. If this size-dependence were to hold even in the thermodynamic limit, the effective elastic modulus and effective surface tension would not be well defined. However, we expect that the long-range cohesive forces holding the raft together would be screened at large length-scales, with a length-scale that depends on the geometry of the acoustic trap. For sufficiently large rafts, the surface tension and elastic modulus would then converge to intensive values that depend on the screening length.

In the limit of very small droplets, the surface tension of small clusters of molecules and colloids at equilibrium also depends on the number of molecules in the droplet [109, 110]. In

these droplets, as the size decreases, the increasing curvature of the interface forces significant differences in the molecular structure, driving deviations in the surface tension from that of the elastic material. Such corrections become important when the size of this boundary layer becomes comparable to the droplet size. Previous work on small clusters in equilibrium has shown that these corrections come into play for three-dimensional clusters smaller than fifty particles, or clusters with a radius of approximately four particles. Such structural considerations thus seem unlikely to explain the size scaling observed here, where the effective surface tension does not appear to saturate up to rafts whose radii are greater than ten particles.

Our results instead show that the acoustic binding energy itself scales with the raft size. It is informative to compare this measured scaling of elastic constants with raft size to the results obtained by a pairwise acoustic scattering calculation. In particular, prior work suggested that in the Rayleigh limit ($a \ll \lambda$), the acoustic potential due to the presence of many particles can be calculated using a mean field approximation: the total acoustic potential on a probe particle is the pairwise (linear) sum of the potential due to each source particle [42, 111]. In this approximation, source particles do not scatter sound previously scattered by other source particles, and are therefore considered as independent acoustic scatterers.

However, the predicted mean field scaling of effective elastic constants with raft size (dashed lines in Fig. 5.4(a) and (b)) appears to have a power smaller than that observed in the experimental data (see Appendix A for details of the calculation). For very small rafts, our data extrapolates to the mean field prediction. However, as the number of particles in a raft increases, the predicted scaling flattens out, while the experimental data do not. This discrepancy suggests that for large, close-packed rafts (more than 10 constituents), multibody forces (from multiple scattering events) contribute strongly to the total secondary acoustic potential, even if the individual constituents are well within the Rayleigh limit. We

note that the addition of an acoustic screening term would effectively reduce the number of source particles contributing to the total acoustic field at the probe particle, since screening introduces a length scale beyond which particle interactions are negligible. On the contrary, our results show that acoustic binding does not plateau as raft size is increased. Therefore screening effects, if present, occur at longer length scales than probed here.

These non-pairwise effects point to the fact that the rafts have entered the regime where source particles can no longer be treated as independent acoustic scatterers. In this regime, the non-additive forces could arise from significant higher-order scattering between the close-packed particles, significant phase delays in the acoustic field between different parts of the raft, or alterations to the modal structure of the acoustic cavity due to the presence of the raft. Ultimately, our data highlight the current lack in understanding of secondary acoustic forces beyond lowest-order scattering expansions.

As a counterpart to our observations on the overall shape-change of the rafts, we turn now to the size-dependence of micro-structural deformations in the rafts. Since the rafts allow for direct visual access to the configuration of individual constituent particles, we are able to track the micro-structural basis of their deformation throughout the course of their spin-up. Our results, plotted in the upper half of Fig. 5.4(c), reveal that the largest rafts deform without changing their average connectivity: rafts composed of more than 100 particles rearrange their interior, without changes in the average coordination number $\langle z \rangle$, similar to sheared colloidal crystals [112, 113]. However, as the rafts decrease in size, they deform by decreasing the average number of neighbors between particles in the elastic. This loss of stability in the raft interior results in changes in the mode of deformation past yielding. Plotting the fractional number of particles lost by the raft, N_{loss}/N_0, as it deforms (Fig. 5.4(d), example images in Fig. 5.3(a) and insets of Fig. 5.3(d)) reveals that small rafts tend to change shape by shedding particles rather than through rearrangements of their interior: small rafts appear brittle rather than ductile, as prefigured by the overall loss of

connections in the interior of small rafts before their eventual failure.

The existence of such a cross-over from brittle to ductile behavior is in line with general considerations based on the relative size-dependent energetic costs of plastic deformation and fracture for small rafts. The cost of plastic deformation is, at a minimum, the energy required to create a dislocation pair in a previously crystalline domain, which scales as $E \ln R_{\text{eff}}$ [114], where E is the Young's modulus of the material. Assuming that E and K scale similarly with N_0 for our levitated granular rafts, the energy cost of a dislocation pair scales as $N_0 \ln N_0$. The actual cost may be higher: measurements of the flow stress for metallic nanopillars suggest that the energy for plastic deformation increases drastically for small crystals, as they may have an initially low dislocation density [115, 116], or else rapidly exhaust their available dislocation sources [117]. On the other hand, the energetic cost of fracture is the energy required to create a new interface (whose area is on the order of the raft radius times the particle diameter $2a$), which scales as $\gamma N_0^{1/2}$ or, using the essentially linear dependence of γ on N_0, as $N_0^{3/2}$. For small N_0 it is therefore favorable to fracture rather than to create dislocations. The size-dependence of the raft elastic properties thus also results in differences in the micro-structural modes of rearrangement.

5.4 Conclusions

We have used acoustic levitation to contactlessly assemble, drive, and measure the mechanics of active granular rafts. Here, these "soft" granular rafts have attractive forces comparable to applied rotational tensions. Acoustic rotation thus offers the opportunity to tune through a wide range of driven behaviors in an inertial soft solid, from isotropic dilation, to extreme shape change and finally catastrophic failure.

The observed size-dependence of the effective surface tension and elastic modulus of the rafts pose a particular challenge to the theoretical modeling of secondary acoustic forces. Such modeling [42, 89] currently relies on perturbative scattering expansions, which are

appropriate in the limit of dilute Rayleigh scatterers, where sound is scattered once between independent particles. These assumptions are valid in the regime where individual particles are spaced far apart compared to the particle size, and are much smaller than the sound wavelength. However, these assumptions do not capture the dependence of the effective surface tension on particle number that we find for close-packed rafts, which can reach a sizeable fraction of the sound wavelength. Our results suggest the need for a systematic theoretical exploration of regimes in particle size and packing density in which acoustic interactions can no longer be treated as pairwise. This size-dependence also plays a role in governing both the elasticity and plasticity of these acoustic solids. In particular, the size range of our rafts spans the transition where small rafts deform by fracturing into pieces (similar to brittle failure), while larger rafts can respond to external stresses by plastically deforming their interior. Our results demonstrate how acoustically levitated rafts can be used to investigate the mechanical properties of solids bound by non-pairwise interactions. Consequences of non-pairwise forces for defect-mediated plasticity have been theorized in other systems [118, 119, 120], but are difficult to observe experimentally.

In addition, the size-dependence of the effective elasticity and cohesion of our levitated rafts is highly reminiscent of gravitationally-bound granular materials, where power-law gravitational forces lead to attractive forces that increase with the object size. This resemblance to gravitational forces could open the door to a more detailed understanding of the dynamics of other rapidly rotating clusters, such as rubble-pile asteroids, which are beginning to be systematically explored from a granular perspective [121, 122, 123]. From these rubble piles, fission by rotation is thought to be a pathway to the creation of small binary asteroids [67, 124]. In this case, spinning monolayer rafts may serve as a model system for the dynamic evolution of the equatorial plane in rapidly rotating astronomical granular materials. Our experiments thus suggest a path toward the study of "tabletop asteroids".

5.5 Additional material

In this section, we present additional material that supplements the main body of Chapter 5 (adapted from Lim, Melody X., Bryan VanSaders, Anton Souslov, and Heinrich M. Jaeger, "Acoustically levitated granular rafts." arXiv preprint arXiv:2106.09765 (2021)). Included is a derivation of the theoretical ansatz in Fig. 5.4, a list of the number of observations for the data in Fig. 5.2, details on the elastic modulus measurements, measurements of the raft plasticity during deformation, measurements of the nonaffine motion during breakup, estimates of the effect of air drag, and measurements of the out-of-plane bending of the raft during rotation.

Appendix A: Acoustic potential due to a disc composed of point particles

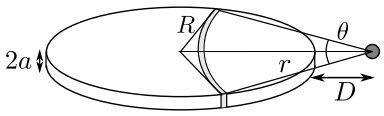

Figure 5.5: Schematic of the coordinate system for calculating the potential on a point particle due to a disc composed of point scatterers. The point particle, which has radius a, is placed in plane with the disc (which has radius R and thickness $2a$), and at a horizontal distance D from the edge of the disc.

We consider the potential force on a point (test) particle due to a disc composed of point scatterers with radius a (such that the disc has height $2a$), each of which has a pairwise interaction with the test particle. For a disk composed of a monolayer packing of particles, the number density of point scatterers is $\rho = 1/2\pi a^3$. We compute the total potential U on the point particle as as the sum of the potentials u due to the disc constituents. This pairwise acoustic potential u, plotted in Fig. 2 of the main text, is azimuthally symmetric, and depends on the radial distance between a pair of particles r, as well as the polar angle between them, ψ.

For a test point placed at horizontal displacement D and zero vertical displacement from

the edge of the disc (see Fig. 5.5 for a schematic), the set of points on the disc that are a distance r from the test point forms an arc, with arclength θ and infinitesimal volume $ar\,dr\,\theta$. Using the cosine rule, we have

$$R^2 = r^2 + (R+D)^2 - 2r(R+D)\cos(\theta/2)$$
$$\implies \theta = 2\arccos\left(\frac{r^2+2RD+D^2}{2r(R+D)}\right).$$

Within this arc-volume, all constituents are at distance r from the test particle. The total acoustic potential due to the disc can thus be derived by integrating the contributions of each arc-length volume over the area of the disc. This can be expressed as a one-dimensional integral over r:

$$U(D) = 4a\rho\int_D^{2R+D} dr\, u(r) r \times \arccos\left(\frac{r^2+2RD+D^2}{2r(R+D)}\right) \tag{5.3}$$

We carry out this integration numerically for different values of R, with $D = 2a$, to produce the dashed line in Fig. 4(a) of the main text. The mean-field prediction for the acoustic elastic modulus (dashed line in Fig. 4(b)) is the second derivative of this expression with respect to the coordinate D, evaluated at $D = 2a$, which we also carry out numerically.

Appendix B: Observation number

Table 1 lists the number of observations of spinning dimers that were combined for the data in Fig. 2(d) and (e) of the main text.

$\Delta f/f_0 \times 10^{-3}$	number of observations
0.46	17
0.89	32
0.96	26
1.77	20
2.21	20
2.87	35
3.53	30

Table 5.1: Number of dimer pairs observed for Fig. 2(d) and (e). Each dimer was observed for 23 seconds.

Appendix C: Measurement of effective elastic modulus

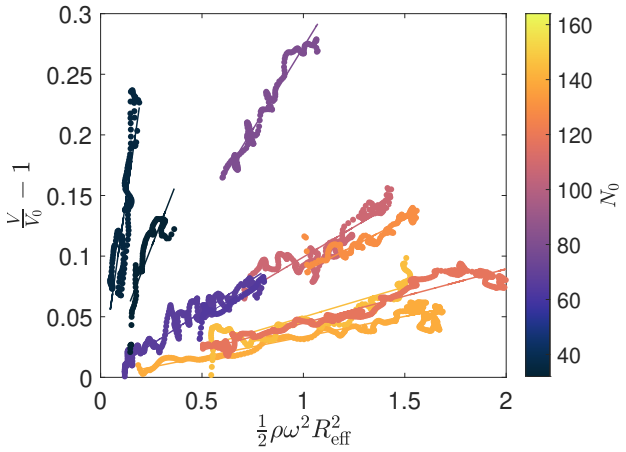

Figure 5.6: Example raw data for the calculation of K (dots). The fractional change in volume of the raft $V/V_0 - 1$ is plotted as a function of the rotational pressure, $\frac{1}{2}\rho\omega^2 R_{\text{eff}}^2$. Color indicates N_0. The best fit line is indicated as a solid line through each data set. Data has been smoothed with a moving average filter, with width 10 data points (3ms).

In order to make use of Eq. 5.2 and extract the effective elastic modulus K of the droplets, we plot the fractional change in raft volume $V/V_0 - 1$ (where $V = aA$, the product of the circular face area of the raft and its thickness) as a function of the rotational pressure $\frac{1}{2}\rho\omega^2 R_{\text{eff}}^2$ (example data shown in Fig. 5.6). Here, we determine V_0, or equivalently, the initial area of the rafts (when $\omega = 0$) times their thickness, by fitting the data to lines, and extracting the intercept. The data is then fitted to a line, whose slope then gives $1/K$. Error bars in

Fig. 5.4(b) reflect the least-squares error in the fit coefficients.

Appendix D: Plasticity during raft deformation

In order to assess the relative roles of plasticity and elasticity during the raft deformation past $\Sigma_{\max}$, we measure the crystallinity of the raft interior (via the particle coordination number, measured using a Voronoi diagram) throughout the course of its rotational break-up. Example snapshots of the Voronoi diagrams are shown in Fig. 5.7(a) and (b), at different points throughout the raft deformation. The Voronoi statistics for the raft in Fig. 5.7(a) are summarized in Fig. 5.7(c), which plots the evolution of the number of particles with six neighbours in the raft interior n_6, as a fraction of the total number of particles in the raft $N(t)$, together with the shape parameter R^* as a function of time. At first, the shape of the raft does not change (constant R^*). At the same time, in response to the growing spinning speed, n_6 slowly decreases. As the rotational speed of the raft increases, a small number of defects are accumulated in the interior. During this phase of raft spin-up, the stresses are predominantly dilational, which do not motivate the glide of dislocations.

The shape of the raft then changes modestly, resulting in an also modest drop in n_6 around 30ms. After this point, the raft retains its new elongated shape for a considerable period of time. During this period of time, n_6 grows, and in fact exceeds the value of n_6 observed for the initially circular raft: the crystal structure of the raft is now able to relax and remove defects, in a form of rotational annealing. The elongation of the raft into an ellipse breaks the azimuthal symmetry of the rotational stress, introducing shear fields to the raft interior which sweep dislocations to the raft boundaries. Finally, the rotational energy again exceeds the binding energy of the drop, which then elongates to $R^* = 3$, and pinches off into two drops. This extreme elongation rapidly generates defects and drastically lowers n_6. Again, after the pinch-off, n_6 rises, indicating that the remaining two sections of the raft have eliminated their defects through the creation of additional surface, and now

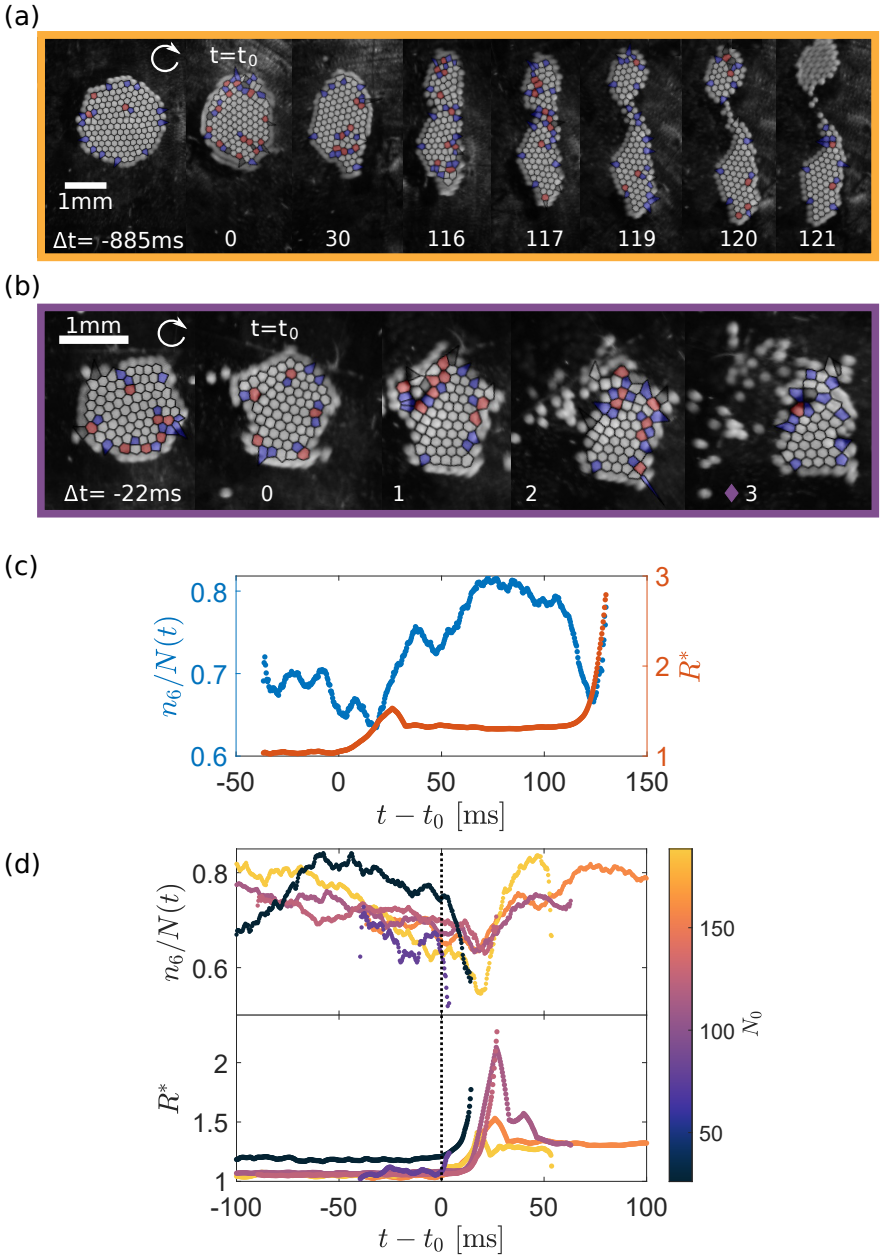

Figure 5.7: Voronoi construction reveals the onset of plasticity during raft deformation. (a,b) Images in Fig 3(a) of the main text, overlaid with the corresponding Voronoi diagram of the raft interior. Cells in the Voronoi diagram are overlaid with the corresponding number of sides of the polygon: particles with five neighbours are shaded blue, particles with six neighbours white, and particles with seven neighbours red. (c) (left axis) Plot of the number of particles in the raft interior with six neighbours n_6, divided by the total number of particles in the raft $N(t)$, as a function of time (both n_6 and N are tracked at every frame of the drop evolution), for the raft pictured in (a). (right axis) Raft shape parameter R^* as a function of time. (d) (upper) $n_6/N(t)$ as a function of time, for several different initial raft sizes N_0. (lower) R^* as a function of time.

have well-ordered interiors.

Further examination of $n_6/N(t)$ and R^* as a function of time, for several different raft sizes, (Fig. 5.7(d)) confirms these trends for large rafts: raft shape changes are accompanied by a temporary decrease in n_6, which then recovers after a short period in which the raft crystal structure relaxes. In contrast, since the smallest rafts tend to change shape by shedding large fractions of their constituent particles, $n_6/N(t)$ drops sharply at t_0, and does not return to a close-packed state after the droplet shape change. In all cases, we observe a gradual decrease in $n_6/N(t)$ during the spin-up process, indicating that the dilation of the raft before global-shape change generates defects in the raft interior. This gradual decrease is marked by fluctuations that correspond to the appearance and disappearance of several defect pairs.

Appendix E: Nonaffine particle motion

One of the assumptions underlying the derivation of Eq. 5.1 is that the raft rotates as a rigid body up until the point where it changes shape, i.e. that there is negligible non-affine motion of the particles in the raft for $E_{\rm rot} < E_{\rm rot,max}$. In order to assess the validity of this assumption, we measure the position of particles in the raft at the start and end of the spin-up process (the end of the spin-up process defined as one frame, or 0.33ms, before the raft reaches its maximum rate of rotation). Once we correct for the rigid-body translation and rotation of the cluster, we then construct the displacement vector between all matching particles in the raft.

Example particle positions and displacements are shown in Fig. 5.8(a–c): the vast majority of particle displacements have magnitude smaller than a particle radius. Quantitatively, we resolve the displacements into the radial and azimuthal directions, and plot the mean directional magnitudes (averaged over all particles in a raft) as a function of N_0 (Fig. 5.8(d)). We find that the average displacements in the radial and tangential directions are of similar

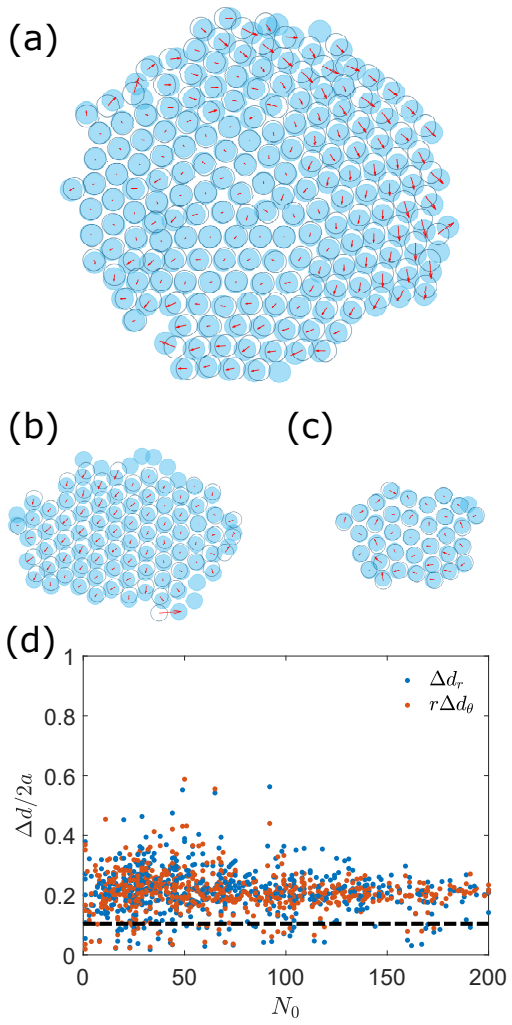

Figure 5.8: Nonaffine motion of particles before breakup. (a–c) Comparison of rotation-corrected particle positions at the start of spin-up (dark blue circles), and just before shape change (i.e. one frame before $E_{\text{rot}} = E_{\text{rot,max}}$, plotted as light blue filled circles), for three rafts of varying size. Red arrows show the local displacement field from initial to final particle position. (d) Plot of average displacement of particles (averaged over all particles in the raft) during spin-up Δd as a function of N_0, normalized by the particle diameter $2a$. Displacement has been resolved into the radial (Δd_r, blue data points), and azimuthal ($r\Delta d_\theta$, orange data points) directions. Black dashed line indicates the noise floor for particle tracking.

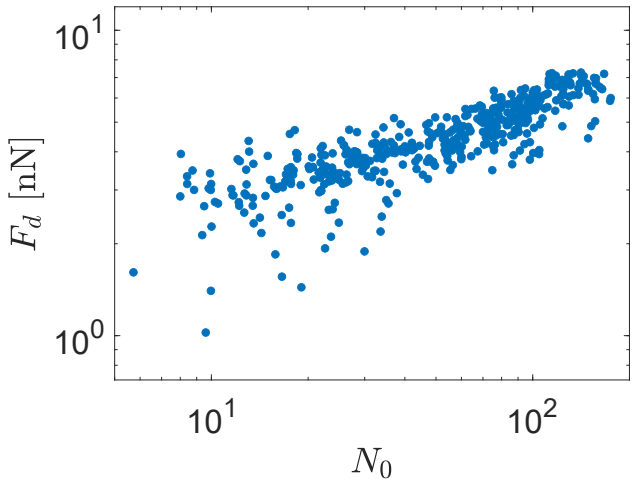

Figure 5.9: Drag force F_d on a particle on the perimeter of a raft, estimated using a linear drag model, as a function of the total number of particles in the raft N_0.

magnitude, roughly half a particle radius. This is the case even in the larger rafts, where there can be some long-wavelength collective motion as the raft dilates (see, e.g., Fig. 5.8(a)). However, the magnitude of this motion stays well below a lattice spacing (the membership of particle nearest neighbor shells is not disturbed). Thus, the rafts remain solid-like, rigid, and do not exhibit evidence of internal shear before the onset of deformation.

Appendix F: Estimate of Stokes drag on raft perimeter

In order to assess the effect of air drag and compare it to the acoustic binding force between particles, we calculate the viscous force on a particle at the edge of the raft, using a linear drag model:

$$F_d = 6\pi\eta a v$$

where η is the viscosity of air, a is the radius of an individual particle, and $v = R_{\text{eff}}\omega$ is the linear velocity of a particle on the perimeter of a raft with radius R_{eff}, rotating with angular velocity ω. This model for F_d (measured at the moment of shape change, where ω is largest,

yields measurements that are of order 1-10 nN (Fig. 5.9).

For comparison, we need to estimate the magnitude of the secondary acoustic forces between a pair of particles that compose the raft. One estimate is provided by the centripetal force required to keep the particle attached to the edge of the raft, $F_c = m\omega^2 R_{\text{eff}}$. Since the particles do not detach from the raft, such an estimate serves as a lower bound on the secondary acoustic force acting on a single particle. The ratio of this centripetal force to the drag force is $F_c/F_d = \frac{2\rho\omega a^2}{9\eta} \approx 50$. Alternatively, Fig. 2(b) shows that the radial restoring force between a pair of particles is approximately 0.1, in units of $E_0 V_p/a$, where E_0 is the energy density of the cavity, V_p is the particle volume, and a is the particle radius. To convert the values in Fig. 2(b) to a force in Newtons, we infer the energy density from the measurement of surface tension. Fig. 4(a) compares the surface tension, measured from the experiments, to an analytical calculation obtained by integrating the acoustic potential U over a disk (black dotted line). Using $\gamma \sim U/a^2$, the fit between this analytical calculation and the experimental data has a single fitting parameter, corresponding to E_0. Substituting this value of E_0, we find that the secondary acoustic force for a particle on the edge of the smallest rafts (10-30 particles) is of order 1μN, or two to three orders of magnitude greater than the estimated drag force. Fitting the analytical calculation to the surface tension of the largest rafts increases the estimated secondary acoustic forces to roughly 100μN. Again, this estimates provides a lower bound on the acoustic binding between particles in the raft. The raft shape changes and thus the data on the effective surface tension and elastic modulus are thus unlikely to be affected by air drag.

Appendix G: Rotationally activated out-of-plane bending

While the effective in-plane surface tension and effective elastic modulus of the rafts are controlled by the in-plane component of the secondary acoustic forces (Fig. 6.1(a)), the rafts have other elastic constants for out-of-plane deformations, which are controlled by the

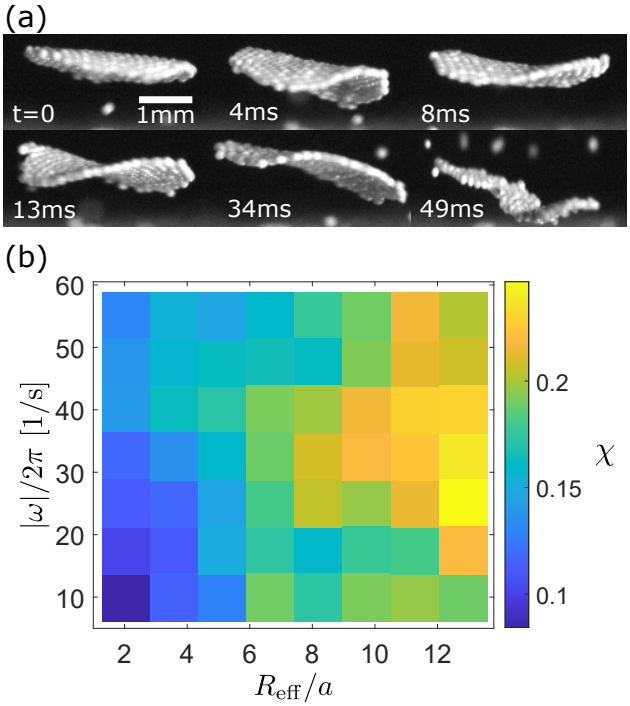

Figure 5.10: Rotation activates out-of-plane bending in levitated granular rafts. (a) Sequence of side-view images showing the rotation of a raft, which eventually elongates into an ellipse (t=34ms). During the process of spinning up, the raft deforms significantly out of plane. (b) Raft concavity χ (value shown by colorbar, see text for definition), as a function of the absolute rotational frequency $|\omega|$ and raft radius R_{eff}/a. The data represents observations of 60 (independently self-assembled) rafts. The 95% confidence intervals for χ are approximately constant as a function of $|\omega|$ and R_{eff}/a, and do not exceed 0.02 for any measurement.

out-of-plane components of the secondary acoustic force (Fig. 6.1(b)). As a result of this out-of-plane bending modulus and their membrane-like, effectively two-dimensional nature, levitated granular rafts can strongly deform out of plane (Fig. 5.10(a), see Supplementary Movie 4 for dynamics). The smallest rafts remain planar as they rotate, exhibiting rocking motions that tilt the raft in and out of the levitation plane. However, for the largest rafts, increasing the rotation rate of the rafts gives rise to saddle-like bending modes, which can start waves that travel azimuthally around the raft while it rotates.

In the following, we discuss these transverse bending modes and waves at raft rotation speeds in the regime where the rafts remain circular (before they deform and break up). To characterize these waves, we make use of the fact that the bending modes appear as saddle-like, nonconvex structures when viewed from the side. We thus use the concavity of the (thresholded) black and white side-view images as a proxy for the out-of-plane bending of the raft. Given a raft shape with projected area A_I, whose corresponding convex hull has area A_v, we define the concavity χ as $\chi = 1 - A_I/A_v$. For planar objects viewed from any angle, the convex hull of the image is almost completely filled by the original image, and so χ is close to zero.

Measurements of χ as a function of the absolute rotation rate $|\omega|$ and normalized raft radius R_{eff}/a reveal that rotation activates out-of-plane bending nonmonotonically (Fig. 5.10(b)). The smallest rafts remain relatively flat as they rotate faster, with a weak increase of χ. For larger R_{eff}/a, more out-of-plane degrees of freedom are available, and the overall concavity at first increases with $|\omega|$, up to $|\omega|/2\pi \simeq 30$Hz, but then decreases for faster spinning.

Similar out-of-plane bending modes occur in thin, rapidly spinning elastic disks and membranes, where they originate from nonlinear interactions between the shape of an elastic object, and the shape-dependent aerodynamic drag on it. These nonlinear interactions result not only in a drag force, but also an additional lift force, whose magnitude is proportional to both the angular speed and the out-of-plane displacement of the raft [125]. Even a very

small lift force (compared to the forces holding the disk together) can then excite and amplify vibrational modes in the form of traveling waves around the disk edge [126, 127].

Since the measured effective elastic modulus of our membrane-like rafts is an order of magnitude smaller than in most previously observed spinning disks [127, 128, 129], increasing ω can tune through a wider range of behaviors. In particular, for the larger rafts we can reach a regime where the inertial forces during rotation increase the effective raft tension, to the point that this reduces the amplitude of transverse undulation. This rotationally induced reduction in out-of-plane motion has been observed previously only in the limit of membranes that are extremely thin relative to their radius, such that the bending stiffness is negligibly small [130, 131, 132].

CHAPTER 6

EDGES CONTROL CLUSTERING IN LEVITATED GRANULAR MATTER

6.1 Introduction

Shape provides an important means by which to tune key properties of dense aggregates[1], whether their packing fraction [13, 14, 15], contact configuration [16, 17, 18, 19, 20], or mechanical properties [21, 22, 23, 24, 25, 26, 27]. In each of these cases, the shape of a particle determines the global properties of an aggregate by modifying both the geometry of the packing and local inter-particle contacts. These local contacts play a particularly important role in jamming, where the precise type of contact between faceted shapes may dramatically change the mechanical stability of a given packing. In addition, breaking spherical symmetry in a dense granular packing produces a coupling between normal forces and torques on the single-grain level.

In addition to local contact forces and geometry, which produce effects at the level of a single contact on a grain, longer-range particle interactions also play an important role in the properties of a granular material. Previous work has shown that adding weakly attractive dipole-dipole interactions to a granular material provides a means of self-organisation for the force chains that form under compression, thus strengthening the force network that forms as a result [28]. Alternatively, longer range forces can drive clustering [30, 31] and particle motion [32, 33]. However, the relation between attractive forces, particle shape, structure, and mechanical properties remains to be fully understood.

In this Chapter, we take a first step towards this goal by producing shape-dependent, tunable attractive forces between granular materials using acoustic levitation. Previous work

1. This Chapter is based on Lim, Melody X., Kieran A. Murphy, and Heinrich M. Jaeger, "Edges control clustering in levitated granular matter." Granular Matter 21, no. 3 (2019): 1-8.

on acoustically levitated particles has focused on the force between levitated particles with a high degree of symmetry, such as spheres [38, 39, 40, 41**?**], cylinders [43, 44, 45], or between smooth deformable objects such as liquid drops [46] and bubbles [47]. Other work has focused on viscous and thermal effects in the acoustic force [133, 39, 134].

We present results for a wide range of particle shapes and constituent materials, showing that particles are attracted to one another along sharp edges. Using finite element simulations, we demonstrate that the strength of the inter-particle attraction is controlled by the sharpness of particle features. These bonds also support robust hinge-like motions, which we suggest are oscillations about a minimum in some energetic landscape. Finally, we consider the structure of clusters formed in the acoustic field. We suggest that the unique structures we observe are due to a combination of the highly anisotropic acoustic forces, packing efficiency, and stabilisation from local inter-particle contacts.

6.2 Methods

We levitate grains using the setup illustrated in Fig. 6.1(a), as detailed in Chapter 2. Here, we drove the transducer at frequency f by applying an AC signal with peak-to-peak voltage 200V. As shown in previous work [87], driving the acoustic trap with frequency slightly above resonance induces active fluctuations in the levitated particles. In turn, these active fluctuations drive cluster rearrangements. In this case, we induce active fluctuations by detuning the trap to $f = 45.76$kHz, or $\Delta f/f_0 = 2.5 \times 10^{-3}$. We note that within the range of frequencies used for detuning, there is no noticeable change in the displacement characteristics of the transducer.

A wide range of particle shapes and constituent materials can be levitated in this setup. We take advantage of the naturally cubic shape of salt grains (material density 2 160 kg m^{-3}) to levitate isotropic cubes (Fig. 6.1(c)). Alternatively, we levitate spheres (polyethylene, diameter 710-850μm, Cospheric, material density 1 000 kg m^{-3}). Finally, in order to create

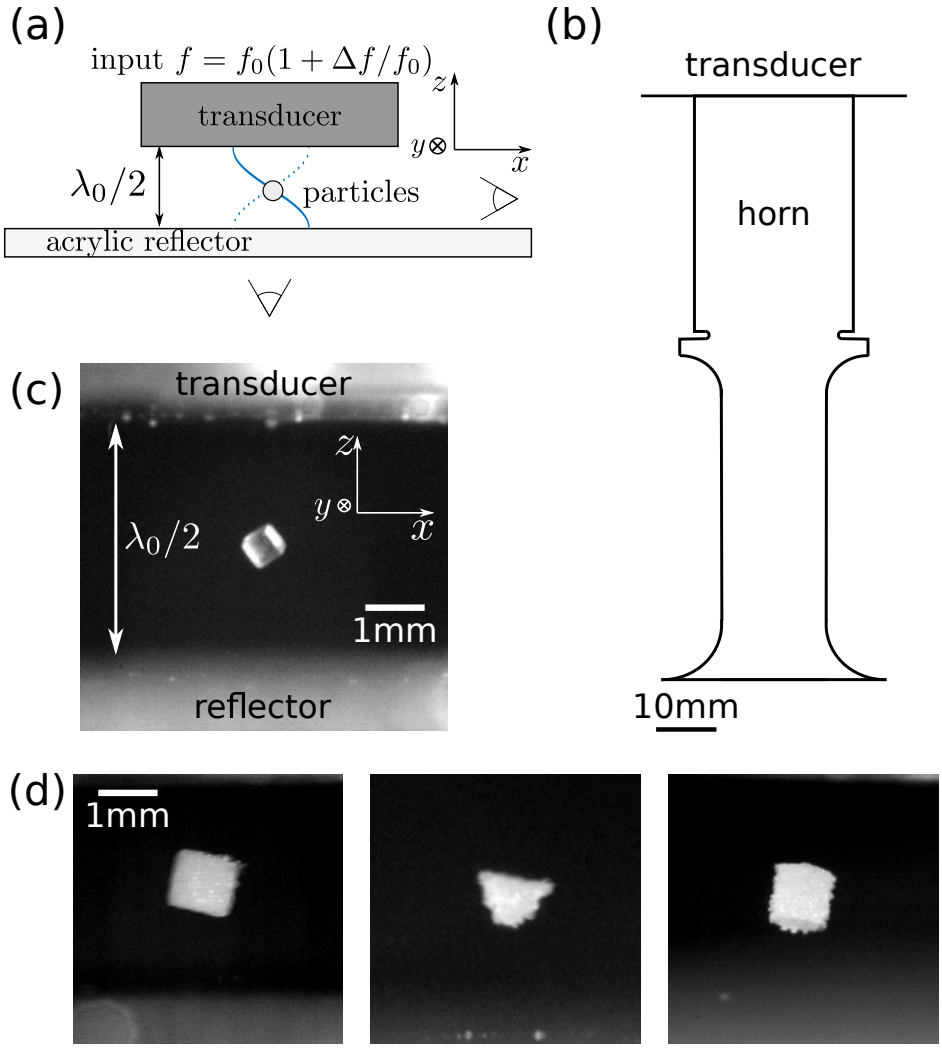

Figure 6.1: **Experimental setup.** (a) A schematic of the apparatus. An ultrasound transducer generates sound waves in air (speed of sound $c_s = 343m/s$). The transducer consists of a commercial ultrasound transducer, the output of which is amplified by an aluminium horn bolted onto its base. The distance between the base of the horn and a transparent acrylic reflector is chosen so as to create a pressure standing wave with a single node, with frequency $f_0 = 45.65kHz$ and wavelength $\lambda_0 = c_s/f_0$. Particles are levitated in this pressure node, and can be imaged from the side or from below. The driving frequency f of the trap can be detuned by $\Delta f \equiv f - f_0$, inducing active fluctuations in the levitated particles [54, 87]. (b) A scale drawing of a cross-section of the combined transducer and horn (which are circularly symmetric). Particles are levitated beneath the bottom surface of the horn. (c) A grain of table salt levitated in the acoustic trap, imaged from the side. (d) 3D printed particles, levitated in the acoustic trap. From left to right: cube (1mm side length), tetrahedron (1mm side length), cylinder (1mm diameter, 1mm height)

particles with controlled shapes and sizes, we 3D print cubes (1mm side length), tetrahedra (1mm side length), cones (1mm base diameter, opening angle 60°), and cylinders (diameter 1mm, height 1mm). All particles are printed in hard UV-cured plastic (Objet VeroWhite, material density 1 180 kg m^{-3}), on an Objet Connex 350 printer. Note that the particles are printed in stacked laminae (thickness $\sim 50\mu$m), producing highly frictional faces (Fig. 6.1(d)).

6.3 A pair of cubes: experimental observations

A single particle in the acoustic trap rotates freely about its centre of mass, regardless of shape and material, confined by the primary sound field in the vertical direction. When a second particle is introduced, the primary sound field confines it to the same levitation plane as the first particle. In addition, acoustic scattering due to the presence of the first particle produces an additional in-plane force, which we refer to as the secondary acoustic force. This secondary (induced) acoustic force, which for deformable particles is known as the secondary Bjerknes force [135**?** , 136], stabilises compact clusters. For spherical (isotropic) particles, the acoustic force follows the axisymmetry of the particles in the levitation plane, such that spherical particles cluster into a close-packed, two-dimensional lattice [87]. However, since the acoustic force is generated by scattering, anisotropy in the particle shape results in anisotropy in the acoustic force.

Due to this anisotropic force, when a second cube is introduced to the acoustic trap, the freely rotating cube is stabilised: a pair of levitated cubes pack by sharing a single edge, with the centre of masses of both cubes in the nodal plane, as shown in Fig. 6.2(a). This configuration contrasts sharply with the arrangements that are generated through dipole-dipole interactions [137], depletion forces [138], or entropic considerations [139, 63, 140]. In order to confirm that the cluster configuration we observe are driven by anisotropic acoustic forces, we levitate different combinations of shape pairs. Two cones also cluster by aligning a single edge, with the base of both cones in the nodal plane (Fig. 6.2(b)). In addition,

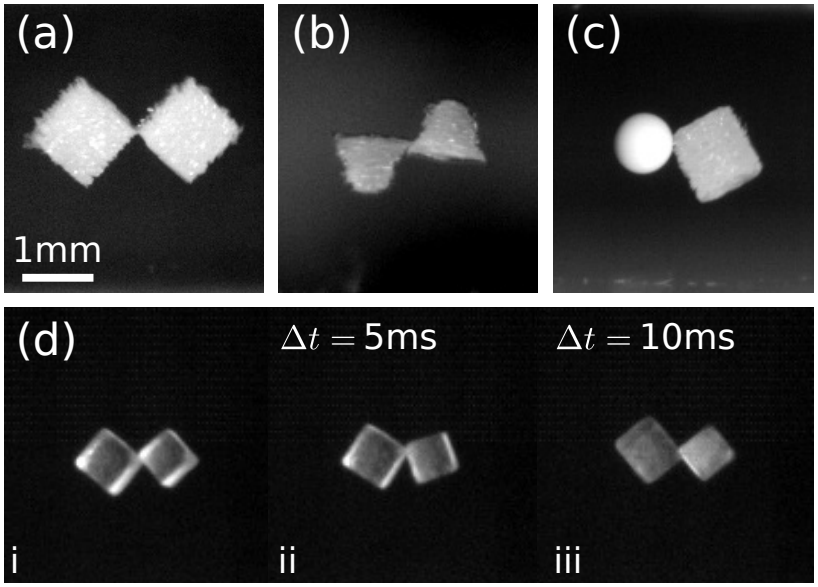

Figure 6.2: **Pairs of levitated particles cluster by sharing an edge.** Pairs of levitated particles imaged from the side. All images are shown to the same scale. (a) Two 3D printed cubes attach via a single edge. (b) Two cones attach by sharing an edge. We also observe configurations where both cones are pointed upwards or downwards. (c) A polyethylene sphere (800μm) attaches to the edge of a cylinder. (d) Sequence of images from the side showing a pair of salt grains executing a hinge motion.

levitating a cylinder with a sphere produces a cluster where the sphere attaches to the sharp edge of the cylinder (Fig. 6.2(c)).

These edge-mediated configurations are stable to fluctuations induced by detuning the trap. Perturbing the cluster produces periodic variations in the contact angle between the cubes, as in Fig. 6.2(d). These hinge-like motions suggest the existence of a restoring force towards the equilibrium configuration shown in Fig. 6.2(a). Increasing the amplitude of active fluctuations by detuning the acoustic field results in the cluster breaking due to energetic collisions with the reflector. We do not observe face-face contacts when the constituent parts of the cluster reassemble. This observation, combined with the existence of periodic hinging motions, suggests that these edge-edge contacts are to be understood as the minimum of some energetic landscape.

6.4 Curvature-controlled acoustic potential: numerical simulations

In order to shed light on the energetic landscape underlying the stability of edge-edge contacts, we calculate the acoustic potential around a perfectly scattering cube using finite-element simulations. This acoustic potential is generated by acoustic scattering from the levitated particles, and can be calculated via a perturbation expansion of the acoustic fields in the levitation medium [38, 40]. Within this approximation, the acoustic potential U_{rad} on a scatterer with radius a (much smaller than λ_0), speed of sound c_p, and material density ρ_p in an inviscid fluid with speed of sound c_0 and density ρ_0 is given as in Eq. 1.5.

We emphasise that Eq. 1.5 is quantitatively accurate only for spherical (point-like) scatterers, in the Rayleigh limit ($a \ll \lambda_0$). However, our particles are closer to the Mie regime ($a \approx 0.1\lambda_0$ in this case), and in addition have finite extent. Our simulation results should thus be interpreted as an approximation of the true acoustic forces on our experimental particles. Nevertheless, they provide a qualitative demonstration of the acoustic forces on a

point object due to the presence of a single object with sharp edges, and provide a useful starting point to explain our experimental observations. Future work could focus on a full simulation of the interaction between a pair of cubes.

We use finite-element simulations (COMSOL) to calculate the acoustic potential on a point scatterer in the vicinity of a single cube. In these simulations, we reproduce the experimental conditions (in the frequency domain) by driving the upper boundary at constant normal acceleration, then establishing perfectly reflecting boundary conditions on a parallel surface half a wavelength below. The simulation domain contains only the levitation volume (we do not simulate outside of the boundaries of the transducer). Plane-wave radiation conditions on the lateral boundaries dissipate the acoustic field. Within this volume, we fix a perfectly scattering cube with side length $l = 0.1\lambda_0$. Given these boundary conditions, we compute the time-averaged quantities $\langle p^2 \rangle$ and $\langle v^2 \rangle$ within the geometry of the trap. The acoustic fields are computed by resolving the acoustic wave equations on a physics-controlled mesh, with element size set to "extremely fine" (maximum element size 2.94×10^{-4}, minimum element size 5.88×10^{-7}, maximum element growth rate 1.1).

Substituting the simulated pressure and velocity fields into Eq. 1.5 thus produces the acoustic potential around a perfectly scattering cube, acting on a point scatterer with radius $a = 0.1\lambda_0$, speed of sound c_p =2 620 m s^{-1}, and density ρ_0 =1 180 kg m^{-3} (material parameters were chosen to match the 3D-printed experimental grains). In order to most clearly show the contribution of the edges, we orient the cube such that its longest diagonal is in the z-direction. A cross-section of the three-dimensional acoustic potential is shown in Fig. 6.3(a). The acoustic field shows a strong gradient in the z direction, due to the primary confining acoustic force – a levitated particle minimises energy by having its centre of mass in the nodal plane ($z = 0$). In addition to the primary confining acoustic field, secondary acoustic scattering results in potential minima located at regions of high curvature (the edges of the cube), indicating that a point particle in the acoustic trap would be disproportionally

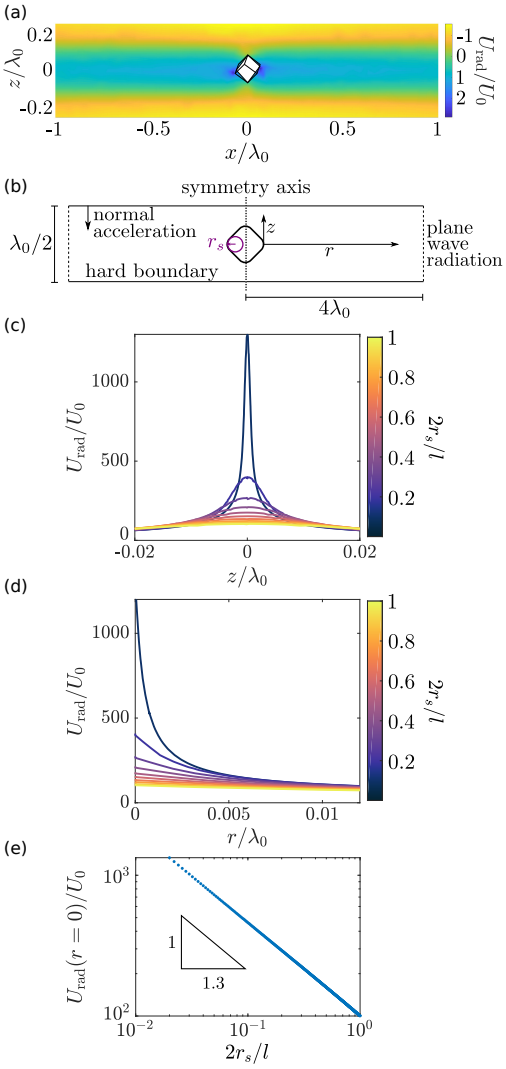

Figure 6.3: **Finite-element simulations of the acoustic potential around a cube reveal that curvature controls acoustic bond strength.** (a) Cross-section of the simulated acoustic potential U_{rad} around a perfectly scattering cube (cross-section in white, drawn schematically using black lines) in an acoustic standing wave. We normalise U_{rad} by U_0, the primary acoustic potential on a point particle in the center of the trap. (b) Schematic of simplified axisymmetric simulation geometry. The acoustic potential is calculated around the surface of revolution of a rounded square with side length l and corner radius of curvature r_s and side length l, fixed in the center of a standing wave. (c) U_{rad}/U_0 as a function of vertical distance from the levitation node z, for different r_s/l. (d) U_{rad}/U_0 as a function of radial distance from the particle surface r, for different r_s/l. (e) Depth of potential minimum, $U_{\mathrm{rad}}(r=0)/U_0$, as a function of r_s/l

attracted to the edges of the cube.

The boundary conditions at the surface of a levitated particle connect geometry and acoustic forces. In particular, we model a perfectly scattering surface using the Neumann boundary condition. For an acoustic wave incident on a perfectly scattering surface with unit normal $\hat{n}$, in an inviscid fluid with pressure p, the boundary condition reads

$$\hat{n} \cdot \nabla p = 0. \tag{6.1}$$

Eq. 6.1 implies that the pressure gradient at a perfectly scattering surface must be orthogonal to the surface normal. In this case, much like a conducting surface in an electric field, the pressure gradient is forced to change with the curvature of the surface. We suggest that this effect focuses the acoustic field in regions of high curvature, thus producing deep potential minima at the edges of the cube.

We illuminate the relation between geometry and acoustic force by quantifying the effect of a single edge on the acoustic potential. Instead of simulating the acoustic potential around a fully three-dimensional cube, we instead use an axisymmetric geometry (boundary conditions shown in Fig. 6.3(b)), and calculate the acoustic field around the surface of revolution of a square with side length $l = 0.1\lambda_0$. We parameterise the edge sharpness of the square using the radius of curvature r_s of the corners. Our results for the acoustic potential in the z- and r-directions as a function of nondimensional edge curvature r_s/l are shown in Figs. 6.3(c) and (d). As r_s/l decreases from 1 (sphere) to 0 (sharp corners), the depth of the acoustic potential increases sharply in both the z- and r-direction.

In order to further quantify the relation between edge sharpness and acoustic force, we simulate the normalised depth of the potential minimum at the surface of the particle, $U_{\mathrm{rad}}(r = 0)/U_0$, as a function of r_s/l. Data is plotted in Fig. 6.3(e), and reveal that the depth of the acoustic potential diverges as a power law as the edge curvature approaches

zero, with exponent $-10/13$. Our results confirm that the near-field force between a point scatterer and a levitated particle in an acoustic field scales sensitively with the sharpness of the edges on the levitated particle.

Based on our simulations of the acoustic field, we suggest an explanation for the robustness of edge-edge contacts and hinge-like motions between a pair of levitated cubes. When two cubes are levitated, their centres of mass are confined to the nodal plane due to the primary acoustic field. In addition, the secondary acoustic force produces short-range attractive forces, which preferentially align the edges of faceted shapes. Upon joining a pair of cubes in the configuration shown in Fig. 6.2(a), we note that rotation of a two-cube cluster around their common edge results in motion of the centres of mass out of the nodal plane. The hinging motion shown in Fig. 6.2(d) thus arises from the interplay of geometry-controlled interactions and the confining acoustic field.

6.5 Clusters of cubes: experimental observations

The geometry of the cubes encourages packing in a square lattice at high packing fractions. At the same time, however, in an acoustic trap, the edges of the cubes give rise to interactions that favour edge-edge contacts (such as illustrated in Fig. 6.2(a)). Since each cube can only make two edge-edge contacts (one on each side of a cube positioned as in Fig. 6.2(a)), as the cluster size grows, it becomes harder and harder for all cubes in the cluster to satisfy their constraints. The acoustic and contact forces that drive self-assembly in an acoustic trap thus also produce highly frustrated clusters. Such clusters exhibit a multiplicity of particle arrangements, transitions between which require extensive reconfigurations.

As an example, Fig. 6.4(a) shows the assembly of two possible configurations of the 3-cube cluster: a linear chain of cubes (ii), and a close-packed configuration where three cubes share a corner (v). Only one of these shapes (close-packed) is available to a cluster of three spheres, since a linear chain of three spheres does not have enough bonds to be rigid, and will

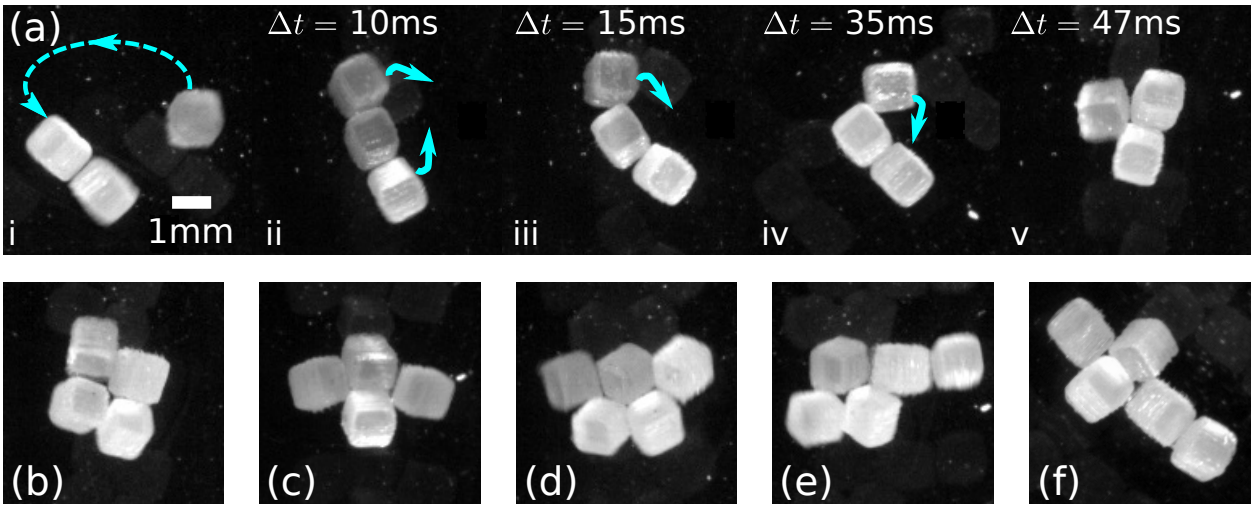

Figure 6.4: [**Cluster formation driven by particle edges.** (a) Sequence of images from below showing the assembly and subsequent folding of a 3-cube cluster. Note that the 3-cluster exhibits two possible configurations: a linear chain (ii) and a triangular cluster (v). (b,c) Two different possible configurations of the 4-cube cluster. (d-f) Three possible configurations of the 5-cube cluster. Note that (b) and (d) correspond most closely to the isostatic cluster shapes of four and five spheres respectively

thus fold into a close-packed arrangement. In contrast, the edge-edge contacts of the cubes have finite extent, so that local contact forces along the length of the contact can stabilise linear chains of cubes. These linear chains also satisfy the condition that all particles in the cluster only interact via their edges.

When active fluctuations in the acoustic field become strong enough (the acoustic trap is far from resonance), the clusters fluctuate up and down in the trap, occasionally colliding with the reflector. These collisions can break bonds between particles in a cluster, disrupting the linear configuration of cubes. The cluster then folds into its other, close-packed configuration (Fig. 6.4(a), ii-v). During this process, one of the cubes detaches partially from the rest of the cluster, leaving one of its corners attached. It then pivots about this corner to a new position on the cluster, ultimately joining the other two cubes at the connecting edge between them. Despite the fact that the close-packed 3-cube cluster forces a contact between an edge and a face, we observe that it is stable to further fluctuations in the acous-

tic field, which change the angle of each "hinge" in the cluster but do not trigger dramatic rearrangements.

These two structural motifs – linear and close-packed – form the basis of all larger cluster shapes. Fig. 6.4(b) and (c) shows two of the possible compact four-cube clusters (the linear chain of four cubes is not shown). The cluster shown in Fig. 6.4(c) was formed from a close-packed group of three cubes, with an additional cube added to the side of the (triangular) cluster. In contrast, the cluster shown in Fig. 6.4(b) was formed from a pair of two-cube clusters that adjoined side on, and thus has a different set of internal angles and symmetries. Although the two clusters look similar, since the internal angles of each cluster are incommensurate with the other, rearranging the constituent particles between the shapes requires extensive reconfiguration through the close-packed three-cube arrangement.

Adding another cube dramatically increases the number of available configurations, only three of which we show here (Fig. 6.4(d), (e), and (f)). Each configuration achieves structural stability by mixing linear chains and close-packed motifs. For instance, the configuration shown in Fig. 6.4(d) resembles the isostatic arrangement of five spheres in two dimensions, and consists of a pair of linear chains arranged side by side. Alternatively, the same cluster can be read as a pair of close-packed 3-cube clusters that share a cube. We suggest that this configuration may be interpreted as the "ground-state" for the 5-cluster, because it involves the fewest number of edge-face contacts. However, the degree of cooperativity required to form this structure suggests that five cubes in an acoustic trap are unlikely to generically form this cluster shape without some degree of rearrangement.

Figures 6.4(e) and (f) show alternative 5-cube clusters, each of which is formed from a close-packed 3-cube cluster, one site of which is attached to a linear chain. We observe that adding a cube onto the 4-cluster in (b) results in the 5-cluster in (e), while adding a cube to the cluster in (c) produces the cluster in (f). Importantly, rearranging (e) into the "ground-state" configuration in (d) requires a single cube pivoting into position. In contrast,

because the 4-cluster in (c) is geometrically incommensurate with the packing that leads to the ground state of the 5-cluster system, rearranging (f) into (d) requires the deconstruction of the cluster into the appropriate 3-cube motifs.

6.6 Discussion and Conclusions

We have presented acoustic levitation as a novel means to tune anisotropic, attractive interactions in a granular material. We show that particles in an acoustic field are strongly attracted to sharp edges, leading to the formation of edge-edge (rather than face-face or face-edge) contacts between cubes, cylinders, and tetrahedra. These contacts support hinge-like motions, which result from a combination of the confining acoustic field and short-range forces from acoustic scattering. Simulations show that the magnitude of these short-range forces is controlled by the radius of curvature of the particle edges. Our results apply to a wide range of assembly environments (any medium that supports an acoustic standing wave) and materials (anything that scatters sound), opening possibilities for the assembly of complex granular structures from directed interactions. Future work could also utilise these directional acoustic forces to design and 3D print particles with shapes that optimise their packing, or their dynamics, in an acoustic trap.

The interplay of contact forces due to particle shape and edge-edge interactions due to acoustic forces produces a diverse range of cluster shapes. The structure and dynamics of these clusters, particularly in the large number limit, raises interesting questions about geometric frustration in self-assembly, ergodicity in activated granular matter, and the effect of attractive forces on jamming.

CHAPTER 7

ACOUSTICALLY LEVITATED LOCK AND KEY GRAINS

7.1 Introduction

The self-assembly of materials with complex structure requires mechanisms for programmable, specific bonds between subunits. Specific interactions with the appropriate binding energy scales have been successfully developed in systems of self-assembling nanoparticles and colloidal particles. Such interactions rely on the addressability of hydrogen-bonded complementary DNA strands [141, 142], or the shape [3, 143] and surface [5, 144] dependence of depletion (entropic) forces. However, there remains a need for equivalent strategies for directed bonds, with tunable specificity, between out-of-equilibrium particles. In particular, the larger mass of granular particles necessitates the development of stronger forces between self-assembling particles than can be provided by chemical or entropic bonds.

Here we show that acoustic levitation offers one possibility for the generation of shape-dependent bonds with tunable specificity between pairs of millimeter-scale particles. We levitate particles in an ultrasonic standing wave, allowing for substrate-free assembly. Secondary scattering generates shape-dependent attractive forces between particles, while driving the acoustic trap above its resonance frequency produces active fluctuations that mimic an effective temperature and allow the clusters to explore their configuration space. We take advantage of 3D printing to fabricate and rapidly prototype precisely designed planar particles. Our results demonstrate that the local curvature of a particle binding site tunes the energy landscape along its perimeter, in turn controlling the selectivity and bound-state lifetime for attaching a matching particle. The bound-state lifetime can further be tuned by adjusting the binding site area, or the height of the particles. We show that these principles can be used to design and assemble particles into complex structures.

7.2 Materials and Methods

We begin with the simplest version of a two-dimensional granular lock: a crescent shape consisting of the union of a disk and a disk-shaped hole, whose centres are separated by distance d. We fix the radius of the disk to be 1mm, with the radius of the disk-shaped hole a, and the height of the crescent h variable. The locks were 3D printed using UV-cured hard plastic (Vero family of materials, density 1170-1180 kg m^{-3}) using a Stratasys J850 Prime printer (accuracy $\pm 100\mu$m). For "keys" we use polyethylene spheres (Cospheric, diameter 710–850μm).

All particles are levitated in an acoustic trap in air as described in Chapter 2, with $\lambda_0 =$ 7.5mm and trap height λ_0 (such that particles are levitated in the lower of two nodal planes, located $\lambda_0/4$ above the reflector surface). In the nodal plane, a lock particle levitates with its flat faces (roughly) parallel to the reflector and transducer. For each experimental run, particles were inserted with a tweezer. The resulting dynamics were then recorded with a high-speed camera (Vision Research Phantom v25) at 3,000 frames per second. Since sharp edges induce preferential contacts between levitated particles [88], a key particle attaches to the lock particle along one of its edges if the lock height h is large, or such that it is in contact with both edges if h is smaller than a particle diameter.

In order to induce cluster rearrangements, we impose an effective temperature by driving the acoustic trap with a frequency larger than its resonance frequency ($\Delta f/f_0 = 1.5 \times 10^{-3}$). In this far from resonance acoustic trap, the key particle fluctuates around the rim of the lock particle, occasionally detaching from the lock and orbiting, before bouncing against the lock and again becoming bound to the lock particle (Fig. 7.1(a)). We assess the likelihood that the lock particle successfully captures ("eats") the key particle in its binding site by measuring the probability of eating $P(\text{eat})$, defined as the ratio of the time spent inside the binding site to the total time spent with lock and key as a cluster (key attached to lock in any position).

7.3 Successful binding probability: mismatched locks and keys

Our results for the eating success rate of locks with binding site radius $a = 1$mm (roughly twice the radius as the key) are displayed in Fig. 7.1(b). As d/a increases, the binding site area decreases, as does $P(\text{eat})$. In order to account for this decreased binding site area, we model the key as equally likely to occupy any spot on the lock perimeter. This yields a geometric estimate for the probability of eating, P_g, the ratio of the binding site perimeter to the total lock perimeter. Comparing the experimental data to P_g (black dotted line in Fig. 7.1(b) reveals a close match between the data and the ansatz of a random, unbiased walk over the lock perimeter. For locks with mismatched binding sites to the key, then, the probability of successful binding is controlled purely by geometry: the relative lengths of the binding site and the lock perimeter.

In order to probe the physical basis of this geometric binding, we simulate the energy landscape of the lock perimeter. This energy landscape arises from secondary acoustic scattering from the particles in the trap, and for particles much smaller than the wavelength of sound, can be calculated using scattering expansions of the pressure and velocity fields in the acoustic cavity, as described in Chapter 3. The pressure and velocity fields resulting from a given set of boundary conditions (including the presence of another particle) can then be computed using finite element simulations (COMSOL Multiphysics here), and substituted into Eq. 1.5 to give the acoustic potential. In this case, we fix a perfectly scattering lock particle in the levitation plane, and set up a standing wave (between perfectly reflecting transducer and reflector) whose frequency and wavelength match the experiment. Acoustic fields are dissipated by a plane-wave radiation condition on the lateral boundaries.

Our results, shown in Fig. 7.1(b), show that the acoustic potential varies significantly around the perimeter of the particle, with the regions of highest acoustic potential focused on the horn-like tips of the crescent. The region of lowest acoustic potential is in the center of the binding site. The fact that the binding statistics are consistent with a random walk

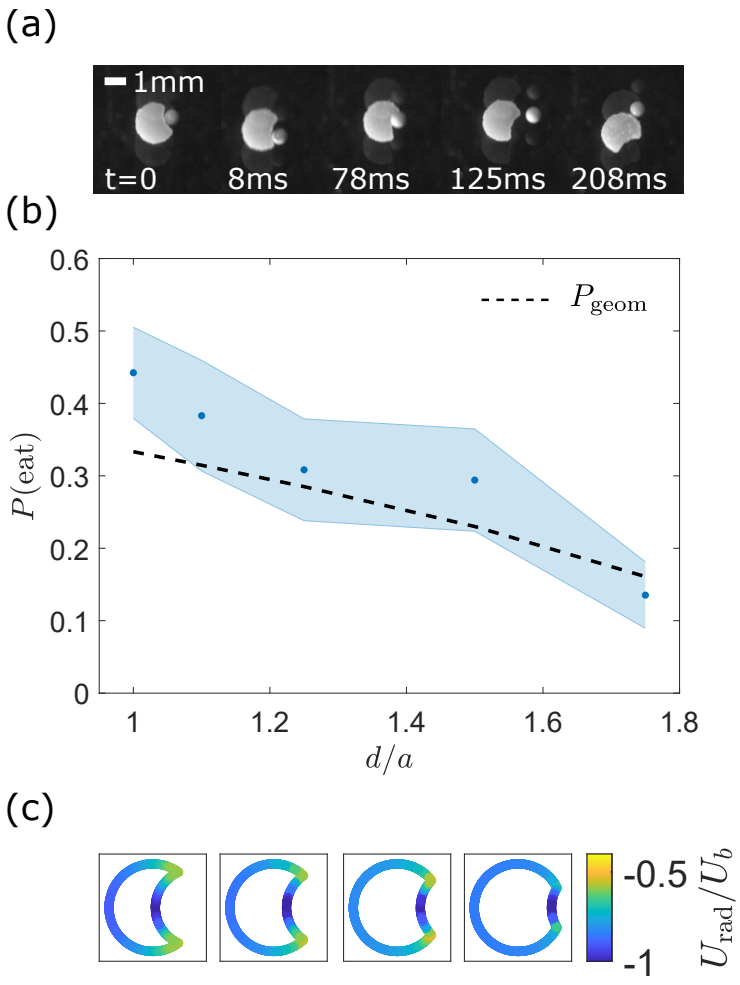

Figure 7.1: For mismatched binding sites and keys, the key particle performs a random walk around the lock particle perimeter. (a) Time-series of images showing the escape of a key particle from a lock binding site with $d/a = 1.5$, $a = 1$mm, $h = 0.5$mm.. (b) Probability of "eating" a key particle for a lock particle with binding site twice the diameter of a key particle, as a function of the overlap distance d divided by the binding site radius $a = 1$mm (data plotted in blue, with standard error). Black dashed line indicates the fraction of the total perimeter of the lock particle occupied by the binding site. For data in this figure, $h = 0.5$mm. (c) Finite-element simulations of the acoustic potential U_{rad}, normalized by the binding site energy U_b on the particle perimeter for (from left to right) $d/a = 1$, 1.25, 1.5, 1.75.

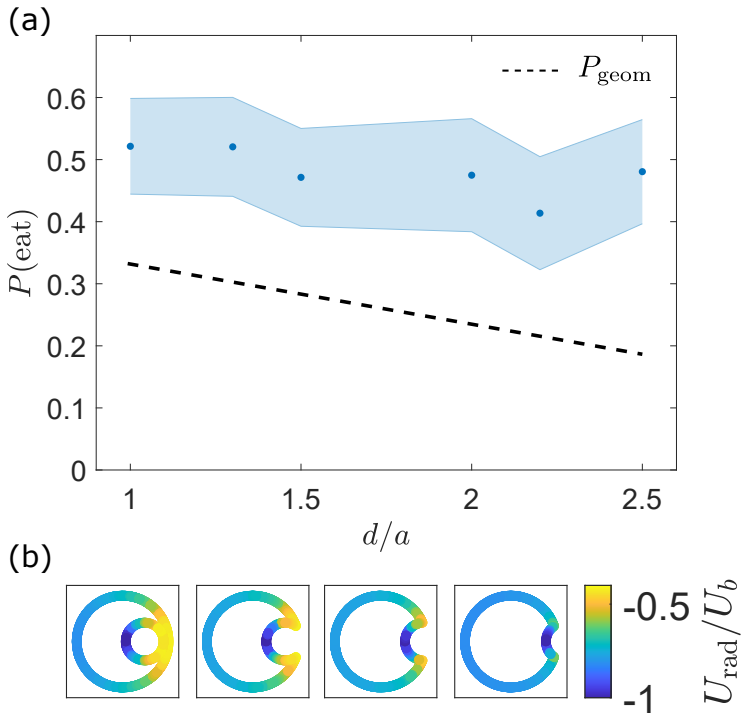

Figure 7.2: When the radius of the key particle and binding site match, the key particle preferentially attaches to the binding site. (a) Probability of "eating" a key particle for a lock particle with binding site the same diameter as a key particle, as a function of the overlap distance d divided by the binding site radius a (data plotted in blue, with standard error). Black dashed line indicates the fraction of the total perimeter of the lock particle occupied by the binding site. (b) Finite-element simulations of the acoustic potential on the particle perimeter for (from left to right) $d/a = 1$, 1.5, 2, 2.5. The colorscale is shared between all four plots, and shows the acoustic potential on the lock edge U_{rad}, normalised by the acoustic potential at the center of the binding site U_b.

of the key around the lock perimeter, despite this spatial variation in energy, suggests that the energy of perturbations to the lock-key cluster is much higher than the characteristic binding energy of the particle to the lock. Such a "high-temperature" process results in binding probabilities that only weakly reflect the energetic biases introduced by variations in the lock shape.

7.4 Successful binding probability: matching locks and keys

In order to go beyond geometry, and introduce preferential binding, we turn to the radius of the lock binding site. Matching the radius of the key particle by shrinking a to 0.5mm results in $P(\text{eat}) \approx 0.5$ (Fig. 7.2(a)). Within error, this value does not depend on d/a. For the smallest binding sites, then, we observe values for $P(\text{eat})$ that are more than double that of the geometric expectation P_{geom}. These results strongly suggest that the shape of these lock particles produces preferential binding at the lock site, compared to the unbiased geometric case.

Finite-element simulations show that the change in curvature at the lock binding site induces a strong local minimum centered in the binding site, as well as much stronger local maxima at the sharp tips of the key binding site (Fig. 7.2(b)). Surprisingly, the energetic discrepancy between the outside of the lock and the inside is comparable to the case with large binding site radius (compare Fig. 7.1(c)), suggesting that energetics may not be the only factor controlling the observed preferential binding.

The results in the mismatched lock case suggest that the action of acoustic active fluctuations on the bound cluster is analogous to the action of a thermal bath on a colloidal cluster, governed by an effective temperature $k_B T_{\text{eff}}$. In order to make this connection quantitative, we measure the potential of mean force on a key particle bound to the outside of the lock (i.e. outside the binding site), parameterised by its angular position with respect to the binding site center θ. For a particle fluctuating in a thermal bath with temperature $k_B T$, observed to have probability $P(\theta)$ of occupying a given angular position θ, this potential is defined as

$$P_{mf}(\theta) \propto -k_B T \ln\left(P(\theta)\right) \ . \tag{7.1}$$

In a true equilibrium system, this potential of mean force is identical to the potential energy on the particle, $U(\theta)$ [145, 146] (up to multiplicative and additive factors). Here,

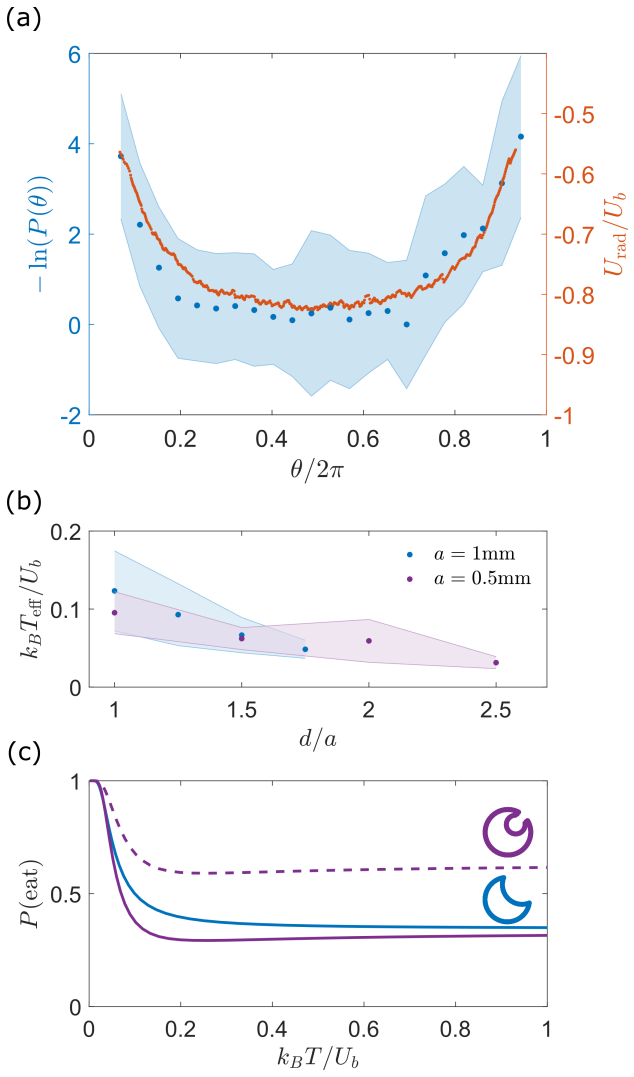

Figure 7.3: Acoustic fluctuations act as an effective temperature. (a) Comparison between the potential of mean force (blue data points and axes, standard error in shaded blue region), and the normalised acoustic potential along the particle edge U_{rad}/U_b (orange line and axes). (b) Normalized effective temperature k_BT_{eff}/U_b, computed by fitting the potential of mean force to U_{rad}, as a function of d/a. Colors correspond to the different radii of curvature a of the two shape families. Shaded areas denote the standard error. (c) Equilibrium prediction for $P(\mathrm{eat})$ as a function of the temperature k_BT, normalized by the bound-state energy U_b. Predictions are plotted for two shapes with $d/a = 1$, whose binding sites have radius of curvature $a = 0.5$mm (purple) and $a = 1$mm (blue). Solid (dotted) lines indicate the use of the physical binding site radius (effective radius, see text for details and definitions).

we treat the acoustic active fluctuations as a noise bath with an effective temperature, which we include as a fitting parameter to the measurement of $P_{mf}(\theta)$. Our results, plotted in Fig. 7.3(a) for a lock particle with $d/a = 2$, $a = 0.5$mm, $h = 0.5$mm, reveal a close correspondence between the measured $P_{mf}(\theta)$ and the simulated acoustic potential, U_{rad}/U_b. The action of the active fluctuations on the outside of the lock thus closely resembles the driving of a thermal reservoir, with the local potential energy determining the local binding probability.

Our measurements of $P_{mf}(\theta)$ can also be used to extract the effective temperature of the active fluctuations on the lock outside, k_BT_{eff} (Fig. 7.3(b)). Surprisingly, our results show that the measured effective temperature of the lock outside is roughly consistent across all measured shapes, despite the fact that $P(\text{eat})$ is very different between the two shapes.

In an equilibrium system, this same k_BT_{eff}, as measured by the energetics of the particle perimeter, also governs $P(\text{eat})$. We consider that the perimeter of the lock particle is associated with an energy landscape as a function of arclength s, $E(s)$. For a key particle fluctuating around the perimeter of this particle (whose inside and outside edges we consider to be arcs of circles with radii R_{in} and R_{out} respectively), in a thermal bath with temperature k_BT, $P(\text{eat})$ is given by the probability of finding the key on the lock interior:

$$P(\text{eat}) = \frac{\int_{in} ds\, e^{-E(s)/k_BT}}{\int_{in} ds\, e^{-E(s)/k_BT} + \int_{out} ds\, e^{-E(s)/k_BT}} \tag{7.2}$$

$$= \frac{\int_{in} d\theta\, R_{in} e^{-E(s)/k_BT}}{\int_{in} d\theta\, R_{in} e^{-E(s)/k_BT} + \int_{out} d\theta\, R_{out} e^{-E(s)/k_BT}}\ , \tag{7.3}$$

where *in* and *out* denote integrating over the binding site, and the lock outside respectively. Substituting $E(s)$,R_{in}, and R_{out} into Eq. 7.3 produces the solid lines in Fig. 7.3(c). Eq. 7.3 thus predicts very similar binding probabilities for different cluster shapes, in contrast to the measured probabilities, which differ by as much as a factor of two.

In order to account for this discrepancy, we turn to the geometry of the lock-key bound pair. Eq. 7.3 assumes that all arc lengths are equal between the inside and outside of the lock. This assumption is valid in the limit that the key particle is infinitesimally small, and effectively interacts locally with a planar angular section of the lock. However, the area of contact between a key and a matched binding site is much larger than the case where the key and lock do not match. As a first approach, we use the harmonic mean of R_{in} and the key radius R_{key} as the effective radius of interaction R_{eff}, defined as

$$R_{\text{eff}} = \frac{R_{\text{in}} R_{\text{key}}}{R_{\text{in}} - R_{\text{key}}} \,. \tag{7.4}$$

Substituting Eq. 7.4 into Eq. 7.3 produces the dashed curve in Fig. 7.3(c), resolving the discrepancy with the experimental measurements of $P(\text{eat})$. Our results thus suggest that the probability of binding is controlled not only by the acoustic active effective temperature, but also by the geometry of the lock binding site, as parameterized by Eq. 7.4. This geometric correction to the binding probabilities is reminiscent of the use of the Derjaguin approximation in calculations of the depletion force in colloidal systems [3], raising the possibility of further analogies between acoustic forces and other types of thermal fluctuation forces.

7.5 Lock height tunes the bound state lifetime

Although the fluctuations of the key around the outside of the lock are dierctly controlled by the two-dimensional energetics of the lock perimeter, the full cluster dynamics take place in a three-dimensional acoustic trap, where particles are weakly confined to lie in the levitation plane. A particularly interesting case is presented by $d/a = 1$, when $a > d$. In this case, where the binding site is completely enclosed in the lock, a random walk around the outside of the lock particle would not be expected to result in a successful binding between the lock and

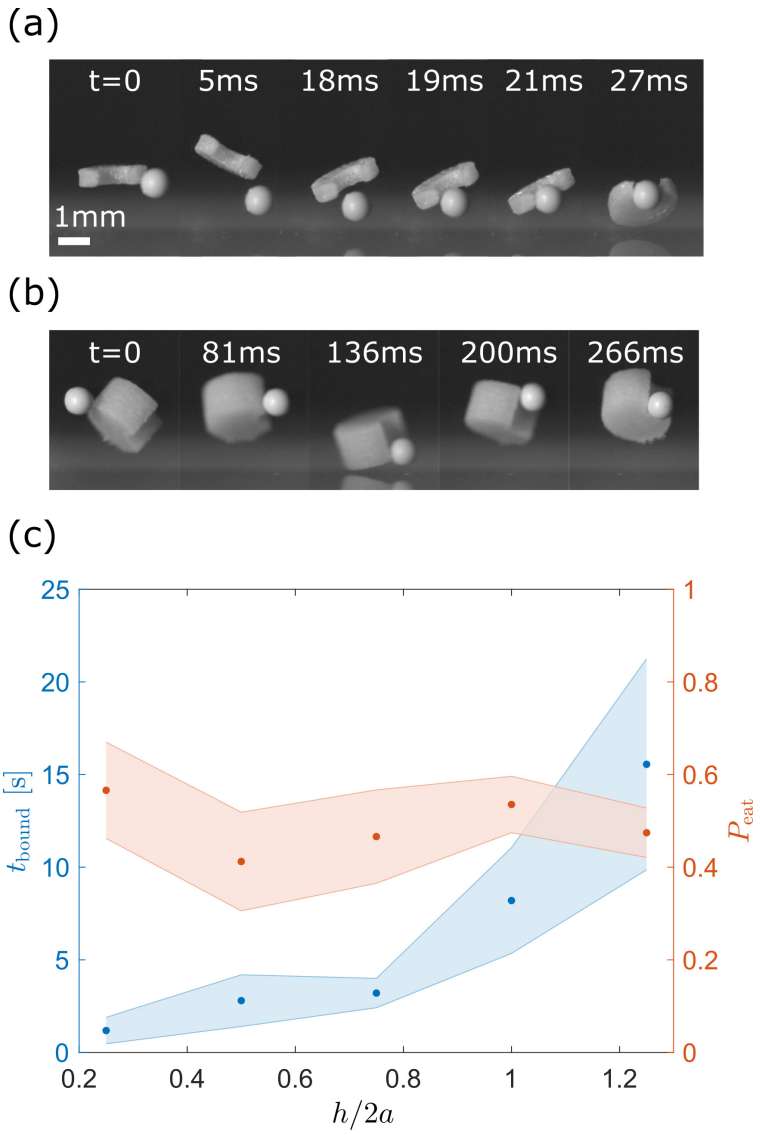

Figure 7.4: Lock particle height tunes the bound-state lifetime, without tuning the bound state probability. (a) Time-series of side-view images, showing a key particle entering the binding site of a lock with $d/a = 1$, a =1mm, $h = 0.5$mm. (b) Time-series of side-view images, showing a key particle entering the binding site of a lock with $d/a = 2$, a =1mm, $h = 1.25$mm. (c) Probability of "eating" a key particle for a lock particle with $d/a = 2$, a =1mm (red data points, right axis) and average bound state lifetime (blue data points, left axis), as a function of the key height h divided by the binding site diameter $2a$. Shaded areas indicate the standard error.

key particle. The fact that these binding events are observed with high probability suggests that the transition between bound and unbound keys must involve some degree of motion in three dimensions: i.e. that the cluster does not remain fully parallel to the levitation plane as it fluctuates. Such a transition between bound and unbound must involve a transition of the key over the lock edge, and onto the face of the lock. An example of such an event is shown in Fig. 7.4(a), where a key enters the binding site by going beneath the tips of the lock particle.

Such a three-dimensional crossing event offers another possibility for tuning the bound-state lifetime of a lock and key cluster: the height of the lock particle. In addition to particle flat faces being repulsive [88], particles that escape out of a tall binding site face the additional energetic cost of the primary acoustic field, which acts to keep the particle in the nodal plane. In addition, inside a binding site larger than the diameter of the key particle, a key can fluctuate between the two vertical edges of the binding site (Fig. 7.4(b)), offering both a means to dissipate kinetic energy injected by the active fluctuations, and also a reduction in the probability of a direct collision between the key particle and the reflector plate.

These effects lead to an increase in the bound state lifetime for a lock-key pair by up to a factor of 4 (Fig. 7.4(c)). Unlike colloidal clusters in thermal equilibrium, where increasing the bound state lifetime by decreasing the temperature leads to a corresponding increase in bound state probability (Fig. 7.3(a)), increasing the bound state lifetime by tuning the lock thickness does not change the probability of the key being eaten by the lock. The three-dimensional nature of the acoustic lock and key cluster thus offers an opportunity to separately tune the bound state probabilities and lifetimes, to yield designed structures with parts whose dynamics can take place over a wide range of timescales.

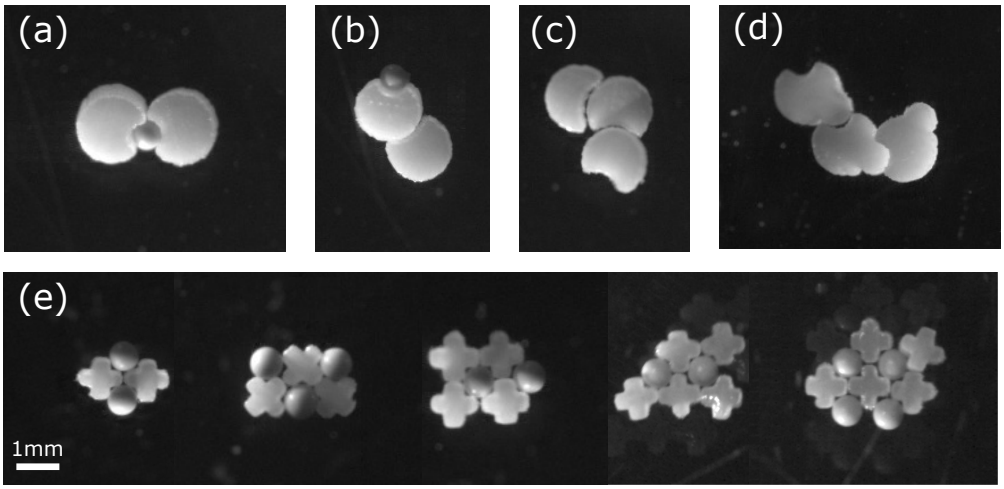

Figure 7.5: Self-assembly of lock and key granular clusters. (a) Cluster composed of two lock particles and a key. (b) Three lock particles with additional keys printed on the outside. (c) A key, with two locks of varying binding site curvature. (d) Three keys with varying binding site overlap distance. (e) Spherical particles with cross-shaped particles form alternating, "host-guest" structures with (i) two spheres and two crosses, (ii) three spheres and three crosses, (iii) two spheres and four crosses, (iv) two spheres and five crosses, and (v) four spheres and five crosses. (b) A spherical particle with a pair of lock particles.

7.6 Self-assembling lock and key structures

Using these design principles, we can take advantage of the flexible acoustic bonds between lock and key to create a variety of lock and key granular clusters (Fig. 7.5). A pair of locks can assemble on either side of a key, forming a flexible jointed structure in the levitation plane (Fig. 7.5(a)). Alternatively, a lock particle can attach to the outside of a lock particle with matching radius of curvature. Combined with a key, the cluster of three particles can form a snowman-like stack of disks (Fig. 7.5(b)). The match between the curvature of the lock outside and a different lock binding site can also result in stacked chains of particles in the absense of keys (Fig. 7.5(c)).

Additional features can also be easily added to the lock. For instance, the position of the key can be directly fixed onto the lock body by printing an additional intersecting disk, again resulting in chains of particles (Fig. 7.5(d)). Varying the position of the attached key can

then be used to tune the persistence length of the granular chain. Alternatively, additional binding sites can be added to the lock surface. These can then be combined with additional keys and locks to form host-guest clusters (Fig 7.5(e)).

7.7 Conclusions

In this Chapter, we have taken the first steps towards acoustically levitated directed assembly. We have shown that shape plays a key role in regulating the assembly probabilities of lock and key structures: when the radius of curvature of a key and lock binding site match, their probability of binding can increase by a factor of two (compared to the unmatched case). This increased probability of binding is a result of both an acoustic active effective temperature, and of the area of contact between the particle and binding site. Additionally, in the nonequilibrium environment of the acoustic trap, the connection between binding probabilities, energetics, and fluctuations becomes decoupled, making it possible to separately tune binding times and binding probabilities via the lock particle height.

The effect of lock shape (as parameterised here by binding site depth, binding site curvature, and lock height) on the lock energy landscape can be easily simulated using finite element simulations, then rapidly prototyped using 3D printing. Additional forces can also be incorporated into these millimetre-size grains, for instance by patterning the grain edges with magnetic patches, or by levitating the grains in an atmosphere saturated with water vapor to encourage the formation of capillary bridges. Such an approach is further anemable to algorithmic optimization to produce a desired energy landscape and binding time, opening the door to the systematic exploration and creation of specific, functional granular acoustic interactions.

CHAPTER 8

CONCLUSIONS

In this thesis, we introduced the use of acoustic levitation to the study of granular matter.

We introduced acoustic levitation as a tool to assemble small clusters of particles and investigate their dynamic reconfigurations. While thermal fluctuations set the magnitude of depletion forces in more microscopic particle systems such as colloids, the sonic depletion forces discussed here depend on the sound pressure amplitude and thus can be controlled independently from the effective temperature of the system. The effective temperature, in turn, was shown to be an emergent quantity that arises from the dynamic response of the levitated objects in the off-resonant regime $\Delta f/f_0 > 0$.

We further used acoustic levitation to contactlessly assemble, drive, and measure the mechanics of active granular rafts, which have attractive forces comparable to applied rotational tensions. Acoustic rotation thus offers the opportunity to tune through a wide range of driven behaviors in an inertial soft solid, from isotropic dilation, to extreme shape change and finally catastrophic failure. The observed size-dependence of the effective surface tension and bulk modulus of the rafts poses a particular challenge to the theoretical modeling of secondary acoustic forces. Our results suggest the need for a systematic theoretical exploration of regimes in particle size and packing density in which acoustic interactions can no longer be treated as pairwise. This size-dependence also plays a role in governing both the elasticity and plasticity of these acoustic solids.

Turning to the effect of shape on acoustic forces, we have presented acoustic levitation as a novel means to tune anisotropic, attractive interactions in a granular material. We show that particles in an acoustic field are strongly attracted to sharp edges, leading to the formation of edge-edge (rather than face-face or face-edge) contacts between cubes, cylinders, and tetrahedra. These contacts support hingelike motions, which result from a combination of the confining acoustic field and short-range forces from acoustic scattering. Simulations

show that the magnitude of these short-range forces is controlled by the radius of curvature of the particle edges.

In addition, we showed that the energy landscape around the perimeter of a particle can be directly tuned by the local curvature of its binding site, in turn controlling the selectivity and bound-state lifetime for attaching a matching particle to the binding site. These principles can be used to design and assemble particles into complex structures.

Together, our results apply to a wide range of assembly environments (any medium that supports an acoustic standing wave) and materials (anything that scatters sound). Our results thus open the door to acoustic levitation as a general platform for the non-invasive asssembly and manipulation of far-from-equilibrium, underdamped systems.

Many avenues remain for exploration. In what remains, we highlight a few of the most exciting. First, this thesis has highlighted the need for further experimental and theoretical work on the acoustic radiation forces between close-packed particles. Experimentally, extracting the acoustic forces between levitated objects requires the development of new experimental and data-processing techniques. In particular, it will become necessary to measure the full three-dimensional position of a levitated particle. This is relatively simple with a dilute sample of particles, but the close-packed nature of the granular rafts precludes the use of many modern 3-D imaging techniques. In addition, methods to reconstruct forces from athermal, underdamped dynamics are only just beginning to be developed [147, 148]. We imagine that the development of an experimental protocol to extract force information from acoustically levitated granular matter will significantly advance scientific frontiers in not only acoustics, but also in 3-D imaging and system identification.

In addition, this work has focused mostly on the size range where the acoustic forces acting on particles can be treated as purely radiative. However, acoustic forces can also be transported through a viscous mechanism: steady-state flows in the acoustic trap, known as acoustic streaming [149]. For a fluid with viscosity η and mass density ρ forced to vibrate

at angular frequency ω, the lengthscale for viscous momentum transfer δ is determined by a balance of the fluid inertia, and its viscosity [99]:

$$\delta = \sqrt{\frac{2\eta}{\rho\omega}}\,. \tag{8.1}$$

In air, at the ultrasound frequencies used in this thesis, $\delta \approx 10\mu$m. As the size of levitated particles decreases, the assumption of purely radiative forces, in an inviscid liquid, become increasingly inaccurate. Indeed, as a particle diameter approaches δ, preliminary experiments and simulations show completely new acoustic forces, dominated by viscous forces rather than acoustic. So far, limited work has been done on the underlying theory of streaming acoustic forces, and much fewer experimental observations of these forces on particles in air.

This thesis has revealed that particle shape and cluster structure are intimately connected in the acoustic trap. We have begun to see how the anisotropic nature of acoustic forces, coupled with the shape of a levitated particle, can lead to cluster shapes with intriguing mechanics: cubes can behave as a hinge, and a raft can support extended stingray-like bending modes. Can we establish a relation between nonequilibrium driving, as provided by acoustic active fluctuations, and the dynamics of an elastic acoustic material? In other words, does an "active acoustic" version of the fluctuation-dissipation theorem exist? Such an avenue of investigation would impinge on several emerging areas of interest in condensed matter physics.

Finally, we have seen that the acoustic trap can generate non-conservative forces on particles, such as the tendency for spontaneous vertical oscillations, or the driven rotation of a cluster. Although this thesis does not attempt to identify the ultimate mechanisms that generate the non-conservative forces, particularly the rotations, this is important upcoming work. In addition, can these non-conservative forces be harnessed to produce forces and torques on an individual particle level? The ability to do so would place levitated granular

matter at a prime position to answer a host of questions relating to active matter in the presence of finite inertia [150], for which there are currently very few experimental models.

Acoustically levitated granular matter provides an endless source of inspiration, both for fascinatingly complex dynamics and for their ability to address deep questions in condensed matter physics. The future is rich with incredible possibilities, limited only by the scope of our curiosity.

REFERENCES

[1] Vinothan N. Manoharan, Mark T. Elsesser, and David J. Pine. Dense packing and symmetry in small clusters of microspheres. *Science*, 301(5632):483–487, 2003.

[2] Wilson Poon. Colloids as big atoms. *Science*, 304(5672):830–831, 2004.

[3] Stefano Sacanna, William TM Irvine, Paul M Chaikin, and David J Pine. Lock and key colloids. *Nature*, 464(7288):575–578, 2010.

[4] Guangnan Meng, Natalie Arkus, Michael P. Brenner, and Vinothan N. Manoharan. The free-energy landscape of clusters of attractive hard spheres. *Science*, 327(5965):560–563, 2010.

[5] Daniela J Kraft, Ran Ni, Frank Smallenburg, Michiel Hermes, Kisun Yoon, David A Weitz, Alfons van Blaaderen, Jan Groenewold, Marjolein Dijkstra, and Willem K Kegel. Surface roughness directed self-assembly of patchy particles into colloidal micelles. *Proceedings of the National Academy of Sciences*, 109(27):10787–10792, 2012.

[6] Peter J Lu and David A Weitz. Colloidal particles: crystals, glasses, and gels. *Annu. Rev. Condens. Matter Phys.*, 4(1):217–233, 2013.

[7] JS Olafsen and JS Urbach. Clustering, order, and collapse in a driven granular monolayer. *Physical Review Letters*, 81(20):4369, 1998.

[8] G D'Anna, P Mayor, A Barrat, V Loreto, and Franco Nori. Observing brownian motion in vibration-fluidized granular matter. *Nature*, 424(6951):909, 2003.

[9] Klebert Feitosa and Narayanan Menon. Fluidized granular medium as an instance of the fluctuation theorem. *Physical Review Letters*, 92(16):164301, 2004.

[10] Aaron S Keys, Adam R Abate, Sharon C Glotzer, and Douglas J Durian. Measurement of growing dynamical length scales and prediction of the jamming transition in a granular material. *Nature Physics*, 3(4):260, 2007.

[11] Yuta Komatsu and Hajime Tanaka. Roles of energy dissipation in a liquid-solid transition of out-of-equilibrium systems. *Physical Review X*, 5(3):031025, 2015.

[12] Marcel Workamp, Gustavo Ramirez, Karen E Daniels, and Joshua Dijksman. Symmetry-reversals in chiral active matter. *Soft Matter*, 2018.

[13] Aleksandar Donev, Ibrahim Cisse, David Sachs, Evan A Variano, Frank H Stillinger, Robert Connelly, Salvatore Torquato, and Paul M Chaikin. Improving the density of jammed disordered packings using ellipsoids. *Science*, 303(5660):990–993, 2004.

[14] Joost de Graaf, René van Roij, and Marjolein Dijkstra. Dense regular packings of irregular nonconvex particles. *Physical Review Letters*, 107(15):155501, 2011.

[15] Leah K Roth and Heinrich M Jaeger. Optimizing packing fraction in granular media composed of overlapping spheres. *Soft Matter*, 12(4):1107–1115, 2016.

[16] Amir Haji-Akbari, Michael Engel, Aaron S Keys, Xiaoyu Zheng, Rolfe G Petschek, Peter Palffy-Muhoray, and Sharon C Glotzer. Disordered, quasicrystalline and crystalline phases of densely packed tetrahedra. *Nature*, 462(7274):773, 2009.

[17] Pablo F Damasceno, Michael Engel, and Sharon C Glotzer. Predictive self-assembly of polyhedra into complex structures. *Science*, 337(6093):453–457, 2012.

[18] Max Neudecker, Stephan Ulrich, Stephan Herminghaus, and Matthias Schröter. Jammed frictional tetrahedra are hyperstatic. *Physical Review Letters*, 111(2):028001, 2013.

[19] RP Behringer, D Bi, B Chakraborty, A Clark, J Dijksman, J Ren, and J Zhang. Statistical properties of granular materials near jamming. *Journal of Statistical Mechanics: Theory and Experiment*, 2014(6):P06004, 2014.

[20] Lee Walsh and Narayanan Menon. Ordering and dynamics of vibrated hard squares. *Journal of Statistical Mechanics: Theory and Experiment*, 2016(8):083302, 2016.

[21] Karol Miszta, Joost De Graaf, Giovanni Bertoni, Dirk Dorfs, Rosaria Brescia, Sergio Marras, Luca Ceseracciu, Roberto Cingolani, René Van Roij, Marjolein Dijkstra, et al. Hierarchical self-assembly of suspended branched colloidal nanocrystals into superlattice structures. *Nature Materials*, 10(11):872, 2011.

[22] Emilien Azéma and Farhang Radjai. Force chains and contact network topology in sheared packings of elongated particles. *Physical Review E*, 85(3):031303, 2012.

[23] Marc Z Miskin and Heinrich M Jaeger. Adapting granular materials through artificial evolution. *Nature Materials*, 12(4):326, 2013.

[24] Somayeh Farhadi and Robert P Behringer. Dynamics of sheared ellipses and circular disks: effects of particle shape. *Physical Review Letters*, 112(14):148301, 2014.

[25] Yuchen Zhao, Kevin Liu, Matthew Zheng, Jonathan Barés, Karola Dierichs, Achim Menges, and Robert P Behringer. Packings of 3d stars: stability and structure. *Granular Matter*, 18(2):24, 2016.

[26] Junyao Tang and Robert P Behringer. Orientation, flow, and clogging in a two-dimensional hopper: Ellipses vs. disks. *Europhysics Letters*, 114(3):34002, 2016.

[27] Kieran A Murphy, Karin A Dahmen, and Heinrich M Jaeger. Transforming mesoscale granular plasticity through particle shape. *Physical Review X*, 9(1):011014, 2019.

[28] Meredith Cox, Dong Wang, Jonathan Barés, and Robert P Behringer. Self-organized magnetic particles to tune the mechanical behavior of a granular system. *Europhysics Letters*, 115(6):64003, 2016.

[29] Daniel L Blair and A Kudrolli. Clustering transitions in vibrofluidized magnetized granular materials. *Physical Review E*, 67(2):021302, 2003.

[30] John R Royer, Daniel J Evans, Loreto Oyarte, Qiti Guo, Eliot Kapit, Matthias E Möbius, Scott R Waitukaitis, and Heinrich M Jaeger. High-speed tracking of rupture and clustering in freely falling granular streams. *Nature*, 459(7250):1110, 2009.

[31] Victor Lee, Scott R Waitukaitis, Marc Z Miskin, and Heinrich M Jaeger. Direct observation of particle interactions and clustering in charged granular streams. *Nature Physics*, 11(9):733, 2015.

[32] Geoffroy Lumay and Nicolas Vandewalle. Controlled flow of smart powders. *Physical Review E*, 78(6):061302, 2008.

[33] Marcello Cavallaro, Lorenzo Botto, Eric P Lewandowski, Marisa Wang, and Kathleen J Stebe. Curvature-driven capillary migration and assembly of rod-like particles. *Proceedings of the National Academy of Sciences*, 108(52):20923–20928, 2011.

[34] August Kundt. Iii. acoustic experiments. *The London, Edinburgh, and Dublin Philosophical Magazine and Journal of Science*, 35(234):41–48, 1868.

[35] Lord Rayleigh. Xxxiv. on the pressure of vibrations. *The London, Edinburgh, and Dublin Philosophical Magazine and Journal of Science*, 3(15):338–346, 1902.

[36] Lord Rayleigh. Xlii. on the momentum and pressure of gaseous vibrations, and on the connexion with the virial theorem. *The London, Edinburgh, and Dublin Philosophical Magazine and Journal of Science*, 10(57):364–374, 1905.

[37] Louis Vessot King. On the acoustic radiation pressure on spheres. *Proceedings of the Royal Society of London. Series A-Mathematical and Physical Sciences*, 147(861):212–240, 1934.

[38] LP Gorkov. Forces acting on a small particle in an acoustic field within an ideal fluid. *Sov. Phys. Doklady*, 6:773–775, 1962.

[39] AA Doinikov. Acoustic radiation pressure on a rigid sphere in a viscous fluid. *Proceedings of the Royal Society of London. Series A: Mathematical and Physical Sciences*, 447(1931):447–466, 1994.

[40] Henrik Bruus. Acoustofluidics 7: The acoustic radiation force on small particles. *Lab on a Chip*, 12(6):1014–1021, 2012.

[41] Mikkel Settnes and Henrik Bruus. Forces acting on a small particle in an acoustical field in a viscous fluid. *Physical Review E*, 85(1):016327, 2012.

[42] Glauber T Silva and Henrik Bruus. Acoustic interaction forces between small particles in an ideal fluid. *Physical Review E*, 90(6):063007, 2014.

[43] Wei Wei, David B Thiessen, and Philip L Marston. Acoustic radiation force on a compressible cylinder in a standing wave. *The Journal of the Acoustical Society of America*, 116(1):201–208, 2004.

[44] Jingtao Wang and Jurg Dual. Theoretical and numerical calculations for the time-averaged acoustic force and torque acting on a rigid cylinder of arbitrary size in a low viscosity fluid. *The Journal of the Acoustical Society of America*, 129(6):3490–3501, 2011.

[45] FG Mitri. Radiation forces and torque on a rigid elliptical cylinder in acoustical plane progressive and (quasi) standing waves with arbitrary incidence. *Physics of Fluids*, 28(7):077104, 2016.

[46] Lawrence A Crum. Acoustic force on a liquid droplet in an acoustic stationary wave. *The Journal of the Acoustical Society of America*, 50(1B):157–163, 1971.

[47] TG Leighton, AJ Walton, and MJW Pickworth. Primary bjerknes forces. *European Journal of Physics*, 11(1):47, 1990.

[48] M. A. B. Andrade, F. Buiochi, and J. C. Adamowski. Finite element analysis and optimization of a single-axis acoustic levitator. *Ultrasonics, Ferroelectrics, and Frequency Control, IEEE Transactions on,*, 57(2):469:479, 2010.

[49] Peter Glynne-Jones, Puja P Mishra, Rosemary J Boltryk, and Martyn Hill. Efficient finite element modeling of radiation forces on elastic particles of arbitrary size and geometry. *The Journal of the Acoustical Society of America*, 133(4):1885–1893, 2013.

[50] Philipp Hahn, Ivo Leibacher, Thierry Baasch, and Jurg Dual. Numerical simulation of acoustofluidic manipulation by radiation forces and acoustic streaming for complex particles. *Lab on a Chip*, 15(22):4302–4313, 2015.

[51] Ivo Leibacher, Philipp Hahn, and Jürg Dual. Acoustophoretic cell and particle trapping on microfluidic sharp edges. *Microfluidics and Nanofluidics*, 19(4):923–933, 2015.

[52] Mudi Wang, Chunyin Qiu, Shenwei Zhang, Runzhou Han, Manzhu Ke, and Zhengyou Liu. Sound-mediated stable configurations for polystyrene particles. *Phys. Rev. E*, 96:052604, Nov 2017.

[53] Victor Lee, Nicole M. James, Scott R. Waitukaitis, and Heinrich M. Jaeger. Collisional charging of individual submillimeter particles: Using ultrasonic levitation to initiate and track charge transfer. *Phys. Rev. Materials*, 2:035602, Mar 2018.

[54] Joseph Rudnick and MARTIN Barmatz. Oscillational instabilities in single-mode acoustic levitators. *The Journal of the Acoustical Society of America*, 87(1):81–92, 1990.

[55] Rebecca W. Perry, Miranda C. Holmes-Cerfon, Michael P. Brenner, and Vinothan N. Manoharan. Two-dimensional clusters of colloidal spheres: Ground states, excited states, and structural rearrangements. *Phys. Rev. Lett.*, 114:228301, Jun 2015.

[56] Sho Asakura and Fumio Oosawa. On interaction between two bodies immersed in a solution of macromolecules. *The Journal of Chemical Physics*, 22(7):1255–1256, 1954.

[57] Arshad Kudrolli, M Wolpert, and Jerry P Gollub. Cluster formation due to collisions in granular material. *Physical Review Letters*, 78(7):1383, 1997.

[58] ISAAC Goldhirsch and G Zanetti. Clustering instability in dissipative gases. *Physical review letters*, 70(11):1619, 1993.

[59] Nikolai Brilliantov, Clara Saluena, Thomas Schwager, and Thorsten Pöschel. Transient structures in a granular gas. *Physical review letters*, 93(13):134301, 2004.

[60] Ellen Klein, William Rogers, Solomon Barkley, and Vinothan Manoharan. Structures and assembly pathways of colloidal clusters. *Bulletin of the American Physical Society*, 2018. Contributed talk, APS March Meeting, 2018.

[61] Etienne Jambon-Puillet, Christophe Josserand, and Suzie Protière. Wrinkles, folds, and plasticity in granular rafts. *Physical Review Materials*, 1(4):042601, 2017.

[62] Qian Chen, Sung Chul Bae, and Steve Granick. Directed self-assembly of a colloidal kagome lattice. *Nature*, 469(7330):381, 2011.

[63] Greg van Anders, N Khalid Ahmed, Ross Smith, Michael Engel, and Sharon C Glotzer. Entropically patchy particles: engineering valence through shape entropy. *ACS Nano*, 8(1):931–940, 2013.

[64] Larry Smarr. Mass formula for Kerr black holes. *Physical Review Letters*, 30(2):71, 1973.

[65] R Genzel, R Schödel, Thomas Ott, A Eckart, T Alexander, F Lacombe, D Rouan, and B Aschenbach. Near-infrared flares from accreting gas around the supermassive black hole at the galactic centre. *Nature*, 425(6961):934–937, 2003.

[66] Jonathan C McKinney and Charles F Gammie. A measurement of the electromagnetic luminosity of a Kerr black hole. *The astrophysical journal*, 611(2):977, 2004.

[67] Kevin J Walsh, Derek C Richardson, and Patrick Michel. Rotational breakup as the origin of small binary asteroids. *Nature*, 454(7201):188–191, 2008.

[68] Ben Rozitis, Eric MacLennan, and Joshua P Emery. Cohesive forces prevent the rotational breakup of rubble-pile asteroid (29075) 1950 DA. *Nature*, 512(7513):174–176, 2014.

[69] OS Barnouin, MG Daly, EE Palmer, RW Gaskell, JR Weirich, CL Johnson, MM Al Asad, JH Roberts, ME Perry, HCM Susorney, et al. Shape of (101955) Bennu indicative of a rubble pile with internal stiffness. *Nature Geoscience*, 12(4):247–252, 2019.

[70] Yoshihiko Arita, Michael Mazilu, and Kishan Dholakia. Laser-induced rotation and cooling of a trapped microgyroscope in vacuum. *Nature Communications*, 4(1):1–7, 2013.

[71] S Cohen, F Plasil, and WJ Swiatecki. Equilibrium configurations of rotating charged or gravitating liquid masses with surface tension. II. *Annals of Physics*, 82(2):557–596, 1974.

[72] K Pomorski and J Dudek. Nuclear liquid-drop model and surface-curvature effects. *Physical Review C*, 67(4):044316, 2003.

[73] N Schunck, J Dudek, and B Herskind. Nuclear hyperdeformation and the Jacobi shape transition. *Physical Review C*, 75(5):054304, 2007.

[74] Mohsen Arabgol and Tycho Sleator. Observation of the nuclear Barnett effect. *Physical Review Letters*, 122(17):177202, 2019.

[75] RJA Hill and L Eaves. Nonaxisymmetric shapes of a magnetically levitated and spinning water droplet. *Physical Review Letters*, 101(23):234501, 2008.

[76] Subrahmanyan Chandrasekhar. The stability of a rotating liquid drop. *Proceedings of the Royal Society of London. Series A. Mathematical and Physical Sciences*, 286(1404):1–26, 1965.

[77] RA Brown and LE Scriven. The shape and stability of rotating liquid drops. *Proceedings of the Royal Society of London. A. Mathematical and Physical Sciences*, 371(1746):331–357, 1980.

[78] CQ Chen, Y Shi, Y St Zhang, J Zhu, and YJ Yan. Size dependence of Young's modulus in ZnO nanowires. *Physical Review Letters*, 96(7):075505, 2006.

[79] Ravi Agrawal, Bei Peng, Eleftherios E Gdoutos, and Horacio D Espinosa. Elasticity size effects in ZnO nanowires- a combined experimental-computational approach. *Nano Letters*, 8(11):3668–3674, 2008.

[80] Ya Yang, Wen Guo, Xueqiang Wang, Zengze Wang, Junjie Qi, and Yue Zhang. Size dependence of dielectric constant in a single pencil-like ZnO nanowire. *Nano Letters*, 12(4):1919–1922, 2012.

[81] Kenji Koga, Tamio Ikeshoji, and Ko-ichi Sugawara. Size-and temperature-dependent structural transitions in gold nanoparticles. *Physical Review Letters*, 92(11):115507, 2004.

[82] Valerie J Anderson and Henk NW Lekkerkerker. Insights into phase transition kinetics from colloid science. *Nature*, 416(6883):811–815, 2002.

[83] Vinothan N Manoharan. Colloidal matter: Packing, geometry, and entropy. *Science*, 349(6251), 2015.

[84] M Rubin-Zuzic, GE Morfill, AV Ivlev, R Pompl, BA Klumov, W Bunk, HM Thomas, H Rothermel, O Havnes, and A Fouquet. Kinetic development of crystallization fronts in complex plasmas. *Nature Physics*, 2(3):181–185, 2006.

[85] CA Knapek, D Samsonov, S Zhdanov, U Konopka, and GE Morfill. Recrystallization of a 2D plasma crystal. *Physical Review Letters*, 98(1):015004, 2007.

[86] KR Sütterlin, A Wysocki, AV Ivlev, C Räth, HM Thomas, M Rubin-Zuzic, WJ Goedheer, VE Fortov, AM Lipaev, VI Molotkov, et al. Dynamics of lane formation in driven binary complex plasmas. *Physical Review Letters*, 102(8):085003, 2009.

[87] Melody X Lim, Anton Souslov, Vincenzo Vitelli, and Heinrich M Jaeger. Cluster formation by acoustic forces and active fluctuations in levitated granular matter. *Nature Physics*, 15(5):460–464, 2019.

[88] Melody X Lim, Kieran A Murphy, and Heinrich M Jaeger. Edges control clustering in levitated granular matter. *Granular Matter*, 21(3):1–8, 2019.

[89] Shahrokh Sepehrirahnama, Kian-Meng Lim, and Fook Siong Chau. Numerical study of interparticle radiation force acting on rigid spheres in a standing wave. *The Journal of the Acoustical Society of America*, 137(5):2614–2622, 2015.

[90] J-C Tsai, Fangfu Ye, Juan Rodriguez, Jerry P Gollub, and TC Lubensky. A chiral granular gas. *Physical Review Letters*, 94(21):214301, 2005.

[91] G Briand and Olivier Dauchot. Crystallization of self-propelled hard discs. *Physical Review Letters*, 117(9):098004, 2016.

[92] Christian Scholz, Soudeh Jahanshahi, Anton Ldov, and Hartmut Löwen. Inertial delay of self-propelled particles. *Nature Communications*, 9(1):1–9, 2018.

[93] ST Thoroddsen, K Takehara, and TG Etoh. The coalescence speed of a pendent and a sessile drop. *Journal of Fluid Mechanics*, 527:85, 2005.

[94] Dirk GAL Aarts, Henk NW Lekkerkerker, Hua Guo, Gerard H Wegdam, and Daniel Bonn. Hydrodynamics of droplet coalescence. *Physical Review Letters*, 95(16):164503, 2005.

[95] Dazhi Yu, Renwei Mei, Li-Shi Luo, and Wei Shyy. Viscous flow computations with the method of lattice Boltzmann equation. *Progress in Aerospace Sciences*, 39(5):329–367, July 2003.

[96] Martin Bauer, Sebastian Eibl, Christian Godenschwager, Nils Kohl, Michael Kuron, Christoph Rettinger, Florian Schornbaum, Christoph Schwarzmeier, Dominik Thönnes, Harald Köstler, et al. waLBerla: A block-structured high-performance framework for multiphysics simulations. *Computers & Mathematics with Applications*, 81:478–501, 2021.

[97] J. Götz, K. Iglberger, C. Feichtinger, S. Donath, and U. Rüde. Coupling multibody dynamics and computational fluid dynamics on 8192 processor cores. *Parallel Computing*, 36(2):142–151, February 2010.

[98] DRJ Owen, CR Leonardi, and YT Feng. An efficient framework for fluid–structure interaction using the lattice boltzmann method and immersed moving boundaries. *International Journal for Numerical Methods in Engineering*, 87(1-5):66–95, 2011.

[99] Mikkel Settnes and Henrik Bruus. Forces acting on a small particle in an acoustical field in a viscous fluid. *Physical Review E*, 85(1):016327, 2012.

[100] Joseph Rudnick and MARTIN Barmatz. Oscillational instabilities in single-mode acoustic levitators. *The Journal of the Acoustical Society of America*, 87(1):81–92, 1990.

[101] EH Trinh and JL Robey. Experimental study of streaming flows associated with ultrasonic levitators. *Physics of Fluids*, 6(11):3567–3579, 1994.

[102] Sebastian Baer, Marco AB Andrade, Cemal Esen, Julio Cezar Adamowski, Gustav Schweiger, and Andreas Ostendorf. Analysis of the particle stability in a new designed ultrasonic levitation device. *Review of Scientific Instruments*, 82(10):105111, 2011.

[103] Robert C Cammarata and Karl Sieradzki. Surface and interface stresses. *Annual Review of Materials Science*, 24(1):215–234, 1994.

[104] Wolfgang Haiss. Surface stress of clean and adsorbate-covered solids. *Reports on Progress in Physics*, 64(5):591, 2001.

[105] EH Trinh, PL Marston, and JL Robey. Acoustic measurement of the surface tension of levitated drops. *Journal of Colloid and Interface Science*, 124(1):95–103, 1988.

[106] Yuren Tian, R Glynn Holt, and Robert E Apfel. A new method for measuring liquid surface tension with acoustic levitation. *Review of scientific instruments*, 66(5):3349–3354, 1995.

[107] Taylor G Wang, AV Anilkumar, CP Lee, and KC Lin. Bifurcation of rotating liquid drops: results from USML-1 experiments in space. *Journal of Fluid Mechanics*, 276:389–403, 1994.

[108] Debra Lewis, J Marsden, and T Ratiu. Stability and bifurcation of a rotating planar liquid drop. *Journal of Mathematical Physics*, 28(10):2508–2515, 1987.

[109] VD Nguyen, FC Schoemaker, EM Blokhuis, and P Schall. Measurement of the curvature-dependent surface tension in nucleating colloidal liquids. *Physical Review Letters*, 121(24):246102, 2018.

[110] Gabriel V Lau, Patricia A Hunt, Erich A Müller, George Jackson, and Ian J Ford. Water droplet excess free energy determined by cluster mitosis using guided molecular dynamics. *The Journal of Chemical Physics*, 143(24):244709, 2015.

[111] Shenwei Zhang, Chunyin Qiu, Mudi Wang, Manzhu Ke, and Zhengyou Liu. Acoustically mediated long-range interaction among multiple spherical particles exposed to a plane standing wave. *New Journal of Physics*, 18(11):113034, 2016.

[112] Peter Schall, Itai Cohen, David A Weitz, and Frans Spaepen. Visualization of dislocation dynamics in colloidal crystals. *Science*, 305(5692):1944–1948, 2004.

[113] Kazu Suenaga, Hideaki Wakabayashi, Masanori Koshino, Yuta Sato, Koki Urita, and Sumio Iijima. Imaging active topological defects in carbon nanotubes. *Nature Nanotechnology*, 2(6):358–360, 2007.

[114] Paul M Chaikin and Tom C Lubensky. *Principles of condensed matter physics*, volume 10.

[115] Julia R Greer and William D Nix. Nanoscale gold pillars strengthened through dislocation starvation. *Physical Review B*, 73(24):245410, 2006.

[116] Dongchan Jang and Julia R Greer. Transition from a strong-yet-brittle to a stronger-and-ductile state by size reduction of metallic glasses. *Nature Materials*, 9(3):215–219, 2010.

[117] ZW Shan, Raja K Mishra, SA Syed Asif, Oden L Warren, and Andrew M Minor. Mechanical annealing and source-limited deformation in submicrometre-diameter Ni crystals. *Nature Materials*, 7(2):115–119, 2008.

[118] BL Holian, AF Voter, NJ Wagner, RJ Ravelo, SP Chen, Wm G Hoover, CG Hoover, JE Hammerberg, and TD Dontje. Effects of pairwise versus many-body forces on high-stress plastic deformation. *Physical Review A*, 43(6):2655, 1991.

[119] MI Baskes. Many-body effects in fcc metals: a lennard-jones embedded-atom potential. *Physical review letters*, 83(13):2592, 1999.

[120] Gerolf Ziegenhain, Alexander Hartmaier, and Herbert M Urbassek. Pair vs many-body potentials: Influence on elastic and plastic behavior in nanoindentation of fcc metals. *Journal of the Mechanics and Physics of Solids*, 57(9):1514–1526, 2009.

[121] Diego Paul Sánchez and Daniel J Scheeres. Dem simulation of rotation-induced reshaping and disruption of rubble-pile asteroids. *Icarus*, 218(2):876–894, 2012.

[122] Daniel Hestroffer, Paul Sánchez, Lydie Staron, A Campo Bagatin, Siegfried Eggl, Wolfgang Losert, Naomi Murdoch, Eric Opsomer, Fahrang Radjai, Derek C Richardson, et al. Small solar system bodies as granular media. *The Astronomy and Astrophysics Review*, 27(1):1–64, 2019.

[123] Jonathan E Kollmer, Jack Featherstone, Robert Bullard, Tristan Emm, Anna Jackson, Riley Reid, Sean Shefferman, Adrienne Dove, Joshua Colwell, and Karen E Daniels. Probing regolith-covered surfaces in low gravity. In *EPJ Web of Conferences*, volume 249, page 02005. EDP Sciences, 2021.

[124] Seth A Jacobson and Daniel J Scheeres. Dynamics of rotationally fissioned asteroids: Source of observed small asteroid systems. *Icarus*, 214(1):161–178, 2011.

[125] Kimihiko Yasuda, Takao Torii, and Toshihiko Shimizu. Self-excited oscillations of a circular disk rotating in air. *JSME international journal. Ser. 3, Vibration, control engineering, engineering for industry*, 35(3):347–352, 1992.

[126] Jerzy L. Nowinski. Nonlinear Transverse Vibrations of a Spinning Disk. *Journal of Applied Mechanics*, 31(1):72–78, 03 1964.

[127] CD Mote Jr et al. Aerodynamically excited vibration and flutter of a thin disk rotating at supercritical speed. *Journal of Sound and Vibration*, 168(1):15–30, 1993.

[128] AA Renshaw, C D'Angelo III, and CD Mote Jr. Aerodynamically excited vibration of a rotating disk. *Journal of Sound and Vibration*, 177(5):577–590, 1994.

[129] Namcheol Kang and Arvind Raman. Vibrations and stability of a flexible disk rotating in a gas-filled enclosure—part 2: Experimental study. *Journal of Sound and Vibration*, 296(4-5):676–689, 2006.

[130] Nobukatsu Okuizumi. Equilibrium of a rotating circular membrane under transverse distributed load. *Journal of System Design and Dynamics*, 1(1):85–96, 2007.

[131] Jemal Guven, JA Hanna, and Martin Michael Müller. Whirling skirts and rotating cones. *New Journal of Physics*, 15(11):113055, 2013.

[132] Mélanie Delapierre, Debadi Chakraborty, John E Sader, and Sergio Pellegrino. Wrinkling of transversely loaded spinning membranes. *International Journal of Solids and Structures*, 139:163–173, 2018.

[133] Peter J Westervelt. The theory of steady forces caused by sound waves. *The Journal of the Acoustical Society of America*, 23(3):312–315, 1951.

[134] Alexander A Doinikov. Acoustic radiation force on a spherical particle in a viscous heat-conducting fluid. i. general formula. *The Journal of the Acoustical Society of America*, 101(2):713–721, 1997.

[135] Anna Garcia-Sabaté, Angélica Castro, Mauricio Hoyos, and Ricard González-Cinca. Experimental study on inter-particle acoustic forces. *The Journal of the Acoustical Society of America*, 135(3):1056–1063, 2014.

[136] Abhishek Ray Mohapatra, Shahrokh Sepehrirahnama, and Kian-Meng Lim. Experimental measurement of interparticle acoustic radiation force in the rayleigh limit. *Physical Review E*, 97(5):053105, 2018.

[137] Hanumantha Rao Vutukuri, Frank Smallenburg, Stéphane Badaire, Arnout Imhof, Marjolein Dijkstra, and Alfons Van Blaaderen. An experimental and simulation study on the self-assembly of colloidal cubes in external electric fields. *Soft Matter*, 10(45):9110–9119, 2014.

[138] Laura Rossi, Stefano Sacanna, William TM Irvine, Paul M Chaikin, David J Pine, and Albert P Philipse. Cubic crystals from cubic colloids. *Soft Matter*, 7(9):4139–4142, 2011.

[139] Kun Zhao, Robijn Bruinsma, and Thomas G Mason. Entropic crystal–crystal transitions of brownian squares. *Proceedings of the National Academy of Sciences*, 108(7):2684–2687, 2011.

[140] Greg van Anders, Daphne Klotsa, N Khalid Ahmed, Michael Engel, and Sharon C Glotzer. Understanding shape entropy through local dense packing. *Proceedings of the National Academy of Sciences*, 111(45):E4812–E4821, 2014.

[141] Yufeng Wang, Yu Wang, Dana R Breed, Vinothan N Manoharan, Lang Feng, Andrew D Hollingsworth, Marcus Weck, and David J Pine. Colloids with valence and specific directional bonding. *Nature*, 491(7422):51–55, 2012.

[142] Yu Wang, Yufeng Wang, Xiaolong Zheng, Étienne Ducrot, Jeremy S Yodh, Marcus Weck, and David J Pine. Crystallization of dna-coated colloids. *Nature communications*, 6(1):1–8, 2015.

[143] Greg van Anders, Daphne Klotsa, N Khalid Ahmed, Michael Engel, and Sharon C Glotzer. Understanding shape entropy through local dense packing. *Proceedings of the National Academy of Sciences*, 111(45):E4812–E4821, 2014.

[144] Joon Suk Oh, Sangmin Lee, Sharon C Glotzer, Gi-Ra Yi, and David J Pine. Colloidal fibers and rings by cooperative assembly. *Nature communications*, 10(1):1–10, 2019.

[145] John G Kirkwood. Statistical mechanics of fluid mixtures. *The Journal of chemical physics*, 3(5):300–313, 1935.

[146] Benoît Roux. The calculation of the potential of mean force using computer simulations. *Computer physics communications*, 91(1-3):275–282, 1995.

[147] David B Brückner, Pierre Ronceray, and Chase P Broedersz. Inferring the dynamics of underdamped stochastic systems. *Physical review letters*, 125(5):058103, 2020.

[148] Jared L Callaham, J-C Loiseau, Georgios Rigas, and Steven L Brunton. Nonlinear stochastic modelling with langevin regression. *Proceedings of the Royal Society A*, 477(2250):20210092, 2021.

[149] James Lighthill. Acoustic streaming. *Journal of sound and vibration*, 61(3):391–418, 1978.

[150] Daphne Klotsa. As above, so below, and also in between: mesoscale active matter in fluids. *Soft matter*, 15(44):8946–8950, 2019.